# Breaking technical barriers of MRI and MRS to explore human brain functions

Arjan D. Hendriks

**Breaking technical barriers of MRI and MRS to explore human brain functions**
PhD thesis, Utrecht University, the Netherlands


ISBN: 978-90-393-7055-1
Cover design: Proefschrift-All In One (AIO), Guus Gijben
Lay-out: Arjan Hendriks
Printed by: Proefschrift-All In One (AIO), Guus Gijben

The research described in this thesis was funded by NWO Nederlandse Organisatie voor Wetenschappelijk Onderzoek. Research grants: 040.11.581, ALW-834.14.004 and 13339.

# Breaking technical barriers of MRI and MRS to explore human brain functions

**Het doorbreken van technologische barrières van MRI en MRS om de functies van het menselijk brein verder te doorgronden**

(met een samenvatting in het Nederlands)

## Proefschrift

ter verkrijging van de graad van doctor aan de Universiteit Utrecht
op gezag van de rector magnificus, prof. dr. H.R.B.M. Kummeling,
ingevolge het besluit van het college voor promoties
in het openbaar te verdedigen
op woensdag 21 november 2018 des middags te 2.30 uur

door

Arjan Daniël Hendriks

geboren op 6 augustus 1990
te Utrecht

| | |
|---|---|
| Promotor: | Prof. dr. P.R. Luijten |
| Copromotoren: | Dr. N. Petridou |
| | Dr. D.W.J. Klomp |

# Contents

# Chapter 1

## General introduction and thesis outline

## General introduction

Our brain makes us who we are. It is essential to our thoughts, decisions, memories, imagination and personality. Especially the cortex of the brain plays a key role in these processes [1]. Although brain research has made considerable progress over the recent years, there are still many questions that remain unsolved to this day. Fundamental questions about our consciousness and how our brain works, as well as clinical questions in case of neurological diseases such as Alzheimer's and Parkinson's disease.

To be able to answer these questions, further insight into the mechanics of the brain and better techniques to study the brain are required. Sometimes, to see and discover new concepts, new glasses have to be invented first. Similar to how the mechanics and purpose of blood was better understood with the microscope of Antoni van Leeuwenhoek.

### Brain functions translated to physics

Over the recent years it became widely recognized that to get to know more about the mechanics of the brain, it is not enough to look only at static brain anatomy. Understanding of dynamic in-vivo brain functions, including the (neuronally triggered) hemodynamics and metabolism of the brain are essential to take the next step. For every input (stimulus) the brain gets, there is a response that consists of neuronal, metabolic and vascular components. These responses and their characteristics give valuable insight into the mechanics of the brain. These responses have different time scales, but generally the time scale is on the order of a few seconds or less. To be able to follow ***individual*** processes in the ***human*** brain ***in vivo*** and ***in real time*** is the ultimate target. To get there, a high temporal resolution (or high frame rate in camera terminology) is key.

Stimuli received by the senses of the human body get interpreted and processed by the cerebral cortex. Within the cortex, detailed brain structures (columns, layers) play different roles with respect to different brain functions. To which brain function a detailed cortical structure contributes, can differ on a small scale of less than 1 mm. For example, whether a neuronal group in the human visual cortex has a preference for either the left or the right eye (ocular dominance), alternates at a scale of 1 mm [2-4]. Therefore, to accurately measure different brain functions at detailed scale, requires a high spatial resolution as well.

### MRI resolution and scan time, not yet good enough?

Magnetic resonance imaging (MRI) measurements are generally a tradeoff between the signal-to-noise ratio (SNR), resolution, scan time and the imaging volume. For example, the higher the spatial resolution of a scan, the longer the acquisition time of a single volume. With MRI, it is therefore possible to acquire high resolution images, but at the cost of a longer scan time. This is not desirable when aiming to monitor fast and detailed physiological processes. Different MRI techniques measure brain functions and/or brain activity via perfusion, diffusion, blood oxygenation, energy consumption or neurotransmitter concentrations. In this thesis

the focus is on MR techniques that measure brain activity via hemodynamics or metabolism, specifically blood-oxygen-level dependent functional MRI (BOLD fMRI) and magnetic resonance spectroscopy (MRS). Despite the clear interest to measure different brain functions at high spatial and temporal resolution (as described in the previous paragraph), current MR measurement techniques are not yet capable of fulfilling these demands. For example for BOLD fMRI, the combination of both a high temporal resolution (< 1 sec) and a high spatial resolution (< 1 mm) is rarely seen. When measuring the main inhibitory neurotransmitter of the brain γ-aminobutyric acid (GABA), with GABA edited MRS, the commonly reported (dynamic) scan times range between 6 – 30 minutes [5]. This is long when looking at the time scale of brain functions. Therefore, the research described in this thesis is intended to lift some of these time constraining technical barriers of different MR techniques, to get closer to measurements at the speed of physiological brain processes, while maintaining sufficient spatial resolution and SNR.

## Aim

The overall aim of this thesis is to maximize the SNR, temporal resolution and spatial resolution of BOLD fMRI and MRS techniques to be able to gain further insight into the hemodynamics and metabolism of the human brain.

## Brief description of MR techniques used in this thesis

To achieve the overall aim, the research in this thesis focused on improving two techniques. A brief description of these two techniques is provided below.

The first technique is blood-oxygen-level dependent functional MRI (BOLD fMRI), a technique that measures local neuronal function via associated changes in hemodynamics. The principle behind this technique is that activated neuronal areas consume more energy. To meet this energy demand, the brain increases local blood flow and blood oxygenation. Increased blood oxygenation results in a lower concentration of deoxyhemoglobin, which in turn increases the BOLD signal due to the field disturbing paramagnetic properties of deoxyhemoglobin. To monitor short and dynamic signal fluctuations in the brain, the BOLD technique requires acquisition of multiple imaging volumes over time. BOLD fMRI is commonly performed with scans that have a high temporal resolution, such as echo planar imaging (EPI). This type of scan usually consists of one or more shots, making it possible to acquire MRI images in a time window of a few seconds.

The second technique is magnetic resonance spectroscopy (MRS), a technique that is used to study different types of molecules and metabolites in the brain. The magnetic resonance frequency of an atomic nucleus in a molecule is highly sensitive to its chemical environment (electron shielding), giving rise to molecule-specific frequency shifts (chemical shift), which can be visualized in a spectrum. The signal is strong enough to measure millimolar concentrations of neurotransmitters such as γ-aminobutyric acid (GABA) in the brain. MRS scans are not

limited to only measure compounds that contain $^{1}H$ nuclei. Also $^{31}P$ nuclei are commonly targeted to be able to measure energy metabolites, such as adenosine triphosphate (ATP), phosphocreatine (PCr) and inorganic phosphate (Pi).

## Highlights of the MRI machine

In short, an MRI scanner is a powerful magnet containing different types of coils. These include (but are not limited to) superconducting coils, gradient coils, transmit coils and receive coils. In essence, the MRI scan process consists of the following steps: a radio frequency (RF) pulse is sent through transmit coils, the resulting echo from the human body is modulated by gradient coils and the echo is captured by receive coils. Subsequently, the received signal is post processed to create an image or spectrum. To improve both BOLD fMRI and MRS techniques (as described in the aim of this thesis), different components of the MRI scanner were adapted. Below, a few specific MRI scanner components that were essential for this thesis, are highlighted.

The higher the main magnetic field strength of an MRI scanner, the higher the achievable SNR [6]. Additionally, with increasing field strengths, the BOLD contrast improves for fMRI [7] and the spectral resolution improves for MRS [8]. There are also challenges that come with higher field strengths, these include field inhomogeneities, restrictions due to safety limits for heating, and the necessity of tailored MR sequences. The main magnetic field strength of an MRI scanner is commonly expressed in units of tesla (T). Clinical MRI scanners typically have a field strength of 1.5T or 3.0T. In this thesis, an MRI scanner with a strong main magnetic field of 7T is used. This is nowadays often specified as ultra-high field and is preferred when aiming to improve SNR, spatial and temporal resolution of BOLD fMRI and MRS techniques.

In addition to the large static main magnetic field (of several T), the MRI scanner can be controlled to transmit and receive electromagnetic pulses (μT), and to create small varying magnetic fields, called gradients (mT). Gradient fields linearly increase in strength with the distance from the middle of the scanner. These pulses and gradient fields can be applied at different time points, durations and strengths. The overall order and configuration of these events is referred to as a sequence or scan type, and determines the appearance of the resulting image (including the contrast, signal strength, tissue specific sensitivity, weighting, diagnostic value etc.). As an example, BOLD fMRI is commonly performed using a sequence called echo planar imaging (EPI). This is a fast sequence that requires quick alternation of magnetic gradient fields. These fields are created in the MRI scanner by gradient systems. To reduce the dynamic scan time (shorten the acquisition time per frame) of EPI scans, gradient systems can be improved to generate stronger and faster switching magnetic fields.

Receive elements (typically coil shaped) are used to receive the MR echo signal from the body. Another avenue to reduce the dynamic scan time, is to use multiple receive elements simultaneously. This is commonly referred to as parallel imaging. Different parallel imaging methods exist, such as SENSE [9], GRAPPA [10] and CAIPIRINHA [11].

## Outline of the thesis

To be able to gain further insight into the in-vivo mechanics of the brain, this thesis focuses on improving two techniques, being: BOLD fMRI and MRS. Overall, five approaches (**Chapters 2-6**) are investigated to make BOLD fMRI and MRS more suitable for fast and high resolution in-vivo measurements of hemodynamic and metabolic physiological process in the human brain at 7T:

In **Chapter 2** a strategy to improve the (dynamic) scan time and resolution of BOLD fMRI is proposed. The spatial and temporal resolution was pushed by combining high density receive arrays with a shot selective 2D CAIPIRINHA implementation for 3D EPI scans. This combination enabled imaging of the visual cortex at sub-second and sub-millimeter resolution.

In **Chapter 3** a hardware based approach to reduce scan time is discussed, which could be beneficial for a broad range of MRI scans, particularly fMRI scans. Simulations were performed to estimate the potential gain in acceleration performance of a setup with 256 receive coils versus a 32 channel receive coil setup. The results showed that high acceleration factors can be achieved with the 256 channel setup.

In **Chapter 4** novel ideas are presented to further reduce scan time of fMRI scans, by the use of ultrasonic switching gradients. Gradients that switch faster than human auditory range (> 20 kHz), can possibly overcome limitations in current MRI scans (such as peripheral nerve stimulation) and further reduce the scan time of EPI sequences.

In **Chapter 5** a neurometabolic approach to measure brain (in)activity is investigated. The acquisition time of GABA edited MRS in the visual cortex was reduced by using a specially built half volume coil setup. This setup has a large screen with a large visual angle, making it possible to increase the activated cortical volume, allowing a large voxel size for spectroscopy, resulting in either a gain in GABA SNR or a reduction of the acquisition time.

In **Chapter 6** a new strategy to measure brain metabolism is studied. Energy metabolism of the human visual cortex was investigated by performing $^{31}$P functional MRS. The acquisition setup was optimized for high SNR measurements, by using a dedicated $^{31}$P coil and a visual stimulus with a large visual angle. The measurements of inorganic phosphate (Pi) reveal new opportunities and considerations to measure specific acidity (pH) effects in the human visual cortex.

## Intermezzo: The brain as physical reference

Before diving into the different chapters of this thesis that try to capture the dynamic processes in the brain at higher detail and faster sampling rates, it is insightful to know which physical scale is referred to. After all, commonly used words like: a *small* voxel size, *high* resolution and *fast* sampling rate are only relative measures. They are often used in comparison to other measurements or techniques that are available to the scientific community at a certain point in time. However, in imaging it is more insightful to put it in perspective to the organ or object that you are investigating. In our case this is the cortex of the human brain. So, to answer questions such as: "How big is big? How small is small? How fast is fast? How many is many?" the following table denotes a selection of values of brain anatomy and physiology (Table 1). These numbers not only serve as reference values, but also show a wide gap between classical neurophysiology, where measurements are based on single neurons, and fMRI scans that capture clusters of more than ten thousands of neurons per voxel of 1 $mm^3$. This emphasizes the need for measurement techniques that are faster (temporal resolution) and more detailed (spatial resolution).

**Table 1: The brain as physical reference.**

| | |
|---|---|
| **Amount** | |
| $86{\cdot}10^9$ neurons | The human brain is estimated to contain approximately 86 billion ($10^9$) neurons, which can vary by several billions among individuals [12,13]. |
| $1{\cdot}10^6$ neurons | Neural circuits involve at least $10^6$ cells in a complex, recursive network [14]. |
| $40{\cdot}10^3$ neurons | Each voxel of 1 $mm^3$ cerebral cortex includes on average on the order of ten thousands of neurons. The neuronal density in the visual cortex is in the range of 41300 neurons per $mm^3$ [15]. |
| 1 neuron | Classic neurophysiology is based on single-cell recordings or, more recently, on small ensembles of cells [14]. |
| **Size** | |
| 2.5 mm | The thickness of the human cerebral cortex is on average 2.5 mm, with local variations ranging from 1 to 4.5 mm within a single brain [16]. |
| >100 µm | The vessels of the macrovasculature of the brain, such as central arteries and pial veins, have diameters larger than 100 µm ranging up to several millimeters for the larger vessels [17]. These supply and drain blood from several sites of active tissue [18]. |
| <20 µm | The capillary bed in the deeper cortical layers of the brain contains vessels with diameters smaller than 20 µm [17] directly serving the active sites [19]. |
| 0.1 - 10 µm | The diameter of a single human neuronal fiber is variable and on the order of a couple of micrometers. The inner diameters of myelinated axons in human white matter as measured by electron microscopy range from 0.16 µm and up to 9 µm [20]. |
| **Time** | |
| 4 sec | The classic positive BOLD response typically peaks 3–5 sec after the start of a stimulus [21]. A post-stimulus undershoot of the BOLD signal is common and may last for 30 sec or more [22]. More complex dynamics apply for prolonged stimuli of more than 4 sec [23]. |
| 0.5 sec | Cortical layer specific differences in the BOLD onset are generally less than 1 second [19,24], with an average difference of 0.5 sec between cortical layer IV and VI [25]. |
| milliseconds | Neural processes can generally take place at a timescale of few milliseconds [26]. Complete neuronal chains can communicate rapidly, as human reaction times (from visual stimulus to motor output) can be as short as 200 msec [27]. |

## References


1. Dumoulin SO, Fracasso A, van der Zwaag W, Siero JCW, Petridou N. Ultra-high field MRI: Advancing systems neuroscience towards mesoscopic human brain function. Neuroimage 2018;168:345-357.
2. Adams DL, Sincich LC, Horton JC. Complete pattern of ocular dominance columns in human primary visual cortex. J Neurosci 2007;27(39):10391-10403.
3. Yacoub E, Harel N, Ugurbil K. High-field fMRI unveils orientation columns in humans. Proc Natl Acad Sci U S A 2008;105(30):10607-10612.
4. Yacoub E, Shmuel A, Logothetis N, Ugurbil K. Robust detection of ocular dominance columns in humans using Hahn Spin Echo BOLD functional MRI at 7 Tesla. Neuroimage 2007;37(4):1161-1177.
5. Puts NA, Edden RA. In vivo magnetic resonance spectroscopy of GABA: a methodological review. Prog Nucl Magn Reson Spectrosc 2012;60:29-41.
6. Pohmann R, Speck O, Scheffler K. Signal-to-noise ratio and MR tissue parameters in human brain imaging at 3, 7, and 9.4 tesla using current receive coil arrays. Magn Reson Med 2016;75(2):801-809.
7. Ogawa S, Menon RS, Tank DW, Kim SG, Merkle H, Ellermann JM, Ugurbil K. Functional brain mapping by blood oxygenation level-dependent contrast magnetic resonance imaging. A comparison of signal characteristics with a biophysical model. Biophys J 1993;64(3):803-812.
8. Gruetter R, Weisdorf SA, Rajanayagan V, Terpstra M, Merkle H, Truwit CL, Garwood M, Nyberg SL, Ugurbil K. Resolution improvements in in vivo 1H NMR spectra with increased magnetic field strength. J Magn Reson 1998;135(1):260-264.
9. Pruessmann KP, Weiger M, Scheidegger MB, Boesiger P. SENSE: sensitivity encoding for fast MRI. Magn Reson Med 1999;42(5):952-962.
10. Griswold MA, Jakob PM, Heidemann RM, Nittka M, Jellus V, Wang J, Kiefer B, Haase A. Generalized autocalibrating partially parallel acquisitions (GRAPPA). Magn Reson Med 2002;47(6):1202-1210.
11. Breuer FA, Blaimer M, Heidemann RM, Mueller MF, Griswold MA, Jakob PM. Controlled aliasing in parallel imaging results in higher acceleration (CAIPIRINHA) for multi-slice imaging. Magn Reson Med 2005;53(3):684-691.
12. Azevedo FA, Carvalho LR, Grinberg LT, Farfel JM, Ferretti RE, Leite RE, Jacob Filho W, Lent R, Herculano-Houzel S. Equal numbers of neuronal and nonneuronal cells make the human brain an isometrically scaled-up primate brain. J Comp Neurol 2009;513(5):532-541.
13. Herculano-Houzel S. The human brain in numbers: a linearly scaled-up primate brain. Front Hum Neurosci 2009;3:31.
14. Insel TR, Landis SC, Collins FS. Research priorities. The NIH BRAIN Initiative. Science 2013;340(6133):687-688.
15. Haug H. Brain sizes, surfaces, and neuronal sizes of the cortex cerebri: a stereological investigation of man and his variability and a comparison with some mammals (primates, whales, marsupials, insectivores, and one elephant). Am J Anat 1987;180(2):126-142.
16. Fischl B, Dale AM. Measuring the thickness of the human cerebral cortex from magnetic resonance images. Proc Natl Acad Sci U S A 2000;97(20):11050-11055.
17. Duvernoy HM, Delon S, Vannson JL. Cortical blood vessels of the human brain. Brain Res Bull 1981;7(5):519-579.
18. Turner R. How much cortex can a vein drain? Downstream dilution of activation-related cerebral blood oxygenation changes. Neuroimage 2002;16(4):1062-1067.
19. Siero JC, Petridou N, Hoogduin H, Luijten PR, Ramsey NF. Cortical depth-dependent temporal dynamics of the BOLD response in the human brain. J Cereb Blood Flow Metab 2011;31(10):1999-2008.
20. Liewald D, Miller R, Logothetis N, Wagner HJ, Schuz A. Distribution of axon diameters in cortical white matter: an electron-microscopic study on three human brains and a macaque. Biol Cybern 2014;108(5):541-557.

21. Hillman EM. Coupling mechanism and significance of the BOLD signal: a status report. Annu Rev Neurosci 2014;37:161-181.
22. Buxton RB, Uludag K, Dubowitz DJ, Liu TT. Modeling the hemodynamic response to brain activation. Neuroimage 2004;23 Suppl 1:S220-233.
23. Martindale J, Berwick J, Martin C, Kong Y, Zheng Y, Mayhew J. Long duration stimuli and nonlinearities in the neural-haemodynamic coupling. J Cereb Blood Flow Metab 2005;25(5):651-661.
24. Siero JC, Ramsey NF, Hoogduin H, Klomp DW, Luijten PR, Petridou N. BOLD specificity and dynamics evaluated in humans at 7 T: comparing gradient-echo and spin-echo hemodynamic responses. PLoS One 2013;8(1):e54560.
25. Silva AC, Koretsky AP. Laminar specificity of functional MRI onset times during somatosensory stimulation in rat. Proc Natl Acad Sci U S A 2002;99(23):15182-15187.
26. Lodish H, Berk A, Zipursky SL, Matsudaira P, Baltimore D, Darnell J. Section 21.2, The Action Potential and Conduction of Electric Impulses. Molecular Cell Biology, 4th edition. New York: W. H. Freeman; 2000.
27. Ando S, Yamada Y, Tanaka T, Oda S, Kokubu M. Reaction time to peripheral visual stimuli during exercise under normoxia and hyperoxia. Eur J Appl Physiol 2009;106(1):61-69.

# Chapter 2

## High density receive arrays in combination with shot selective 2D CAIPIRINHA for 3D EPI scans:

*accelerated sub-millimeter functional and anatomical MRI at 7T*

Arjan D. Hendriks,
Federico D'Agata,
Tim Schakel,
Liesbeth Geerts,
Peter R. Luijten,
Dennis W.J. Klomp,
Natalia Petridou

*Submitted*

## Abstract

**Purpose:** Push the spatial and temporal resolution of 7T MRI. Investigate whether the improvements in spatial and temporal resolution of high density receive arrays can be enhanced using a 2D CAIPIRINHA sequence for multi-shot 3D EPI scans.

**Methods:** High density receive arrays were combined with a shot selective 2D CAIPIRINHA implementation for multi-shot 3D EPI sequences at 7T. In this implementation, in contrast to conventional inclusion of extra $k_z$ gradient blips, specific EPI shots are left out to create a CAIPIRINHA shift and a reduction of scan time. First, the implementation of the CAIPIRINHA sequence was evaluated with a standard receive setup, by shortening the scan time of sub-millimeter whole brain $T_2$* weighted anatomy imaging. Second, high density receive arrays were combined with the CAIPIRINHA sequence to push the temporal resolution of sub-millimeter 3D EPI (fMRI) scans of the visual cortex.

**Results:** The shot selective 2D CAIPIRINHA sequence enabled a reduction of scan time for 0.5 mm isotropic 3D EPI $T_2$* weighted anatomy scans by a factor 4 as compared to earlier reports. With the combination of this 2D CAIPIRINHA implementation and the high density receive arrays, it was possible to enhance image quality of sub-millimeter 3D EPI scans of the visual cortex at high accelerations, as compared to conventional SENSE. This combination also enabled the acquisition of sub-millimeter and sub-second 3D EPI scans of the visual cortex.

**Conclusion:** High density receive arrays in combination with shot selective 2D CAIPIRINHA for 3D EPI scans prove to be valuable for reducing scan time of sub-millimeter MRI acquisitions.

**Keywords:** 3D EPI, receive arrays, CAIPI, high resolution, visual cortex, 7T

## Introduction

The combination of both a high temporal resolution and a high spatial resolution is essential to examine dynamic and spatially detailed brain functions using functional MRI (fMRI). Within the cortex, detailed brain structures (columns, layers) play different roles with respect to different brain functions. To which brain function a detailed cortical structure contributes, can vary on a small scale of less than 1 mm. Recent developments in fMRI acquisition methods and hardware technologies, particularly at high field (≥ 7T), have enabled visualization of functional detail at a laminar or columnar level [1]. However, in most studies, the high spatial resolution required comes at the cost of low temporal resolution or reduced coverage [2,3]. In general, fMRI measures neuronal function via associated changes in hemodynamics, most commonly using the blood oxygenation level dependent (BOLD) contrast. To reveal biologically relevant characteristics of the hemodynamic response at detailed spatial scale requires not only a high spatial resolution, but also a high temporal resolution [4-6]. Nowadays, despite the strong drive to image the cortex dynamically with high detail, fMRI with both a high temporal resolution (<1 sec) and a high spatial resolution (<1 mm) combined, is rarely seen.

In pursuit of high resolution fMRI with a short dynamic scan time, CAIPIRINHA implementations [7-9] in combination with simultaneous multi-slice methods (SMS), including multiband, have been studied extensively in the recent literature [2,10,11]. Most of these studies are aimed at 2D or multi-slice imaging. More recently, the fMRI field advances towards 3D imaging, because of the gains in SNR at small voxel sizes [12,13]. Multi-shot 3D Echo Planar Imaging (EPI) sequences are effective high resolution fMRI scans. Previous studies have been performed in which the benefits of 3D EPI sequences were combined with the benefits of 2D CAIPIRINHA [14,15]. By implementing additional gradient blips on the slice axes of the EPI sequence, the k-space trajectory can be influenced, and the aliasing patterns caused by under sampling can be controlled. This leads to higher achievable acceleration factors and reduced noise amplification as compared to the traditional acceleration methods such as SENSE [16] and GRAPPA [17].

Similarly, high density receive coil arrays facilitate the use of high acceleration factors with reduced g-factors at high resolutions [18-20]. For imaging the cortex, the benefits of using high density receive coil arrays are two-fold: Locally, at the periphery of the brain it results in an improved SNR. Second, it enhances the encoding performance, because the variation in spatial sensitivity is increased, which can be exploited by parallel imaging techniques to reduce scan time. Ultra-high field strengths have an intrinsic SNR gain and additional spatial variance of local $B_1^-$ fields. A combination of high density receive coil arrays and a 2D CAIPIRINHA sampling pattern at a high field strength of 7T offers the advantage of potentially increasing the resolution even further.

To enhance acceleration performance, both high density receive arrays and 2D CAIPIRINHA intend to increase the variation in spatial sensitivity of the receiver elements at locations that show signal aliasing. Since both methods target the variation in spatial sensitivity, it can be questioned whether these techniques will compete or complement each other. For instance, the high variation in spatial sensitivity of small coil elements in high density receive arrays is already sufficient to achieve high acceleration factors with the traditional parallel imaging methods such as SENSE [20]. Can 2D CAIPIRINHA still significantly contribute to the already achievable high acceleration performance of high density receiver arrays?

This study aims to push the spatial and temporal resolution of 7T MRI by investigating whether the improvements in spatial and temporal resolution of high density receive arrays at 7T can be enhanced by using a 2D CAIPIRINHA sequence for multi-shot 3D EPI scans. A straightforward implementation of shot selective 2D CAIPIRINHA for multi-shot 3D EPI sequences was developed, which, instead of adding extra gradients, leaves them out. Prospectively undersampled datasets were acquired. First, the implementation of the sequence was evaluated by sub-millimeter $T_2$* weighted 3D EPI anatomical imaging. Afterwards, the combination of high density receive arrays and 2D CAIPIRINHA was evaluated on its capability to accelerate sub-millimeter fMRI acquisitions.

## Sequence design

To be able to scan with high density receiver arrays in combination with 2D CAIPIRINHA, a shot selective 2D CAIPIRINHA sampling pattern was implemented for 3D EPI scans on a Philips 7T platform. Several EPI shots of a multi-shot interleaved 3D EPI sequence were selectively skipped resulting in a CAIPIRINHA sampling pattern and a reduction of scan time (Figure 1). The EPI shots were selected in such a way that the acquired $k_z$ planes had varying $k_y$ start positions (a $\Delta k_y$ offset), in correspondence with the targeted CAIPIRINHA sampling pattern. The implementation is based on a multi-shot interleaved 3D EPI sequence, therefore no gradient blips on the $k_z$ axis during the EPI train were required, in contrast to other reports for single shot and $k_z$-segmented 3D EPI sequences, which also use gradient blips on the $k_z$ axis during the EPI train [14]. Both the RF pulses and the $k_z$-gradients of the multi-shot 3D EPI sequence are left untouched, so there is no additional burden on SAR or $k_z$-gradients, as can be the case when using multiband RF pulses or blipped CAIPIRINHA acquisitions. The reconstruction was performed with an adapted SENSE reconstruction [16,21], in contrast to the more commonly reported reconstructions for CAIPIRNIHA datasets in literature, such as GRAPPA [22] and SENSE-GRAPPA hybrid [23,24] reconstructions.

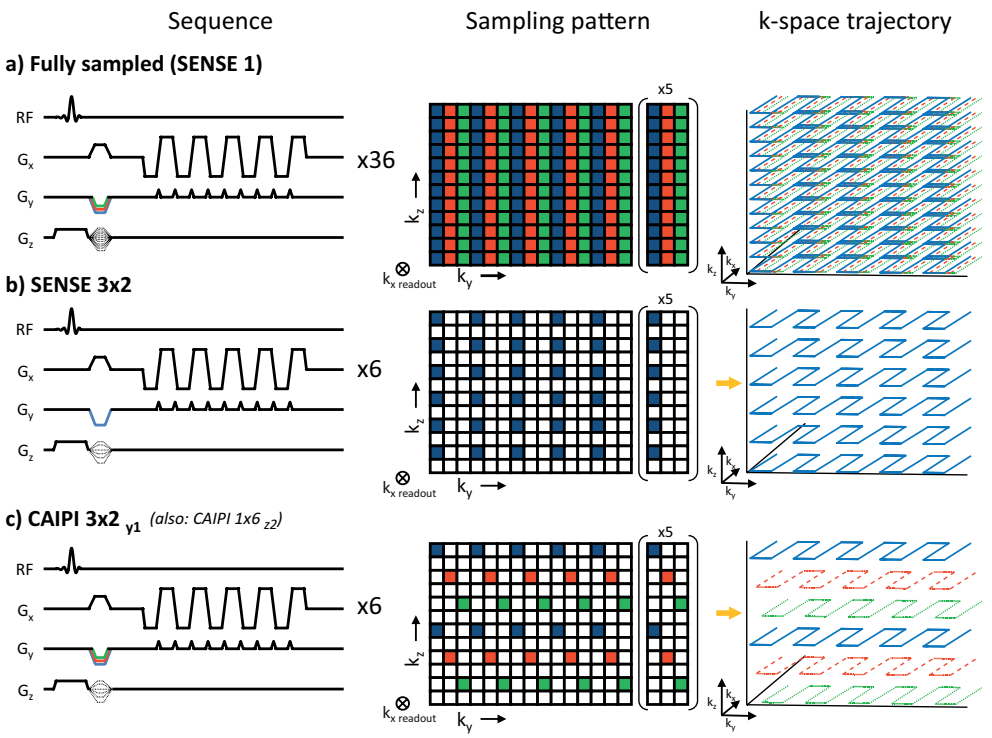


**Figure 1: Sampling schemes of multi-shot 3D EPI sequences. The k-space sampling patterns are displayed for (a) full acquisition, (b) SENSE 3x2 and (c) CAIPIRINHA 3x2 shift y1. Note that the fully sampled k-space contains 3 shots (indicated in blue, red and green) per $k_z$-plane. When using SENSE 3x2, only 1 (blue) shot is acquired for every other $k_z$-plane. 2D CAIPIRINHA uses 1 shot per other $k_z$-plane as well, but alternates between the blue, red and green shots to reduce the g-factor penalty.**

## Methods

The combination of high density receive arrays and 2D CAIPIRINHA for multi-shot 3D EPI scans was investigated in two steps. First, the implementation of the shot selective 2D CAIPIRINHA sequence was evaluated using a standard receive setup (details below) by performing $T_2$* weighted 3D EPI anatomical imaging. Second, the combination of high density receive arrays and the 2D CAIPIRINHA was evaluated on its capability to accelerate sub-millimeter 3D EPI fMRI acquisitions. Two healthy participants were scanned with a 7T Achieva system (Philips, Best, the Netherlands). The participants gave informed consent, and the work was approved by the Medical Ethics Committee of the University Medical Center Utrecht. Both receive setups (Figure 2) are connected to the same transmit setup, consisting of a dual channel transmit/receive birdcage coil (Nova Medical, USA).

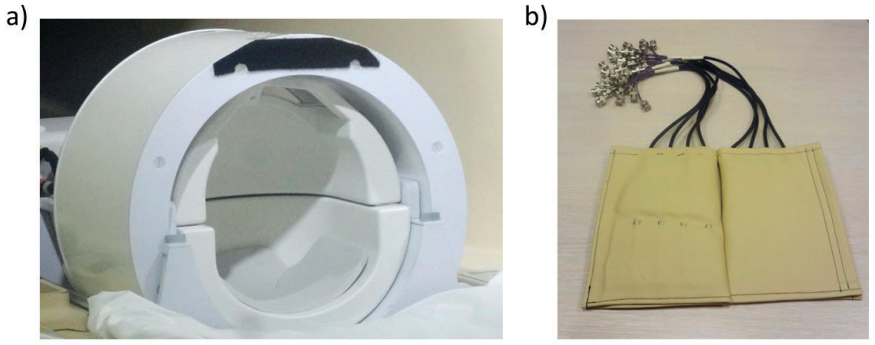


**Figure 2: The two setups used for data acquisition. The 32 channel headcoil (a) is used for the acquisition of whole brain of $T_2$* weighted anatomy scans. The 2x16 channel high density surface coil arrays (b) are used for small FOV imaging of the visual cortex with a short scan time.**

## Shimming and reference scan

$B_0$ shimming of the brain was performed before acquiring the EPI scans. A $B_0$-map was acquired, driving only the dual channel transmit/receive birdcage coil, and the following scan parameters (TE/TR= 1.54/4.0 ms, flip angle 10°, 3.75x3.75x3.75 $mm^3$ voxels, 240x180x180 $mm^3$ FOV, 48 slices, total acquisition time: 18 sec). Second-order shimming parameters were calculated and applied to subsequent scans. After shimming the same $B_0$-map was re-acquired, this time including the calculated shimming values. As last preparation step, a (SENSE) coil sensitivity reference scan was made by successive signal reception with the volume T/R birdcage coil and the individual receive elements. The raw datasets of these scans were saved and used to calculate the coil sensitivity maps required for reconstruction. The coil sensitivity reference scan was a 3D gradient echo with the following scan parameters: TE/TR= 1.01/8.0 ms, flip angle 1°, 3x3x3 $mm^3$ voxels, 240x240x240 $mm^3$ FOV, 80 slices and total acquisition time: 1:55 min.

## Evaluation of sequence implementation, $T_2$* weighted 3D EPI anatomical imaging

Whole brain $T_2$* weighted multi-shot 3D EPI anatomical scans were acquired with a standard 32 channel headcoil [25] (Nova Medical, USA). The headcoil consists of 32 receive elements shaped in a dome like structure around the head. The coil elements are large square loops of approximately 5 x 4 $cm^2$. First, 1 mm isotropic resolution scans were acquired to evaluate the implementation of the shot selective 2D CAIPIRINHA sequence. Retrospectively undersampled datasets were constructed and compared with measured prospectively undersampled datasets. Second, 0.5 mm isotropic resolution scans were acquired, to compare the implementation in relation to the SENSE method. The scan parameters of the $T_2$* weighted 3D EPI anatomical scans can be found in Table 2. In the figures containing results, the CAIPIRINHA sampling

patterns are denoted in the abbreviated format: CAIPI $5_{y2}$, representing an acceleration factor of 5 and a shift of 2 points along $k_y$ direction. The corresponding full specification can be found in the tables, in the format CAIPI 5x1 y2.

**Table 2: Acquisition parameters of the $T_2$* weighted 3D EPI anatomical scans**

| Sampling pattern | Resolution (isotropic) | FOV ($mm^3$) | slices | slice ovs | TR / TE (ms) | flip angle | matrix size | EPI factor | Total scan time |
|---|---|---|---|---|---|---|---|---|---|
| SENSE 1x1 | 1 mm | 240x196x150 | 150 | 1 | 72 / 27 | 16° | 240x195 | 13 | 2:43 min |
| CAIPI 5x1 y2 | 1 mm | 240x196x150 | 150 | 1 | 72 / 27 | 16° | 240x195 | 13 | 0:33 min |
| SENSE 1x1 | 0.5 mm | 240x186x150 | 300 | 1 | 72 / 27 | 19° | 480x364 | 13 | 10:05 min |
| SENSE 4x1 | 0.5 mm | 240x186x150 | 300 | 1 | 72 / 27 | 19° | 480x364 | 13 | 2:31 min |
| SENSE 7x1 | 0.5 mm | 240x186x150 | 300 | 1 | 72 / 27 | 19° | 480x364 | 13 | 1:27 min |
| CAIPI 7x1 y3 | 0.5 mm | 240x186x150 | 300 | 1 | 72 / 27 | 19° | 480x364 | 13 | 1:27 min |

*FOV: field-of-view (AP: anterior–posterior, RL: left–right, FH: feet–head), TR: repetition time, TE: echo time, slice ovs: slice oversampling factor*

## Combination with high density receive arrays, 3D EPI functional imaging

3D EPI scans of the visual cortex were acquired with 2x16 channel high density surface coil receive arrays [20] (MR Coils BV, Zaltbommel, the Netherlands). The high density surface coil array consist of 32 receive channels distributed over two patches of 16 receive elements, which mainly cover the back of the head. The receive elements are rectangular shaped with a size of about 1.5 x 2 cm. Sub-millimeter 3D EPI scans using both SENSE and 2D CAIPIRINHA were acquired, to evaluate the combination of high density receive arrays and a 2D CAIPIRINHA sequence. In this study, these scans are referred to as functional or fMRI scans, because they are optimized for functional imaging of the visual cortex, however, during the measurements of this study no (visual) stimulus is given. Multiple 3D EPI scans were made using different scan parameters to further explore the possibilities and the balance between a high spatial and a high temporal resolution. Several scans were tested with variable spatial resolution, temporal resolution, and acceleration factors, as shown in Table 3. For comparison, a number of scans were also acquired using SENSE.

### Reconstruction

The scans were reconstructed offline in a modified Philips Recon 2.0 environment (Philips Healthcare, Best, the Netherlands). Due to undersampling, the total number of acquired k-space points in the raw dataset was smaller than the fully sampled acquisition expected by the reconstructor. Instead of reducing the dimensions of the expected matrix size, zeros were placed on the k-space positions that were not acquired. This way information on matrix size and the position of the acquired k-space points was preserved. In the reconstruction pipeline, the aliasing indexes were changed to incorporate CAIPIRINHA patterns.

Retrospective undersampling of SENSE 1 data and the corresponding reconstruction was done in Matlab (MATLAB 8.3, MathWorks Inc., MA, USA). The fully sampled data and the coil sensitivity maps were exported from Recon 2.0 into Matlab, where the data was undersampled in k-space and consecutively reconstructed. Similarly, g-factor maps were calculated using the exported coil sensitivity maps, according to equations of Pruessman et al. [16].

**Table 3: Acquisition parameters of the high resolution 3D EPI scans of the visual cortex**

| Sampling pattern | Resolution (isotropic) | FOV ($mm^3$) | slices | slice ovs | TR / TE (ms) | flip angle | matrix size | EPI factor | Dynamic scan time |
|---|---|---|---|---|---|---|---|---|---|
| SENSE 1x1 | 0.99 mm | 64x164x11.9 | 12 | 1.25 | 54 / 27 | 20° | 64x165 | 33 | 4.3 sec |
| SENSE 5x1 | 0.99 mm | 64x164x11.9 | 12 | 1.25 | 54 / 27 | 20° | 64x165 | 33 | 0.86 sec |
| CAIPI 5x1 y2 | 0.99 mm | 64x164x11.9 | 12 | 1.25 | 54 / 27 | 20° | 64x165 | 33 | 0.86 sec |
| CAIPI 7x1 y3 | 0.95 mm | 65x180x13 | 14 | 1 | 54 / 27 | 20° | 68x189 | 27 | 0.79 sec |
| CAIPI 8x1 y3 | 0.95 mm | 65x176x15 | 16 | 1 | 54 / 27 | 20° | 68x184 | 23 | 0.89 sec |
| SENSE 1x1 | 0.80 mm | 50x175x26 | 32 | 1.25 | 54 / 27 | 20° | 64x216 | 27 | 17.5 sec |
| SENSE 8x1 | 0.80 mm | 50x175x26 | 32 | 1 | 54 / 27 | 20° | 64x216 | 27 | 1.75 sec |
| CAIPI 8x1 y3 | 0.80 mm | 50x175x26 | 32 | 1 | 54 / 27 | 20° | 64x216 | 27 | 1.75 sec |
| CAIPI 5x1 y2 | 0.70 mm | 50x164x21 | 30 | 1 | 54 / 27 | 20° | 72x230 | 23 | 3.28 sec |
| CAIPI 10x1 y2 | 0.70 mm | 50x164x21 | 30 | 1 | 54 / 27 | 20° | 72x230 | 23 | 1.64 sec |

*FOV: field-of-view (AP: anterior–posterior, RL: left–right, FH: feet–head), TR: repetition time, TE: echo time, slice ovs: slice oversampling factor*

## Results

The results are analysed in two steps. First, the implementation of the 2D CAIPIRINHA sequence for 3D EPI scans was evaluated using $T_2$* weighted anatomical imaging. Second, the combination of high density receive arrays and the 2D CAIPIRINHA sequence was evaluated based on its acceleration performance for sub-millimeter fMRI acquisitions.

### Evaluation of sequence implementation, $T_2$* weighted 3D EPI anatomical imaging

To evaluate whether the shot selective 2D CAIPIRINHA sequence was implemented correctly, 1 mm 3D-EPI whole brain $T_2$* anatomy weighted images were compared using prospective and retrospective undersampling, as shown in Figure 3. A full non-undersampled SENSE 1 dataset was acquired in 2:43 min and retrospectively undersampled with a 2D CAIPIRINHA pattern and an undersampling factor of 5, as is shown in Figure 3a-c. Both the resulting aliasing as sum of the separate channels is displayed (Figure 3b) and the result after reconstruction (Figure 3c). Correspondingly, a prospectively undersampled CAIPI 5 dataset was acquired in 33 sec and displayed in Figure 3d,e. When comparing the simulated (b,c) and measured (d,e) datasets it should be noted that the images look practically identical, for both the aliased and reconstructed images.

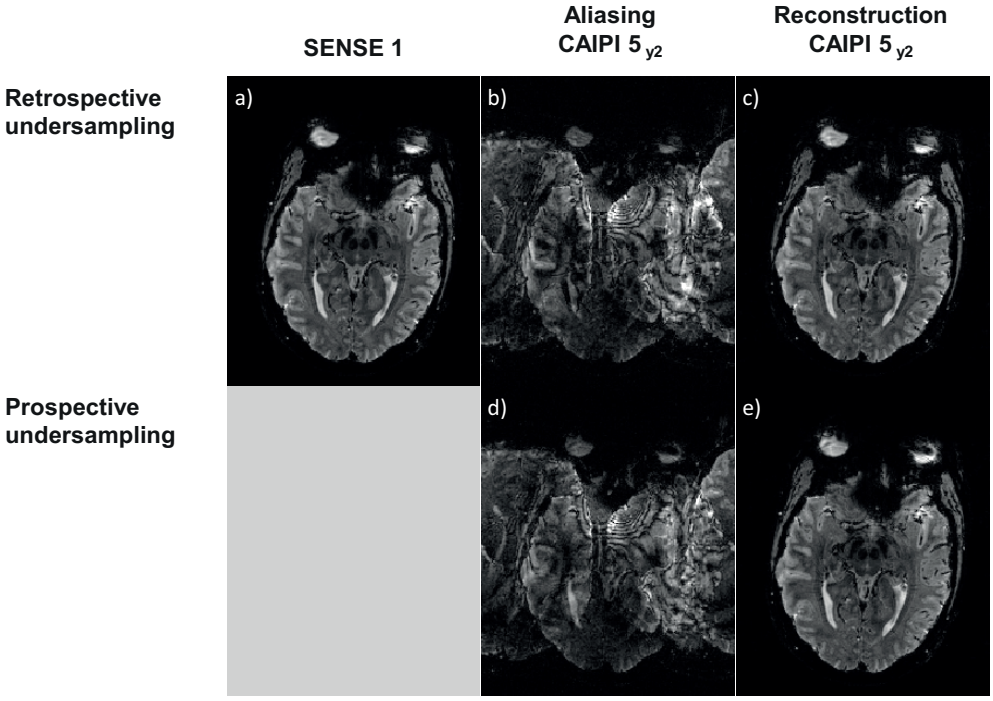


**Figure 3: Comparison of retrospective undersampling (a-c) and prospective undersampling (d,e) of 1 mm isotropic 3D $T_2$* weighted anatomy images. A full non-undersampled SENSE 1 dataset (a) is acquired in 2:43 min and retrospectively undersampled in k-space with a 2D CAIPIRINHA pattern. The result is displayed in image domain, as the summed aliased channels (b), and after applying the corresponding reconstruction (c). When comparing these with the prospective undersampled images (d,e) acquired in 33 sec, both methods look very similar, confirming a correct implementation of the shot selective 2D CAIPIRINHA sequence.**

To evaluate the performance of the 2D CAIPIRINHA implementation in comparison to SENSE acceleration, the resolution of 3D EPI whole brain $T_2$* weighted anatomical scans was pushed down to 0.5 millimeter isotropic. The $T_2$* weighted anatomical scans are displayed in Figure 4. One slice through the lower part of the brain is depicted that shows the deeper brain structures. Both a fully sampled dataset of 10:05 minutes (Figure 4a) and undersampled SENSE and CAIPIRINHA datasets are displayed (Figure 4b-d). The undersampling patterns used are SENSE 4 acquired in 2:31 min (Figure 4b), CAIPI 7 acquired in 1:27 min (Figure 4c) and SENSE 7 acquired in 1:27 min (Figure 4d). Note that both SENSE and CAIPIRINHA can be used to shorten the total scan time substantially. However, at an acceleration factor of 7, the SENSE image is heavily spoiled by artifacts, while the 2D CAIPIRINHA image still preserves the anatomy of the brain, allowing the scan time to be shortened even further.

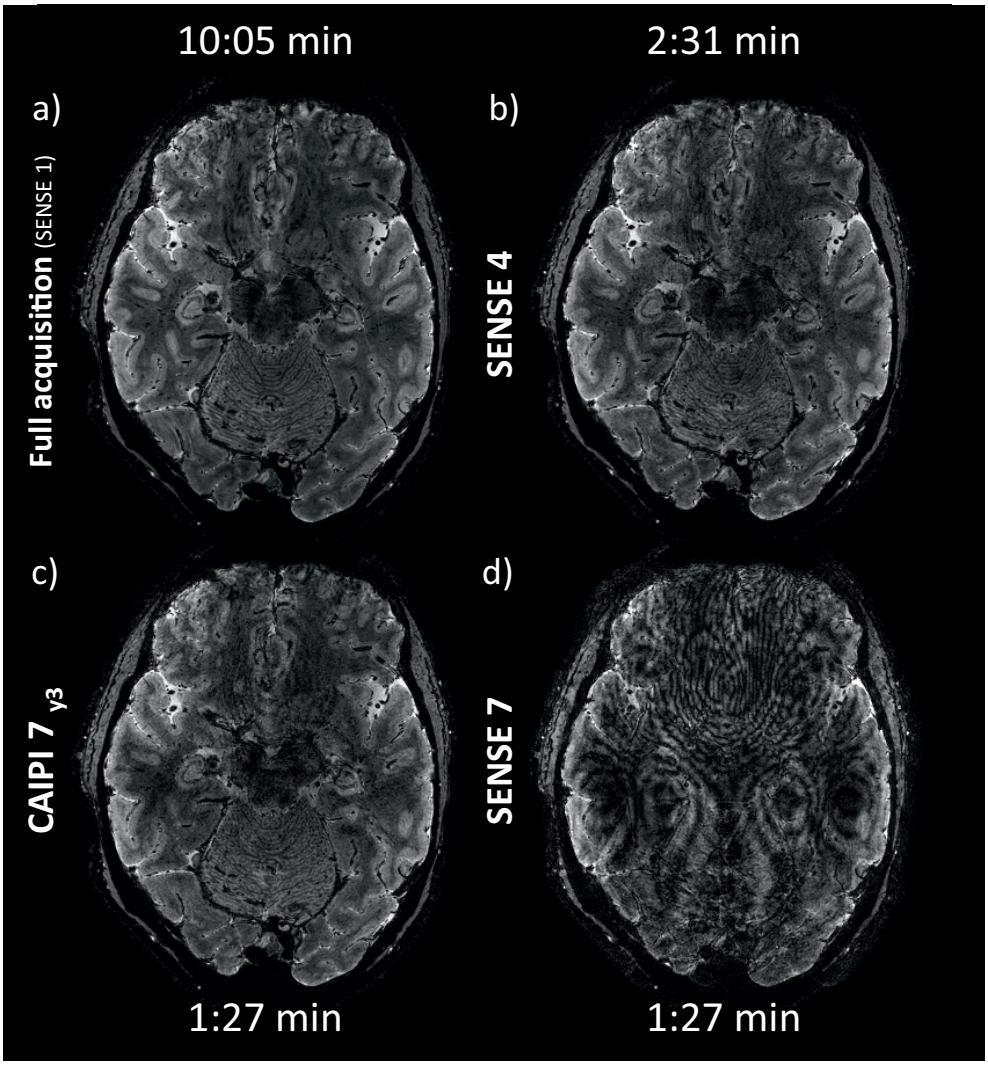


**Figure 4: Whole brain $T_2$* anatomy scans acquired with multi-shot 3D EPI sequences. Example slices are displayed for (a) fully sampled data, (b) SENSE 4, (c) CAIPI 7 (d) and SENSE 7. The resolution of the scans is 0.5 mm isotropic. The fully sampled data takes 10:05 min to acquire, whereas the SENSE and CAIPIRINHA methods are able to significantly shorten the scan time to 2:31 min and 1:27 min respectively. Note that even with the shortened scan time, the detailed brain structures are still visible for the CAIPIRINHA scan, in contrast to the SENSE 7 scan, which is spoiled by artifacts.**

## Combination with high density receive arrays, 3D EPI functional imaging

Example fMRI scans, acquired with a combination of high density receive arrays and a 2D CAIPIRINHA sequence, are shown in detail in Figure 5. Both, CAIPIRINHA (Figure 5a) and SENSE undersampling (Figure 5b) are shown. For each dataset, 8 axial slices of the visual cortex

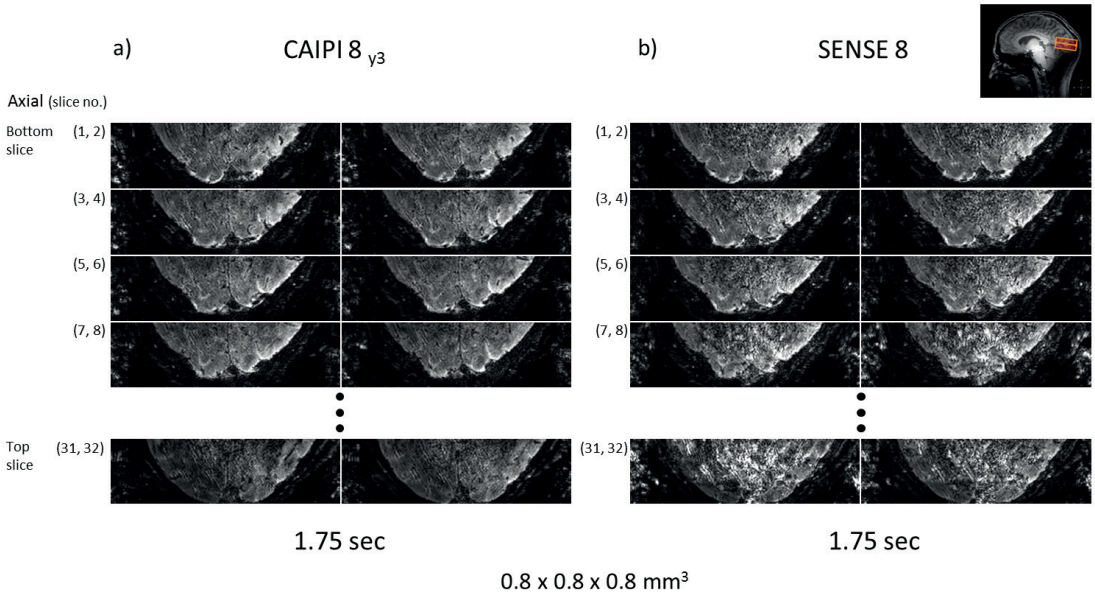


**Figure 5: 3D EPI scans of the visual cortex, acquired with the high density receive arrays in combination with (a) 2D CAIPIRINHA and (b) SENSE. Displayed are eight stacked slices from the visual cortex, as well as the outer two top slices. Both datasets have an acceleration factor of 8, a total acquisition time of 1.75 sec and a resolution of 0.8 mm isotropic. The positioning of the imaging volume is shown in the figure inset (top right). Note that the 2D CAIPIRINHA data contains less artifacts and less noise amplification as compared to the SENSE data. However, the outer two axial slices (lower row) contain artifacts for both SENSE and 2D CAIPIRINHA.**

are selected as well as the upper two axial slices. Note that the CAIPIRINHA scans contain less noise amplification and unfolding artifacts as compared to the SENSE scans. However, artifacts are still seen in both datasets for the outer two top slices. The g-factor maps (Figure 6) confirm a reduction of the noise amplification factor when using CAIPIRINHA, especially in the center of the visual cortex. To illustrate the different possibilities for fMRI imaging with a high spatial and high temporal resolution, different combinations of sub-millimeter imaging of the visual cortex are displayed in Figure 7. A fully sampled (SENSE 1) acquisition is displayed on the left (Figure 7a,f). The accelerated CAIPIRINHA acquisitions (Figure 7b-d) have varying scan parameters (as indicated in the figure). The range of the acquired resolutions is 0.70-0.99 mm, the dynamic scan time is 0.82 - 3.28 sec, and the coverage is 12 - 32 slices. As the resolution improves, the scan time increases as well. Note that it is possible to perform sub-millimeter and sub-second EPI imaging of the visual cortex, without losing significant image quality (Figure 7b,c), in contrast to using SENSE (Figure 7e).

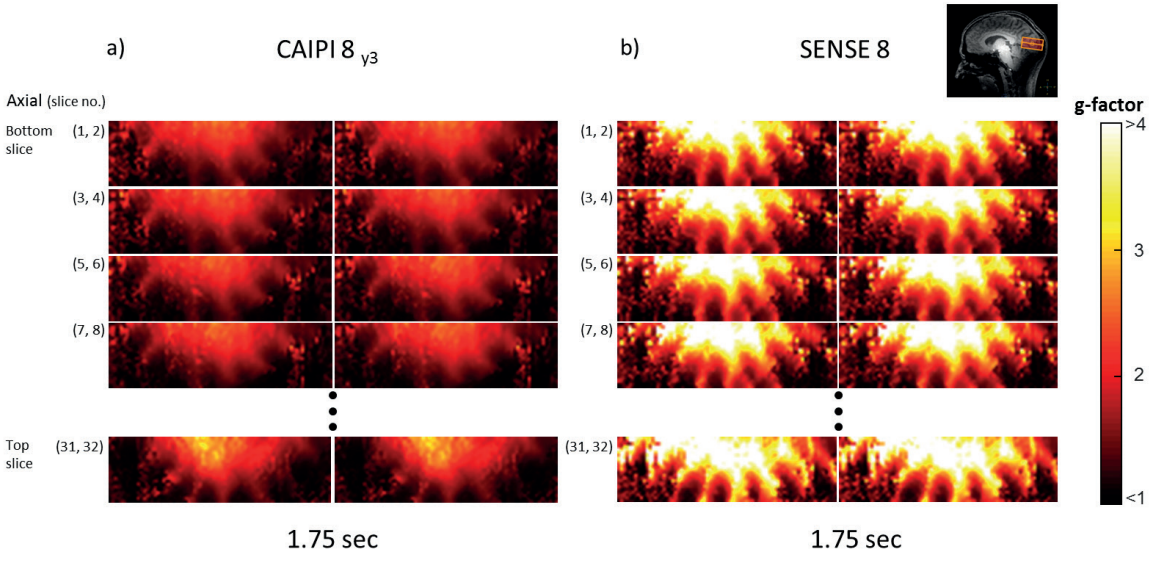


**Figure 6: g-factor maps of the visual cortex acquired with the high density receive arrays in combination with (a) 2D CAIPIRINHA and (b) SENSE. The selected g-factor maps correspond with the 3D EPI scans and slices shown in Figure 5 at an acceleration factor of 8. For every slice, the average g-factor is lower when acquired with 2D CAIPIRINHA, as compared to SENSE. This effect is especially visible in the center of the visual cortex, resulting in a reduction of noise when using 2D CAIPIRINHA.**

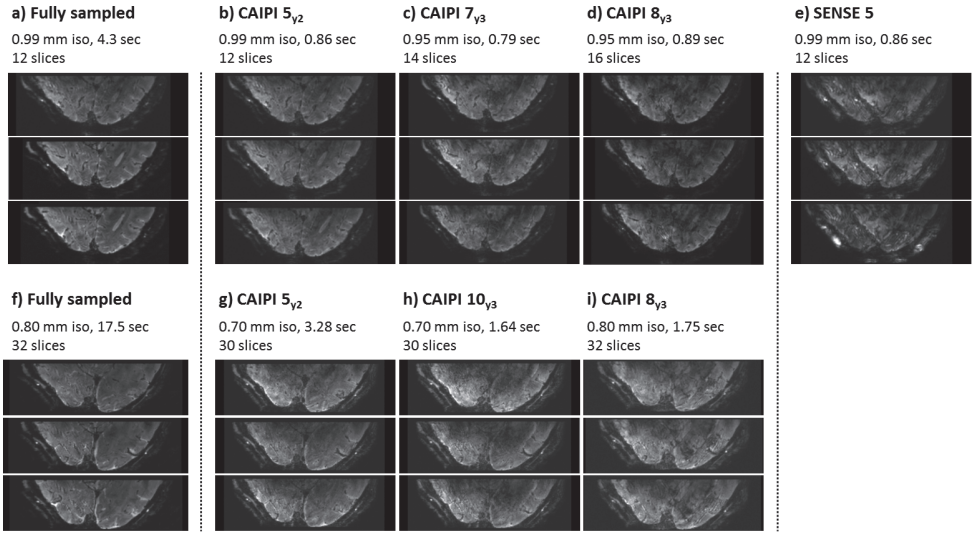


**Figure 7: 3D EPI scans of the visual cortex acquired with different settings for resolution, scan time and imaging coverage (scaled differently for visualization). The specified voxel-size is isotropic (iso). The same 3 slices are displayed for both the fully sampled SENSE 1 datasets (a,f) and the accelerated datasets (b-e, g-i). Note that it is possible to scan with both a high spatial resolution (< 1 mm) and a high temporal resolution (< 1 sec) combined.**

## Discussion

This study aimed to push spatial and temporal resolution of 7T MRI by combining high density receive arrays with a 2D CAIPIRINHA sequence for multi-shot 3D EPI scans. A shot selective 2D CAIPIRINHA sequence for multi-shot 3D EPI scans was implemented, which, instead of adding extra gradients, leaves them out. With the 2D CAIPIRINHA sequence it was possible to reduce the scan time of high resolution $T_2$* weighted anatomical scans, confirming an accurate sequence implementation. When combining high density receive arrays and 2D CAIPIRINHA it was possible to acquire sub-millimeter, sub-second 3D EPI scans of the visual cortex. The image quality of the CAIPIRINHA acquisitions was improved, as compared to SENSE acquisitions with the same resolution and scan time. The results are discussed in further detail below. First, the implementation of the 2D CAIPIRINHA sequence is discussed, as evaluated from the acquired $T_2$* weighted 3D EPI anatomical images. Afterwards, the combination of high density receive arrays and 2D CAIPIRINHA is discussed, focusing on its potential to accelerate sub-millimeter fMRI acquisitions.

### Evaluation of sequence implementation, $T_2$* weighted 3D EPI anatomical imaging

The $T_2$* weighted 3D EPI anatomical scans acquired with the standard receive setup show that the shot selective 2D CAIPIRINHA sequence for multi-shot 3D EPI scans was implemented appropriately. Several EPI shots of a multi-shot interleaved 3D EPI sequence were selectively skipped resulting in a CAIPIRINHA sampling pattern and a reduction of scan time. The sequence is simple and straightforward to implement, since no additional gradients or RF pulses are required, as compared to a multi-shot interleaved 3D EPI sequence. The implementation resulted in the expected image quality, as evaluated by comparing prospective and retrospectively undersampled datasets. These datasets are in agreement, as can be seen by the similarities of both the aliasing patterns and the reconstructed images. When the sequence is used to acquire anatomical scans with an isotropic resolution of 0.5 mm, the total scan time can be shortened significantly. The total scan time can be reduced by a factor of 4, as compared to an earlier optimized implementation of 6 min for whole brain $T_2$* weighted 3D EPI anatomy scans at 7T [26]. The application of the shot selective CAIPIRINHA implementation is broad. For example it can also be used at other field strengths in clinical routine to reduce scan time of 3D EPI anatomical scans when acquired with multi-element receive coils.

### Combination with high density receive arrays, 3D EPI functional imaging

The combination of high density receive arrays and a 2D CAIPIRINHA sequence made it possible to acquire sub-millimeter 3D EPI scans of the visual cortex with a dynamic scan time of less than 1 second. Multiple scans with different settings for a high resolution and a short scan time were acquired. In literature, sub-millimeter functional imaging is often characterized by relatively slow repetition time. In other previous work, high resolution fMRI data of 0.7 mm isotropic was acquired in 4 seconds [27]. In this study, using a similar scan protocol as Fracasso

et al. but incorporating CAIPIRINHA, we were able to push down the scan time of data with 0.7 mm resolution to 1.64 sec. Though, note that some slices contain aliasing artifacts due to the high acceleration factor.
When comparing CAIPIRINHA and SENSE acquisitions with identical acquisition parameters (Figure 5-7), CAIPIRINHA outperforms SENSE. For 0.8 mm isotropic 3D EPI scans of the visual cortex with a (dynamic) scan time of 1.75 sec, the noise amplification is reduced especially in the center of the visual cortex. This is visible both in the reconstructed images (Figure 5) as well as in the g-factor maps (Figure 6). For both methods unfolding artifacts due to the high acceleration can still be seen at the outer two top slices of the dataset acquired at 0.8 mm isotropic resolution (Figure 5). These artifacts are less dominant in the CAIPIRINHA dataset as compared to SENSE. Overall, despite the already high achievable acceleration factor when using high density receive arrays, it is possible to further increase the acceleration factor by combing the high density receive arrays with a shot selective 2D CAIPIRINHA sequence.

## Position in literature

The novelty of this study is the combination of high density receive arrays and a 2D CAIPIRINHA sequence for 3D EPI scans, to push MRI resolutions to a sub-second and sub-millimeter scale. However, the concept of 2D CAIPIRINHA for 3D EPI scans on itself has been reported before [14,15]. The shot selective 2D CAIPIRINHA part of this study is therefore an expansion on a previously reported concept. There are other promising approaches to achieve similar or potentially even higher spatial and a temporal resolution for MRI. These approaches include sequence design as well as hardware developments. Recent efforts aim to increase the number of channels for whole brain coverage at high fields [28-30] similar to lower fields [31,32]. Combined with advanced acceleration schemes, these can further improve fMRI sensitivity and specificity by enabling high spatiotemporal resolution. Another approach is to use insert gradients for head imaging. Insert gradients allow fast switching of strong gradients which can reduce the length of the EPI readout train thereby enhancing temporal resolution [33]. The current study used 2D CAIPIRINHA for 3D EPI sequences, though recently big steps have been made with methods that use simultaneous multi-slice approaches [18], such as multiband [34], blipped CAIPI [22], and the more recent wave-CAIPI [35] that extends the CAIPIRINHA principle to all three spatial encoding dimensions. Other approaches focus more on the excitation side of the sequence. Selective RF excitation can be used to either reduce the field of view, or to reduce parallel imaging noise amplification [36], which has already been combined with the benefits of a 3D CAIPI EPI sequence [37].

## Considerations

In this study, the achieved gains from high density receive arrays and 2D CAIPIRINHA were used to shorten scan time of high resolution 3D EPI scans. However, the gains can be used in different ways, not only to reduce scan time, but also to increase the amount of slices or

imaging coverage (FOV). The results are promising, but the methods can be further optimized in the future, since artifacts are present in the some CAIPIRINHA datasets, as can be seen in the top slices of Figure 5. In fact these may suggest imperfect slab excitations, which could maybe also explain the artifacts of Figure 4 SENSE 7. In this study a shot selective 2D CAIPIRINHA sequence for multi-shot 3D EPI scans is used. The sequence is practical to implement, since it mainly involves removing selected EPI shots from a multi-shot 3D EPI sequence. No additional gradients or RF pulses are required, in contrast to current literature where typically gradient blips on the z-axis are used or SAR demanding multiband RF pulses. As the current implementation does not use additional gradients, most EPI phase corrections do not require modification as compared to multi-shot 3D EPI sequences, simplifying the implementation. A disadvantage of the current implementation is that the undersampling factor is directly connected to the EPI factor, which reduces the freedom of choice in the sequence settings. For example, the acquisition of a 3D volume with a single EPI shot is not possible with the current implementation. Despite the high acceleration factors achieved in this study, there might be more advantageous applications for CAIPIRINHA. In our study we used reduced FOV acquisitions (as commonly acquired with surface coils), this can be considered as a non-ideal case for combination with CAIPIRINHA, since CAIPIRINHA exploits the ability to shuffle sensitivity variations over a (large) FOV relative to the coil sensitivity profiles. On the other hand, this study does use a large channel count of 32 receivers, which does further enhance the benefits of CAIPIRINHA.

## Conclusion

To investigate the combination of high density receive arrays and 2D CAIPIRINHA, a shot selective 2D CAIPIRINHA sequence is implemented. With this sequence it is possible to reduce the scan time of high resolution $T_2$* weighted anatomical 3D EPI scans. When high density receive arrays are combined with the 2D CAIPIRINHA sequence, the scan time and image quality of sub-millimeter 3D EPI (fMRI) scans of the visual cortex is improved. Multiple prospectively undersampled sub-millimeter and sub-second 3D EPI scans of the visual cortex are obtained, combining both a high temporal resolution and a high spatial resolution, which is essential to further examine dynamic and spatially detailed brain functions with fMRI. Overall, high density receive arrays in combination with shot selective 2D CAIPIRINHA for 3D EPI scans prove to be valuable for reducing scan time of sub-millimeter (and sub-second) fMRI acquisitions.

## References


1. Dumoulin SO, Fracasso A, van der Zwaag W, Siero JCW, Petridou N. Ultra-high field MRI: Advancing systems neuroscience towards mesoscopic human brain function. Neuroimage 2018;168:345-357.
2. Setsompop K, Feinberg DA, Polimeni JR. Rapid brain MRI acquisition techniques at ultra-high fields. NMR Biomed 2016;29(9):1198-1221.
3. van der Zwaag W, Schafer A, Marques JP, Turner R, Trampel R. Recent applications of UHF-MRI in the study of human brain function and structure: a review. NMR Biomed 2016;29(9):1274-1288.
4. Lin FH, Polimeni JR, Lin JL, Tsai KW, Chu YH, Wu PY, Li YT, Hsu YC, Tsai SY, Kuo WJ. Relative latency and temporal variability of hemodynamic responses at the human primary visual cortex. Neuroimage 2018;164:194-201.
5. Petridou N, Siero JCW. Laminar fMRI: What can the time domain tell us? Neuroimage 2017.
6. Yoo PE, John SE, Farquharson S, Cleary JO, Wong YT, Ng A, Mulcahy CB, Grayden DB, Ordidge RJ, Opie NL, O'Brien TJ, Oxley TJ, Moffat BA. 7T-fMRI: Faster temporal resolution yields optimal BOLD sensitivity for functional network imaging specifically at high spatial resolution. Neuroimage 2018;164:214-229.
7. Breuer FA, Blaimer M, Heidemann RM, Mueller MF, Griswold MA, Jakob PM. Controlled aliasing in parallel imaging results in higher acceleration (CAIPIRINHA) for multi-slice imaging. Magn Reson Med 2005;53(3):684-691.
8. Breuer FA, Blaimer M, Mueller MF, Seiberlich N, Heidemann RM, Griswold MA, Jakob PM. Controlled aliasing in volumetric parallel imaging (2D CAIPIRINHA). Magn Reson Med 2006;55(3):549-556.
9. Jurrissen M, Fuderer M, van den Brink J. Diamond-SENSE: undersampling on a crystallographic grid. Proceedings of the 12th Annual Meeting of the ISMRM, Kyoto, Japan; 2004; Kyoto, Japan. p 2643.
10. Barth M, Breuer F, Koopmans PJ, Norris DG, Poser BA. Simultaneous multislice (SMS) imaging techniques. Magn Reson Med 2016;75(1):63-81.
11. Huber L, Handwerker DA, Jangraw DC, Chen G, Hall A, Stuber C, Gonzalez-Castillo J, Ivanov D, Marrett S, Guidi M, Goense J, Poser BA, Bandettini PA. High-Resolution CBV-fMRI Allows Mapping of Laminar Activity and Connectivity of Cortical Input and Output in Human M1. Neuron 2017;96(6):1253-1263 e1257.
12. Poser BA, Koopmans PJ, Witzel T, Wald LL, Barth M. Three dimensional echo-planar imaging at 7 Tesla. Neuroimage 2010;51(1):261-266.
13. van der Zwaag W, Marques JP, Kober T, Glover G, Gruetter R, Krueger G. Temporal SNR characteristics in segmented 3D-EPI at 7T. Magn Reson Med 2012;67(2):344-352.
14. Narsude M, Gallichan D, van der Zwaag W, Gruetter R, Marques JP. Three-dimensional echo planar imaging with controlled aliasing: A sequence for high temporal resolution functional MRI. Magn Reson Med 2016;75(6):2350-2361.
15. Poser BA, Ivanov D, Kannengiesser SA, Uludag K, Barth M. Accelerated 3D EPI using 2D blipped-CAIPI for high temporal and/or spatial resolution. Proceedings of the 22th Annual Meeting of the ISMRM, Milan, Italy; 2014. p 1506.
16. Pruessmann KP, Weiger M, Scheidegger MB, Boesiger P. SENSE: sensitivity encoding for fast MRI. Magn Reson Med 1999;42(5):952-962.
17. Griswold MA, Jakob PM, Heidemann RM, Nittka M, Jellus V, Wang J, Kiefer B, Haase A. Generalized autocalibrating partially parallel acquisitions (GRAPPA). Magn Reson Med 2002;47(6):1202-1210.
18. Feinberg DA, Vu AT, Beckett A. Pushing the limits of ultra-high resolution human brain imaging with SMS-EPI demonstrated for columnar level fMRI. Neuroimage 2018;164:155-163.
19. Fracasso A, Luijten PR, Dumoulin SO, Petridou N. Laminar imaging of positive and negative BOLD in human visual cortex at 7T. Neuroimage 2018;164:100-111.

20. Petridou N, Italiaander M, van de Bank BL, Siero JC, Luijten PR, Klomp DW. Pushing the limits of high-resolution functional MRI using a simple high-density multi-element coil design. NMR Biomed 2013;26(1):65-73.
21. Zahneisen B, Ernst T, Poser BA. SENSE and simultaneous multislice imaging. Magn Reson Med 2015;74(5):1356-1362.
22. Setsompop K, Gagoski BA, Polimeni JR, Witzel T, Wedeen VJ, Wald LL. Blipped-controlled aliasing in parallel imaging for simultaneous multislice echo planar imaging with reduced g-factor penalty. Magn Reson Med 2012;67(5):1210-1224.
23. Blaimer M, Breuer FA, Seiberlich N, Mueller MF, Heidemann RM, Jellus V, Wiggins G, Wald LL, Griswold MA, Jakob PM. Accelerated volumetric MRI with a SENSE/GRAPPA combination. J Magn Reson Imaging 2006;24(2):444-450.
24. Koopmans PJ. Two-dimensional-NGC-SENSE-GRAPPA for fast, ghosting-robust reconstruction of in-plane and slice-accelerated blipped-CAIPI echo planar imaging. Magn Reson Med 2017;77(3):998-1009.
25. Ledden PJ, Mareyam A, Wang S, van Gelderen P, Duyn J. 32 Channel Receive-Only SENSE Array for Brain Imaging at 7T. Proceedings of the 15th Annual Meeting of the ISMRM, Berlin, Germany 2007 p 242 2007.
26. Zwanenburg JJ, Versluis MJ, Luijten PR, Petridou N. Fast high resolution whole brain T2* weighted imaging using echo planar imaging at 7T. Neuroimage 2011;56(4):1902-1907.
27. Fracasso A, Petridou N, Dumoulin SO. Systematic variation of population receptive field properties across cortical depth in human visual cortex. Neuroimage 2016;139:427-438.
28. Auerbach EJ, DelaBarre L, Van de Moortele PF, Strupp J, Gumbrecht R, Potthast A, Pirkl G, Moeller S, Hanna B, Grant AN, Adriany G, Uğurbil K. An integrated 32-channel transmit and 64-channel receive 7 tesla MRI system. Proceedings of the 25th Annual Meeting of the ISMRM, Hawaii, USA; 2017. p 1218.
29. Beckett AJS, Vu AT, Schillak S, Wald LL, Feinberg DA. A high density 24 channel array coil extendable to 48 channels for human cortical MRI at 7T. Proceedings of the 25th Annual Meeting of the ISMRM, Hawaii, USA; 2017. p 2654.
30. Hendriks AD, Luijten PR, Klomp DW, Petridou N. Potential acceleration performance of a 256-channel whole-brain receive array at 7 T. Magn Reson Med 2018;00:1-12 Epub ahead of print.
31. Keil B, Blau JN, Biber S, Hoecht P, Tountcheva V, Setsompop K, Triantafyllou C, Wald LL. A 64-channel 3T array coil for accelerated brain MRI. Magn Reson Med 2013;70(1):248-258.
32. Wiggins GC, Polimeni JR, Potthast A, Schmitt M, Alagappan V, Wald LL. 96-Channel receive-only head coil for 3 Tesla: design optimization and evaluation. Magn Reson Med 2009;62(3):754-762.
33. Weiger M, Overweg J, Rosler MB, Froidevaux R, Hennel F, Wilm BJ, Penn A, Sturzenegger U, Schuth W, Mathlener M, Borgo M, Bornert P, Leussler C, Luechinger R, Dietrich BE, Reber J, Brunner DO, Schmid T, Vionnet L, Pruessmann KP. A high-performance gradient insert for rapid and short-T2 imaging at full duty cycle. Magn Reson Med 2018;79(6):3256-3266.
34. Larkman DJ, Hajnal JV, Herlihy AH, Coutts GA, Young IR, Ehnholm G. Use of multicoil arrays for separation of signal from multiple slices simultaneously excited. J Magn Reson Imaging 2001;13(2):313-317.
35. Bilgic B, Gagoski BA, Cauley SF, Fan AP, Polimeni JR, Grant PE, Wald LL, Setsompop K. Wave-CAIPI for highly accelerated 3D imaging. Magn Reson Med 2015;73(6):2152-2162.
36. Mooiweer R, Sbrizzi A, Raaijmakers AJE, van den Berg CAT, Luijten PR, Hoogduin H. Combining a reduced field of excitation with SENSE-based parallel imaging for maximum imaging efficiency. Magn Reson Med 2017;78(1):88-96.
37. van der Zwaag W, Reynaud O, Narsude M, Gallichan D, Marques JP. High spatio-temporal resolution in functional MRI with 3D echo planar imaging using cylindrical excitation and a CAIPIRINHA undersampling pattern. Magn Reson Med 2018;79(5):2589-2596.

# Chapter 3

## Potential acceleration performance of a 256-channel whole-brain receive array at 7T

Arjan D. Hendriks,
Peter R. Luijten,
Dennis W.J. Klomp,
Natalia Petridou

**Based on publication:** Hendriks A.D., Luijten P.R., Klomp D.W.J., Petridou N., Potential acceleration performance of a 256-channel whole-brain receive array at 7T. Magn Reson Med 2018. DOI: 10.1002/mrm.27519 *Epub ahead of print*

## Abstract

**Purpose:** Assess the potential gain in acceleration performance of a 256 channel versus 32 channel receive coil array at 7T in combination with a 2D CAIPIRINHA sequence for 3D datasets.

**Methods:** A 256 channel receive setup was simulated by placing two small 16 channel high density receive arrays at 2x8 different locations on the head of healthy participants. Multiple consecutive measurements were performed and coil sensitivity maps were combined to form a complete 256 channel dataset. This setup was compared with a standard 32 channel head coil, in terms of SNR, noise correlation, and acceleration performance (g-factor).

**Results:** In the periphery of the brain, receive SNR was on average a factor 1.5 higher (ranging up to a factor 2.7 higher) than the 32 channel coil, in the center of the brain SNR was comparable or lower, depending on the size of the ROI, with a factor 1.0 on average (ranging from 0.7 up to a factor of 1.6). Average noise correlation between coil elements was 3% for the 256 channel coil, and 5% for the 32 channel coil. At acceptable g-factors (<2), the achievable acceleration factor using SENSE and 2D CAIPIRINHA, was 24 and 28 respectively, versus 9 and 12 for the 32 channel coil.

**Conclusion:** The receive performance of the simulated 256 channel array was better than the 32 channel reference. Combined with 2D CAIPIRINHA, a peak acceleration factor of 28 was assessed, showing great potential for high density receive arrays.

**Keywords:** phased array, 256 channel receive coil, parallel imaging, massive receive, 2D CAIPIRINHA, 7T

## Introduction

The concept of using arrays of multiple receive coil elements to enhance signal-to-noise ratio (SNR) is already around for a couple of decades [1]. Receive arrays can greatly enhance SNR in brain imaging, as compared to the use of a standard quadrature head coil covering the same area [2]. The benefits of using up to 32 receive elements for brain imaging have been demonstrated extensively [3-8]. However, just a few brain imaging studies have explored the advantages of receive coils with more than 32 elements [9,10].

When combined with parallel imaging, the improved SNR from receive coil arrays can be traded for a faster acquisition time, enhancing the temporal resolution, while maintaining high spatial resolution. When examining dynamic and spatially detailed brain functions using functional MRI (fMRI), the combination of both a high temporal resolution and a high spatial resolution is essential. High density receiver arrays allow for high acceleration factors with reduced g-factors and very high resolutions [11,12]. However, fMRI with both a high temporal resolution (< 1 sec) and a high spatial resolution (< 1 mm) combined, is rarely seen, despite the latest developments in the field of parallel imaging and modern imaging setups.



From theory, the benefit of increasing the number of receive elements is two-fold. First, a gain in SNR can be achieved [2]. Second, it enables improved encoding acceleration performance [13], as can be exploited by using parallel imaging techniques.
The number of receive elements can be increased and the coil size can be reduced accordingly, as long as the individual coils are in tissue load dominance and coil resistance losses are minimal [14,15]. This would result in an improved SNR close to the coils, with hardly losing sensitivity further away from the coils [10,16]. If the individual coils are made too small, (electronic) coil resistance loss dominates the sample noise [17], which would degrade the total SNR. This relation determines that there is an optimal number of coils at which the achievable SNR is maximized. Different 3T studies use receive arrays with high numbers of receive elements, sometimes also referred to as massively parallel MRI detection [18], and show a clear benefit in using 64 receive channels [9,19], 96 channels [10] and even 128 channels [20,21].

The theoretical maximum achievable SNR limit, described as the ultimate SNR, is investigated by previous studies [22,23]. These studies simulate a spherical object at varying field strengths, sphere sizes and acceleration factors. Among other results, it was shown that a 32 channel receive setup at 3 tesla already closely approaches the ultimate SNR in the center of the phantom, but is still far away from the ultimate SNR at the regions nearby the surface of the phantom. Additionally, at higher field strengths, such as 7 tesla, the difference between the SNR acquired with 32 channels and the ultimate SNR increases, and more coils would be required to approach the ultimate SNR at both the surface of the phantom and at intermediate distance from the center. In contrast to increasing the number of receive elements, present-

day efforts in the MRI community are geared towards parallel imaging techniques [24-26]. These techniques can greatly reduce the total acquisition time, pushing the limits of temporal and spatial resolution. Parallel imaging techniques reduce acquisition time by uniformly undersampling k-space data acquired with receive arrays, while maintaining the maximum k-values to keep the full spatial resolution. Early and widely implemented parallel imaging techniques are SENSE [27], GRAPPA [28] and the more recent CAIPIRINHA [29]. When using the undersampling patterns of 2D CAIPIRINHA [30], aliasing patterns can be controlled, posing less restriction on coil sensitivity variations. Specifically, the noise amplification due to receiver coil configuration and geometry (g-factor) can be reduced.

Ultra-high field strengths have the commonly acknowledged advantage of an intrinsic SNR gain and an increase in BOLD sensitivity. In addition, at ultra-high field strength the RF eddy current interaction with human tissue enhances the spatial variance of $B_1^-$ fields [31,32], paving the way to higher acceleration factors as well [23]. This interaction also increases the tissue load dominance of the receive coils, meaning that smaller coil elements can be used without contributing substantially to the noise (i.e. low noise figure; [33]). At 7T, when positioned close to the human head, coil elements can be as small as 2 $cm^2$, with a noise contribution of less than 20% [12]. Considering the surface area of the head, the number of coil elements for full brain MRI could potentially be increased from 96 at 3T to about 256 at 7T without contributing substantial extra noise. Moreover, realization of such a 256 channel array comes closer with the recent developments around the implementation of a digital receive pipeline for 7T scanners [34]. Despite these technical advances and theoretical predictions, it still has to be demonstrated that higher numbers of small receive elements can contribute substantially to acceleration for whole brain imaging at 7T.

The aim of this study is, to investigate the possible acceleration performance of a 256 channel receive coil array at 7T in combination with the parallel imaging methods SENSE and 2D CAIPIRINHA, for 3D datasets. Measurements were performed with 2x16 channel arrays, which were shifted over the head to simulate a 256 channel receive coil array. As a reference, the achieved sensitivity and acceleration performance is compared with a 32 channel head coil at 7T, for both parallel imaging methods. In line with observations of SENSE-optimized RF coils [35,36], we opted for a receive array design with gaps between the circumferentially distributed coil elements. Alternatively, overlapped designs could show higher non-accelerated SNR at the periphery, though at the cost of increased g-factors at high acceleration. A gapped design was used to improve SENSE performance, as this study focused on maximizing the acquisition acceleration at maintained SNR rather than increasing intrinsic SNR without acceleration.

# Methods

## Overview

A 256 channel receive array was simulated, by shifting two small 16 channel high density receive arrays to different locations on the head of healthy participants. On the same day a measurement with a standard Nova 32 channel receive coil setup (details below) was performed, which was taken as a reference. To check reproducibility, the measurement session was repeated with a second participant for both setups. Prior to scanning, the participants gave written informed consent, as required by the ethical committee of the University Medical Center Utrecht. Coil sensitivity reference scans and noise pre-scans were used to obtain the data. In post processing steps, SNR maps, noise correlations and g-factor maps were calculated for both coil setups (simulated 256 channel setup, standard head coil setup) as well as for the two parallel imaging techniques (2D SENSE, 2D CAIPIRINHA).



## Setup

A 7T Achieva MRI scanner (Philips Healthcare, Best, the Netherlands) was used for data acquisition in combination with a volume transmit/receive (T/R) coil (Nova Medical, Wilmington MA, USA), driven by 2x 4kW amplifiers. The volume T/R coil provided whole brain excitation. This system was equipped with the following two receive-only setups, consecutively.

The first receive setup consisted of two high density 16 channel receive arrays (MR Coils BV, Zaltbommel, the Netherlands). The receive coil array consisted of small, 1.5 x 2 $cm^2$, elements arranged in four flexible modules of four elements each (Figure 8), which were overlapped (0.5 cm). The elements were decoupled from one another by high impedance preamplifier decoupling. Each module had an outer dimension of 2 x 8 $cm^2$ and was flexible so that it could be positioned within 1 mm from the head. The use of passive detuning circuitry and fuses was avoided, because this would degrade the unloaded Q factor of the coil too much. For safety, active real-time PIN diode control surveillance was added, to immediately stop the scanner when the diode control demonstrated a malfunction. Previous publications [12,37,38] describe and evaluate the high density receive arrays in more detail, for completeness we also checked the unloaded and loaded Q-values of the coil element.
The second receive setup consisted of a standard 32 channel receive head coil (Nova Medical, Wilmington MA, USA). This coil array was used as the reference for comparison with the simulated 256 channel array. The 32 channel coil array consists of large square loops of approximately 5 x 4 $cm^2$. For decoupling purposes the coil elements are overlapping by 1 cm in the feet-head (FH) direction. The coil elements are arranged in 10 modules of 2-4 loops. Additional details of this receive coil were published previously [39]. Both receive setups were connected to the same preamplifiers and receive pipeline, to make the noise figures of the pre-amplifiers comparable.

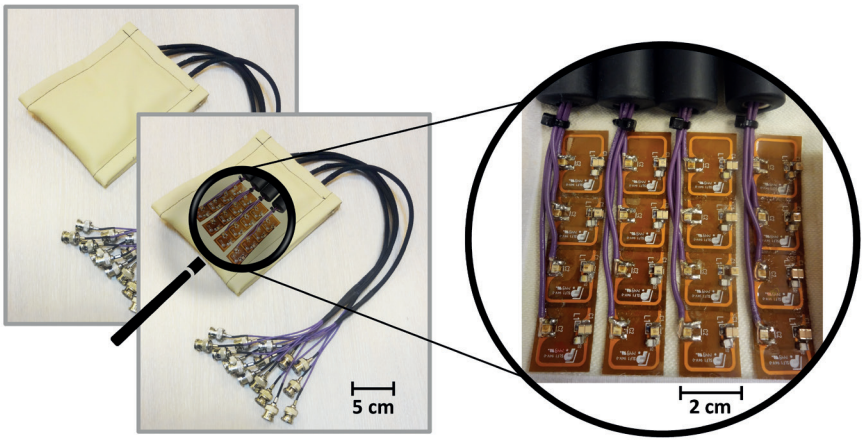


**Figure 8: Two high density receive arrays with 16 channels each (left), and a zoomed image of the coil elements (right). These coil arrays can be used for high spatial resolution and high temporal resolution fMRI imaging. However, with just 16 channels, the brain coverage of the arrays is limited. In this study, high density receive arrays are used to simulate a 256 channel coil with full brain coverage, by shifting the coils to different locations on the head as illustrated in Figure 9.**

## Measurement procedure

Two participants were scanned. For each participant, both the 2x16 channel receive array and the Nova 32 channel head coil setup were used consecutively. For both participants, the measurement procedure involved four steps.

First, an initial anatomical scan was acquired to position the imaging volume (3D gradient echo, TE/TR= 2.2/4.8 ms, voxel size: 1.5x1.5x1.5 $mm^3$, FOV: 25x25x20 $cm^3$, total acquisition time: 2 min). Second, to assess the performance of a 256 channel whole brain receive array, measurements were performed with two 16 channel receive arrays, which were positioned 8 times to 16 different locations on the head of the participant (Figure 9). For each location, a coil sensitivity reference scan (details below) with noise pre-scan was acquired, yielding a total of 8 reference scans, each containing signal from 32 channels, contributing to the formation of a virtual 256 channel coil. Third, the two 16 channel receive arrays were shifted to every other possible combination of two arrays on 16 head positions $\binom{16}{2}$. For each combination, a short noise scan was performed. In total 120 noise scans were required. The noise scan was a Philips pre-scan containing 20 000 noise points for each channel, acquired with a 400-kHz sampling rate. These noise points and the noise points of the 8 reference scans were used for the determination of the noise covariance and noise correlation between channels [40].

Finally, a measurement with the second receive setup was performed, which uses the standard

32 channel receive head coil. As this setup was connected to the same receive pipeline, the behavior of the pre-amplifiers and receiver gain settings was comparable. For this setup, a single reference scan with noise pre-scan was acquired for the same participant. In all scans, an automated power optimization was performed to assure that flip angles remained constant over the different setups. The transmit coil loading was comparable for the different receive setups. No substantial changes in the transmit power were observed, as changes in transmit power were within 5% range.

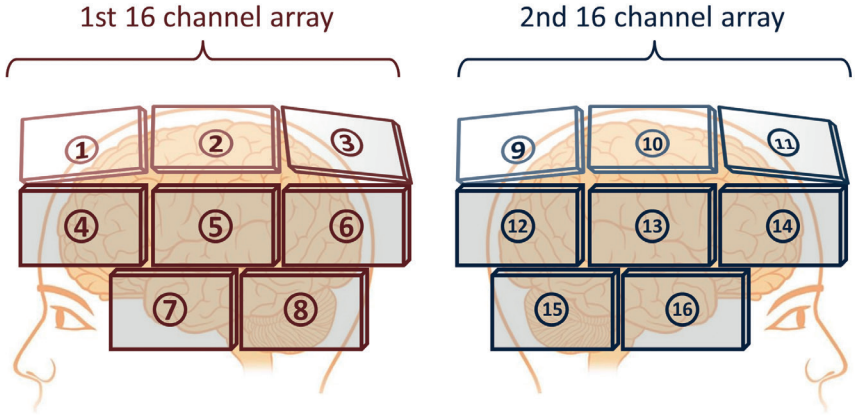


**Figure 9: A schematic of the how two 16 channel coil arrays were shifted to 16 different positions on the head, contributing to the 256 channel array simulation. To acquire all 256 sensitivity maps, only 8 reference scans (8 shifts of 32 channels) were needed. To acquire the all cross terms in the noise correlation matrix, 120 noise scans (120 shifts of 32 channels) were required.**

## Coil sensitivity reference scans

Coil sensitivity reference scans [27] were acquired by successive signal reception with the volume T/R coil and either the high density surface receive arrays or the standard head coil. Data from the reference scans contained information about the coil sensitivity for each coil element individually and also a 'background' image acquired by the volume T/R coil. Each reference scan contained a preceding noise scan. The reference scans were acquired with a 3D gradient echo sequence with the following parameters: TE/TR= 1.22/8.0 ms, a voxel size of 2x2x2 $mm^3$, a FOV of 20x20x20 $cm^3$, and a total acquisition time of 1 min.

## Post processing and simulations

After scanning, coil sensitivity maps were constructed from the coil sensitivity reference scans. The sensitivity maps were calculated using ReconFrame (GyroTools LLC, Zürich, Switzerland), by dividing the individual complex coil images by the complex image acquired with the volume coil [27].

The resulting 8 sets of 32 (2x16) channel sensitivity maps were combined to form a simulated 256 channel receive array. To correct for potential head displacement between the reference scans, images acquired for each coil position were aligned to the images of the first position using AFNI [41]. Alignment parameters (rotation & translation) were calculated using the reconstructed whole brain magnitude images from the reference scan. These alignment parameters were first applied to the whole brain complex images (to visually inspect the alignment quality) and then to the sensitivity matrices per coil position. The resulting 256 aligned coil sensitivity maps and individual coil images of the head formed the basis of the virtual head coil. The same procedure was applied to construct the sensitivity maps of the standard 32 channel head coil, with the exception that a coil alignment correction was not required in this case, since the signal from these 32 channels was already acquired simultaneously.

To analyze the data, SNR maps were calculated from the aligned individual complex coil images for both receive setups. The individual complex coil images were combined using SNR weighted channel addition, as described by the following equation:

$$SNR = \frac{\sum_{n=1}^{N_c} |w_n \; I_n|}{\sqrt{\sum_{n=1}^{N_c} (w_n^2 \; {\sigma_n}^2)}} \qquad w_n = \frac{|I_n|}{\sigma_n}$$

In this equation, $I_n$ defines the set of complex images of the $n^{th}$ individual coil element, $w_n$ are the weight factors that are spatially varying per voxel and per coil element, $N_c$ represents the total number of coil elements and $\sigma_n$ is equal to the standard deviation over the selected noise region for each coil element. The selected noise region consisted of more than 40 thousand points (18x18x128) for each coil element. The noise region was placed in the corner of each individual coil element image in image domain and care was taken to avoid placing the noise region over ghosting and filter artefacts. The SNR difference of the simulated 256 channel array compared to the 32 channel head coil was calculated by first aligning the two datasets and then dividing the same slices of both datasets. With the exception of noise correlation, the SNR maps could be compared directly, since the two receive setups were used together with the same transmit coil and were consecutively connected to the same receive pipeline (same receiver gain and pre-amplifiers). Three brain regions of interest (ROI) were analyzed, by segmenting the brain in a periphery ROI, a center ROI and a midpoint ROI, based on the anatomy of the reconstructed magnitude images of the reference scan. The 95% range and average gain factor in SNR, excluding noise correlation, was calculated for both regions. Additionally, axial SNR profiles trough the center of the brain were computed for both receive setups.

The noise covariance and noise correlation matrix were calculated from 120 separate noise scans and the 8 noise pre-scans included in the reference scans. The 8 noise pre-scans from

the reference scan were used to fill the 8 submatrices of 32 channels on the diagonal of the correlation matrix. The 120 separate noise scans were used to fill the remaining cross terms of the matrix. Since the noise scans were acquired consecutively, the noise coefficients were first calculated per scan individually, only correlating simultaneously acquired noise. Afterwards, the calculated noise coefficients of these separate scans were combined to form 1 matrix of 256 by 256 channels.

The g-factor was obtained from the sensitivity maps according to Pruessmann et al. [27]. The noise covariance matrix was included in the g-factor calculations, as a noise pre-whitening step. Since each individual sensitivity map was noise correlated with only 32 simultaneously acquired channels, only the inner eight 32-channel submatrices on the diagonal of the noise covariance matrix were required to pre-whiten the sensitivity maps for the g-factor calculations. To simulate the SENSE and CAIPIRINHA parallel imaging techniques, two directions were undersampled. These directions were anterior-posterior (AP) and feet-head (FH), as these directions contained the most coil elements. The range of the simulated undersampling factors (R) was 1 to 10 in the AP direction and 1-6 in the FH direction. Multiple g-factor calculations were performed for different combinations of 2D SENSE acceleration factors and different 2D CAIPIRINHA undersampling patterns. The reconstruction, required for the different undersampling patterns of 2D SENSE and 2D CAIPIRINHA, was in principle similar, only the indexing of the aliased voxels had to be adjusted.



## Results

An impression of the coil distribution of the 256 coil elements over the head can be seen in the surface rendered sum of the sensitivity maps (Figure 10a). The figure shows an intensity scaled 3D rendering of the acquired MR data. The 8x32 (256) coil array elements, with a loaded and unloaded Q of 89 and 248 respectively, fit the head of the participant and columns of overlapping elements can be clearly distinguished as lines over the head.

An evaluation of the performance of the simulated 256 channel receive coil array can be found in the cross sections of the SNR maps (Figure 10b-e). A sagittal and axial slice through the midsection of the brain are depicted, providing a representative overview of the SNR for the full 3D dataset, including the lower values in the center of the brain. SNR maps of both the simulated 256 channel receive array and the Nova 32 channel coil are displayed. Since both receive coil setups were attached to the same receive pipeline and only one transmit setup was used, the SNR maps can be compared between setups. Though, it should be noted that noise correlation could only be partially incorporated for the simulated 256 channel coil. In comparison with the standard head coil, especially at the periphery of the brain, the SNR for the simulated 256 channel coil is higher, which is seen for both slices illustrated.

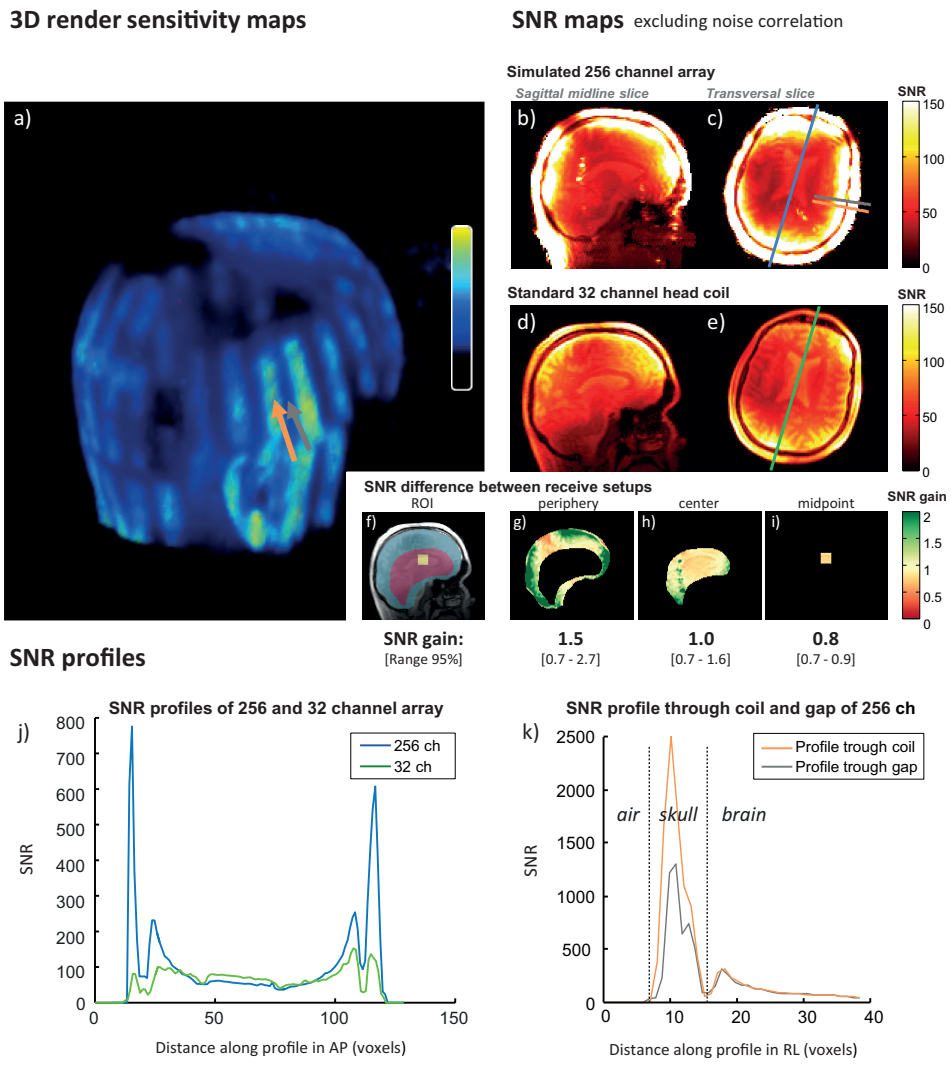


**Figure 10: Overview of the simulated 256 channel coil. The 3D render of combined sensitivity maps (a) was thresholded to display only the high sensitivity values, making the 256 coil elements visually observable as high intensity stripes over the head. The SNR of both the simulated 256 channel array and the standard 32 channel head coil is evaluated by comparing: SNR maps (b-e), SNR difference in three ROIs (f-i) and SNR profiles (j). Both the SNR maps, SNR difference ROIs and the SNR profiles show a pattern of a high SNR gain for the simulated 256 channel array in the periphery, a comparable SNR over a large part of the center of the brain, and a reduction in SNR in the worst-case midpoint of the brain. Additionally, SNR profiles (k) were drawn through a coil element (orange line) and through a gap (grey line) of the simulated 256 channel array. These profiles show that the non-uniformity in sensitivity caused by the coil gaps does not go much further than the skull. The locations of the selected profiles is also indicated in subfigures a and c.**

The SNR difference between the simulated 256 channel coil and the standard 32 channel coil is visualized by dividing the SNR maps of both setups. Center and periphery ROIs (Figure 10f), are drawn in the midsection slice to quantify the average and range of the SNR differences between setups (Figure 10g-i). In the brain periphery (Figure 10g), when partially neglecting the effects of noise correlation, the SNR difference for the simulated 256 channel coil as compared to the standard 32 channel coil is a factor of 1.5 on average, ranging from 0.7 (absence of coils) to 2.7 (close to coils). Moreover, directly next to the coils on the brain surface, higher gains in SNR are observed. In the center of the brain, when selecting a large central ROI (Figure 10h), the SNR difference is a factor 1.0 on average, ranging from 0.7 to 1.6 with an average of 1.0. In the worst-case midpoint of the brain (Figure 10i), there is a reduction of SNR, with a SNR difference of 0.8 on average, ranging from 0.7 to 0.9.



The SNR profiles (Figure 10j) show the same trend. High SNR values are found for the simulated 256 channel array in the skull and periphery of the brain, whereas the SNR is slightly lower in the middle of the brain when comparing both receive setups. For the 256 channel array, the SNR profiles that go through a gap between coil elements have similar SNR inside the brain, as profiles that go through a coil element itself (Figure 10k). The influence of the gaps between the coil elements on SNR remains superficial and does not reach much further than the skull.

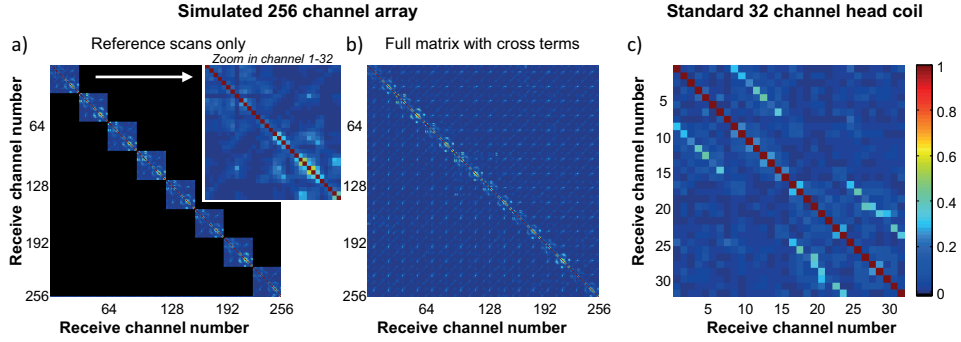


**Figure 11: The noise correlation matrix of the simulated 256 channel array is displayed, as acquired from the reference scans only (a) and when including the extra 120 noise scans (b). For comparison, the correlation matrix of the standard 32 channel head coil (c) is displayed as well. For visual inspection, a zoomed image of channel 1 to 32 of the 256 channel array is displayed in the figure insert of (a). The noise correlation matrix of the simulated 256 channel receive array was filled in blocks of 32 channels consecutively (and not simultaneously). 120 noise scans, obtained using different coil positions on the head, were required to measure all cross terms. When comparing both setups, note that the average noise correlation of the off-diagonal elements is similar for the 256 channel coil as compared to the 32 channel coil.**

The measured noise correlation matrix (Figure 11) is obtained from the 8 reference scans and the 120 subsequent noise scans acquired with the two 16-channel surface arrays. The noise correlation coefficients of the 8 reference scans are placed in 8 sub matrices of 32 channels on the diagonal (Figure 11a). The 120 noise scans were used to further fill all the cross-terms (Figure 11b). The overall noise correlation is low and similar across the elements. To illustrate this, the average magnitude and maximum magnitude of the noise correlation coefficients was calculated. For the simulated 256 channel array, the average of the off-diagonal noise correlation coefficients is 0.027 (2.7%, -31.5 dB). When only incorporating the noise coefficients which were measured together with the sensitivity maps (inner 8 sub-matrices of 32 channels), the average correlation is 0.065 (6.5%, -23.7 dB). For the standard 32 channel head coil the average noise correlation is 0.054 (5.4%, -25 dB). The maximum noise correlation coefficient is 0.67 for the simulated 256 channel coil and 0.42 for the standard 32 channel head coil.

The calculated g-factor maps when using SENSE undersampling patterns are shown for different acceleration factors, for both the standard 32 channel head coil (Figure 12, top) and the simulated 256 channel coil (Figure 12, bottom). The calculated g-factor maps when using 2D CAIPIRINHA undersampling patterns are shown as well (Figure 13). Different acceleration factors are displayed in the feet-head (FH) and anterior-posterior (AP) direction. At low, or no acceleration, the g-factor is similar for both setups. Overall, it can be seen that the g-factor, corresponding to noise amplification, increases with the acceleration factor. For both setups, the g-factor penalty diminishes when the total acceleration factor is distributed over two directions instead of one, by using either 2D SENSE (Figure 12) or 2D CAIPIRINHA (Figure 13). The increase in g-factor is spatially confined to the center of the brain for the simulated 256 channel coil, while more diffuse across the brain for the 32 channel head coil. The use of 2D CAIPIRINHA has a lower g-factor penalty than the use of SENSE, which is seen for both setups. When considering a g-factor of less than 2 (to avoid excessive noise amplification), the maximum achievable acceleration for the standard 32 channel head coil is: 9 (SENSE 3x3) and 12 (CAIPIRINHA $4x3_{\_FH2}$). For the simulated 256 channel head coil this is: 24 (SENSE 4x6) and 28 (CAIPIRINHA $4x7_{\_AP3}$). Note that even at very high accelerations (>28), the g-factor at the periphery of the brain is still below 2 for the 256 channel coil. As side-note, the SENSE and CAIPIRINHA maps are identical for the first 3 g-factor maps of the top row where the shift direction is not undersampled ($CAIPI_{dir}$: FH, $R_{FH}$: 1), since no k-space shift is performed in a direction without undersampling. The results are shown for a sagittal slice through the midsection of the brain, representative for the 'worst-case' situation. Slices that are positioned further away from the center have either an equal or better g-factor performance. Results are illustrated for one participant, similar results were obtained for the second participant.

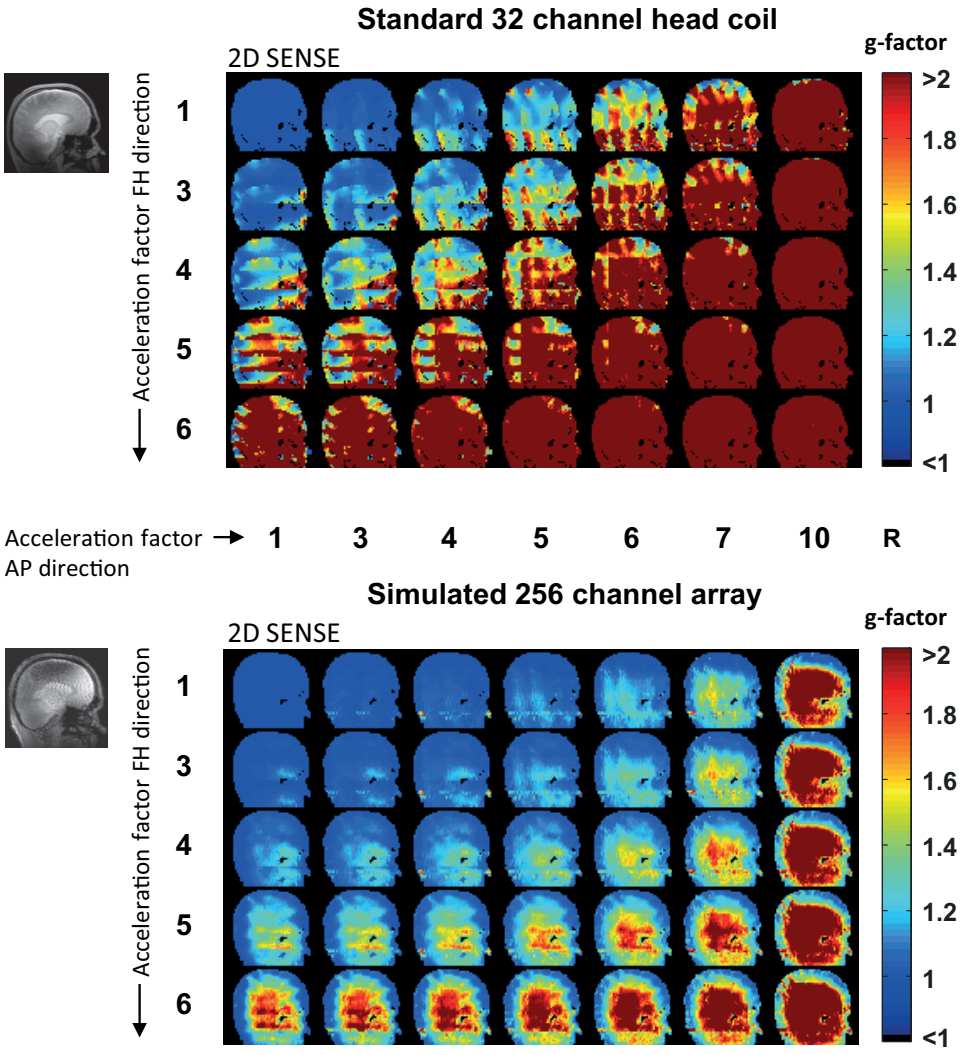


**Figure 12: g-factor maps for the standard head coil (top) and the simulated 256 channel receive array (bottom), using the undersampling patterns of 2D SENSE. Additionally, the two grayscale images (left) show the corresponding anatomical position of the selected slice located close to the midsection of the brain. The colored images show the g-factor maps, which are thresholded at a factor of 2 (color bar). The g-factor maps are displayed for different acceleration factors. The acceleration factor increases both in the FH direction (rows) and in the AP direction (columns). Note that the g-factor rises with the total acceleration factor. The maximum achievable acceleration, for g-factors smaller than 2, is for standard 32 channel head coil 9 (SENSE 3x3), and for the simulated 256 channel receive array 24 (SENSE 4x6).**

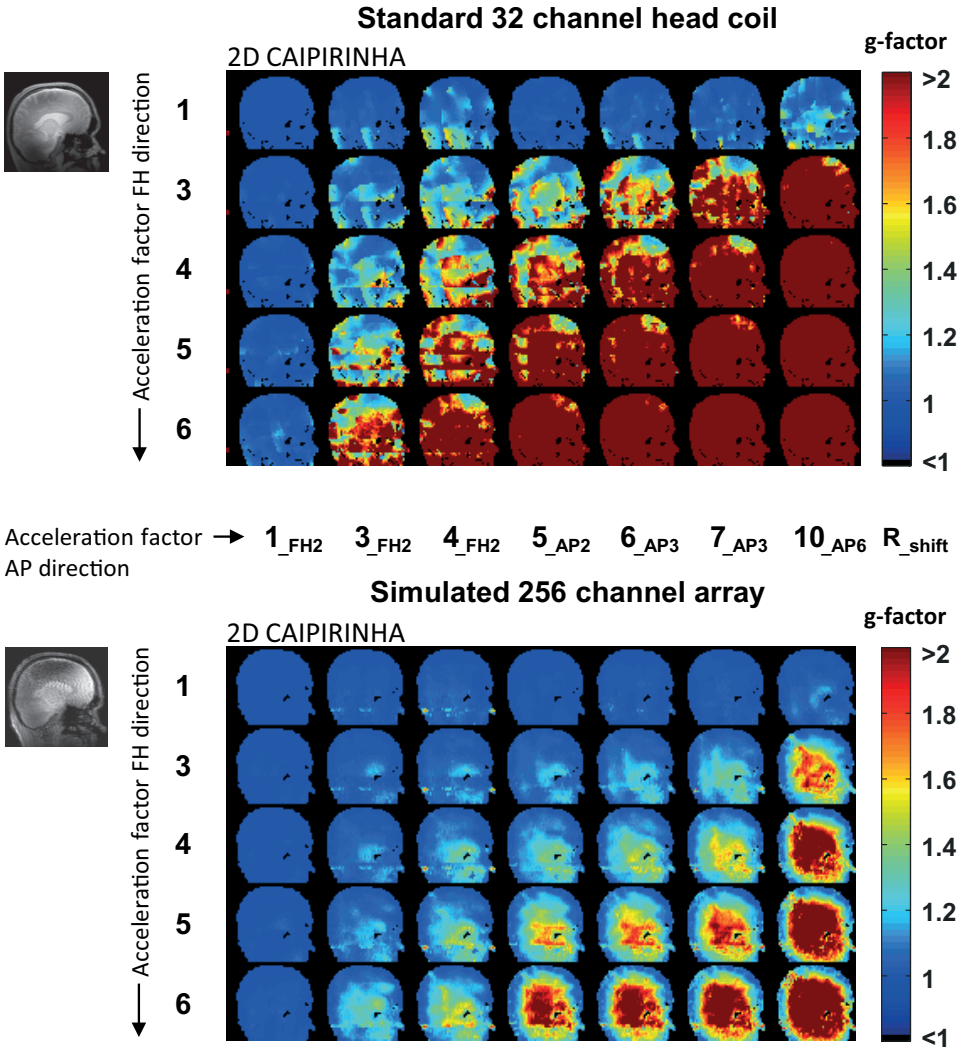


**Figure 13: g-factor maps for the standard head coil (top) and the simulated 256 channel receive array (bottom), using the undersampling patterns of 2D CAIPIRINHA. The figure layout is equal to the layout of Figure 12, allowing comparison between both figures and their undersampling methods. Specific patterns can be referred to by $R^{total}$ (undersampling method $R^{FH}$ x $R^{AP}_{\_CAIPIshift}$). The maximum achievable acceleration, for g-factors smaller than 2, is for standard 32 channel head coil 12 (CAIPIRINHA 4x3$_{_FH2}$), and for the simulated 256 channel receive array 28 (CAIPIRINHA 4x7$_{_AP3}$). Note that this is higher than the maximum acceleration factors achieved with SENSE of respectively 9 and 24.**

## Discussion

The aim of this study was to assess the potential gain in acceleration performance of a 256 channel high density receive coil array at 7T, combined with the parallel imaging methods 2D SENSE and 2D CAIPIRINHA for 3D datasets. To realize this, measurements were performed with two 16 channel gapped receive arrays consisting of small coil elements, which were used as basic building blocks to simulate a 256 channel head coil. The g-factor maps indicate that the 256 channel head coil array can deliver more than a 2-fold improvement in acceleration performance, as compared to the standard 32 channel head coil. In addition, for both the standard head coil and the simulated 256 channel array, a 2D CAIPIRINHA sampling pattern can significantly improve the SNR or acceleration performance. Overall, a remarkable maximum acceleration factor of 28 is estimated. This suggests that whole brain high density receive arrays combined with fast parallel imaging acquisition methods show great potential for fMRI with high spatial and high temporal resolution.



### SNR

The SNR of the simulated 256 channel array is high, especially at the periphery of the brain, as can be observed in the SNR maps. Though, in these SNR maps not all noise correlation terms could be included, because the reference scans were obtained consecutively. In the periphery of the brain, the average gain in SNR of the simulated 256 channel array is a factor of 1.5, and goes up to a factor of 2.7 in tissue close to the coil elements. Up to a certain depth, measured from the coil elements, smaller sized coil elements gain SNR, which can also be seen in the SNR profiles. However, for very small coils, this substantial gain will be restricted to few centimeters away from the coil. In this study, the worst-case midpoint region of the brain shows an SNR reduction by a factor of 0.8 on average (ranging from 0.7 to 0.9), whereas the SNR of a larger central region of the brain is comparable between setups with a factor of 1.0 on average (ranging from 0.7 to 1.6). The SNR in the worst-case midpoint region is lower as compared to the standard 32 channel head coil, raising questions about the optimum 7T head coil configuration, coil element size and the number of channels to achieve maximum intrinsic SNR. The noise figure of the simulated 256 channel coil is expected to increase by 20%, due to the smaller element size [12], which would be evident especially in the center of the brain. The relatively good SNR values in the larger central region of the brain might be explained by the fact that the 256 channel surface coil elements are closer to the head than the 32 channel elements. Coil proximity improves the coil loading, enhancing the SNR [42]. If the array was designed for maximum intrinsic SNR excluding acceleration, then our coil element size may be too small. However, the motivation of our study was to maximize acceleration performance while maintaining SNR.

### Noise correlation

To obtain optimal SNR, it is necessary to ensure that the noise from channel to channel is largely uncorrelated [43]. In this study, the noise correlation between individual coils is low, with average noise correlation coefficients of 0.027 and 0.054 for the 256 channel array and the 32 channel head coil respectively.

### Acceleration performance

The acceleration performance was assessed based on the g-factor maps. For both 2D SENSE and 2D CAIPIRINHA acquisition schemes, acceleration factors for the simulated 256 channel array are 2-fold higher than the standard 32 channel head coil, considering a maximum acceptable g-factor of 2. An estimated peak acceleration factor of 28 was found when using 2D CAIPIRINHA. The use of 2D CAIPIRINHA is desirable over 2D SENSE, because it has lower g-factors, due to more optimal distribution of aliasing patterns. For the simulated 256 channel array, especially at the periphery of the brain, the g-factor is well below 2. This is in accordance with the high receive sensitivity at that location. Even at very high accelerations such as 42, the g-factor at the edge of the brain is still below 2 for the 256 channel coil. For studies that are only interested in the periphery of the brain, as is the case for some cortical fMRI studies, this would indicate that potentially even higher accelerations than a factor of 28 are possible.

### Comparison with state-of-the-art high density receive arrays

Previous work at 3T of Wiggins et al. shows that a 96 channel receive array for the head improves imaging performance, in comparison to an identically-sized 32-channel coil [10]. When following this direction at 7T, smaller coil elements can be used without contributing substantially to the noise. Below, a comparison of the receive performance of the simulated 256 channel array to the 96 channel array is given in terms of SNR, average noise correlation, and acceleration performance. For the simulated 256 channel array, an average SNR increase of a factor 1.5 is seen in the periphery of the brain as compared to the 32 channel coil. For 96 channel array at 3T, an SNR increase of a factor of 1.4 was reported, as compared to an equally sized 32 channel coil. The average off-diagonal noise correlation coefficient is low for the 256 channel coil, with a value of 0.027. For the 96 channel coil this is 0.148. The maximum SENSE acceleration performance was evaluated by comparing the g-factor maps with a g-factor of less than 2. A maximum acceleration factor of 24 (SENSE 4x6) can be achieved for the simulated 256 channel array, as measured in a volunteer. For the 96 channel coil a maximum acceleration factor between 9 (SENSE 3x3) and 16 (SENSE 4x4) was reported, as measured in a brain phantom.

A possible explanation for the large increase in acceleration factor for the 256 channel array (as compared to the 32 channel coil and also as compared to previous work) could be the coil array design. First, a high number of coil elements was used here, enabling the acquisition

of more data with receivers that have different spatial sensitivities, which can be translated to higher attainable acceleration factors. Second, no overlap between coil elements was used in the transverse direction. The gap between elements not only benefits SENSE performance [35], but also facilitates flexibility of the coil array, hence assuring a tighter fit to the head. Third, using pre-amplifier decoupling and cable management of the 2x16 receive channels, RF coupling between adjacent coil elements was aimed to be low. The cables of the 2x16 channel receive array are guided in sets of 4 channels per cable trap (Figure 8), reducing the cable coupling burden. A future step in cable management is the implementation of a digital receive pipeline, which would allow data from multiple receive channels through fiber optic cables, drastically reducing the amount of RF cables further.



## Methodological considerations

From a methodological point of view, it must be noted that the reference scan of the simulated 256 channel coil was acquired consecutively, excluding most noise correlation terms in the g-factor calculations. Nevertheless, coil coupling is expected to be highest between neighboring coils, and this was for the most part taken into account in this study by partially filling the noise correlation matrix (diagonally) with the noise coupling measured from the 2x16 channel sets (Figure 11a). Still, coupling between directly neighboring coils from adjacent measurement sets were excluded from the simulation. Additionally, noise correlation may even increase if incorrect cable management is provided. The coils from different measurement sets are at further distance physically, so it should be possible to maintain negligible noise coupling between these elements with correct cable management. For example when digital receivers are put in (or close to) the coil before the cables get in close proximity. Considering the impact of noise correlation on image SNR in general, one needs to consider true coil sensitivities including noise correlations. However, as described by others, in the general case there is almost no difference in SNR from omitting the coil-noise matrix from the reconstruction algorithm for coils that are well decoupled [44].
The transmit power drive scale did not change more than 5% between receive setups, which excludes a large bias in the intrinsic SNR comparison caused by changes in $B_1$ field. However, once a full 256 channel array would be in place, the $B_1$ level of transmit coil can be effected significantly. The sum of all small potential couplings of the transmit coil to copper, cables and cable traps of a full receiver setup may require more RF power for the same $B_1$ field. To mitigate this, stronger RF amplifiers might be necessary.

The maximum acceleration factor in this study was assessed by evaluating the g-factor maps. In practice, the acceleration factor and SNR are not solely dependent on the g-factor. When the k-space signal is undersampled during acquisition, there is also an inherent SNR loss ($\sqrt{R}$) from acquiring fewer samples. The image SNR ($SNR_0$) decreases with the g-factor and the acceleration factor ($g\cdot\sqrt{R}$). However, the time-course SNR (tSNR), which is important for fMRI

applications, decreases less rapidly [45]. Depending on the application and imaging settings, an optimal acceleration factor can be chosen. Generally, g-factor maps are a good indication of the potential acceleration performance of a coil.

### Choices for coil element design and array configuration

In this study a number of design choices were made including: coil element size, the number of coil elements and the amount of overlap between elements. All choices were made to target high acceleration factors. The large number of small coil elements, used in this study, made it possible to achieve a high acceleration factor of 28. Despite the achieved high acceleration factors, it can be questioned what the most optimal design and array configuration is for a field strength of 7T. Also note that an optimal coil design to achieve maximum acceleration with parallel imaging may be different than the optimal coil design for maximum intrinsic SNR without acceleration [40]. There is still room for improvement in the design and shape of individual coil elements, as these were not optimized in length versus diameter. Furthermore, overlapped designs [9,10] could have a different optimal number and size of coil elements at 7T as compared to SENSE specific gapped designs [35,36]. More advanced coil arrangements and designs, for example using a combination of different coil sizes and overlap, may outperform our proposed setup in the future. This could lead to other, potentially even higher acceleration factors, as demonstrated with single echo acquisition techniques [19].

### Future and technical considerations of 256 channels

From a practical point of view, a number of engineering challenges may emerge with respect to the construction of a 256 channel coil. First, small coil elements are required, so they can cover the head in a quantity of 256. In this study, small 1.5 x 2 $cm^2$ sized elements were used which can be fitted tightly over the head.

Second, the receive pipeline connecting the 256 channel array should also be physically able to connect and subsequently preprocess the signal from all these channels. A digital receive pipeline seems essential, because it enables information from multiple receive channels to be transported through one fiber optic cable. The design goal is to convert the signal from analog to digital as early in the receive pipeline as possible, minimizing the amount of RF cables, their length and thereby cable coupling. Preamplifier boards can be designed to be small enough to be stacked tightly in the scanner bore behind the head coil, reducing the excessive use of cables.

Third, a large number of independent receiver channels can also have practical limitations in terms of handling and processing a substantially larger amount of independent data streams. In particular, reconstruction speed can decrease considerably. At the same time, however, digital receive and computer hardware are evolving to be able to handle these kinds of data flow. Furthermore, data size reduction techniques, such as array compression [46] have proven to be very effective in reducing data size even before image reconstruction.

## Conclusion

Overall, the results showed superior receive performance of the simulated 256 channel receive array on acceleration performance. This holds not only in comparison to the standard 32 channel head coil, but also as compared to other reported high density receivers in literature. The results in this study suggest that the benefits achieved in spatial and temporal fMRI resolution by using the high-density 32 channel configuration, can be extended to 256 channels with full head coverage. In conclusion, the simulated 256 channel head coil shows great acceleration possibilities. Together with 2D CAIPIRINHA, a peak acceleration factor of 28 can be achieved, revealing high potential for whole brain high density receive arrays combined with fast parallel imaging acquisition methods to measure brain function at high spatial and high temporal detail.



## References


1. Roemer PB, Edelstein WA, Hayes CE, Souza SP, Mueller OM. The NMR phased array. Magn Reson Med 1990;16(2):192-225.
2. Wald LL, Carvajal L, Moyher SE, Nelson SJ, Grant PE, Barkovich AJ, Vigneron DB. Phased array detectors and an automated intensity-correction algorithm for high-resolution MR imaging of the human brain. Magn Reson Med 1995;34(3):433-439.
3. Chu YH, Hsu YC, Keil B, Kuo WJ, Lin FH. A 32-Channel Head Coil Array with Circularly Symmetric Geometry for Accelerated Human Brain Imaging. PLoS One 2016;11(2):e0149446.
4. Cohen-Adad J, Mareyam A, Keil B, Polimeni JR, Wald LL. 32-channel RF coil optimized for brain and cervical spinal cord at 3 T. Magn Reson Med 2011;66(4):1198-1208.
5. Keil B, Alagappan V, Mareyam A, McNab JA, Fujimoto K, Tountcheva V, Triantafyllou C, Dilks DD, Kanwisher N, Lin W, Grant PE, Wald LL. Size-optimized 32-channel brain arrays for 3 T pediatric imaging. Magn Reson Med 2011;66(6):1777-1787.
6. Wiggins GC, Triantafyllou C, Potthast A, Reykowski A, Nittka M, Wald LL. 32-channel 3 Tesla receive-only phased-array head coil with soccer-ball element geometry. Magn Reson Med 2006;56(1):216-223.
7. Cline HE, Sodikson DK, Niendorf T, Giaquinto R. 32-Channel Head Coil Array for Highly Accelerated Parallel Imaging Applications. Proceedings of the 12th Annual Meeting of the ISMRM, Kyoto, Japan; 2004; Kyoto, Japan. p 2387.
8. Moeller S, Van de Moortele P-F, Adriany G, Snyder CJ, Andersen PM, Strupp JP, Vaughan JT, Ugurbil K. Parallel Imaging performance for densely spaced coils in phase arrays at ultra high field strength. Proceedings of the 12th Annual Meeting of the ISMRM, Kyoto, Japan; 2004. p 2388.
9. Keil B, Blau JN, Biber S, Hoecht P, Tountcheva V, Setsompop K, Triantafyllou C, Wald LL. A 64-channel 3T array coil for accelerated brain MRI. Magn Reson Med 2013;70(1):248-258.
10. Wiggins GC, Polimeni JR, Potthast A, Schmitt M, Alagappan V, Wald LL. 96-Channel receive-only head coil for 3 Tesla: design optimization and evaluation. Magn Reson Med 2009;62(3):754-762.
11. Feinberg DA, Vu AT, Beckett A. Pushing the limits of ultra-high resolution human brain imaging with SMS-EPI demonstrated for columnar level fMRI. Neuroimage 2018;164:155-163.
12. Petridou N, Italiaander M, van de Bank BL, Siero JC, Luijten PR, Klomp DW. Pushing the limits of high-resolution functional MRI using a simple high-density multi-element coil design. NMR Biomed 2013;26(1):65-73.
13. Wiesinger F, De Zanche N, Pruessmann KP. Approaching Ultimate SNR with Finite Coil Arrays. Proceedings of the 13th Annual Meeting of the ISMRM, Miami, USA; 2005; Miami, Florida, USA. p 672.

14. Fujita H. New horizons in MR technology: RF coil designs and trends. Magn Reson Med Sci 2007;6(1):29-42.
15. Wright SM, Wald LL. Theory and application of array coils in MR spectroscopy. NMR Biomed 1997;10(8):394-410.
16. Sodickson DK, Lee RF, Giaquinto RO, Collins CM, McKenzie CA, Ohliger MA, Grant AK, Willig-Onwuachi JD, Yeh EN, Kressel HY. Depth Penetration of RF Coil Arrays for Sequential and Parallel MR Imaging. Proceedings of the 11th Annual Meeting of the ISMRM, Toronto, Canada; 2003; Toronto, Ontario, Canada. p 469.
17. Wiggins GC, Potthast A, Triantafyllou C, Lin F, Benner T, Wiggins CJ, Wald L. A 96-channel MRI System with 23- and 90-channel Phase Array Head Coils at 1.5 Tesla. Proceedings of the 13th Annual Meeting of the ISMRM, Miami, USA; 2005; Miami, Florida, USA. p 671.
18. Keil B, Wald LL. Massively parallel MRI detector arrays. J Magn Reson 2013;229:75-89.
19. McDougall MP, Wright SM. 64-channel array coil for single echo acquisition magnetic resonance imaging. Magn Reson Med 2005;54(2):386-392.
20. Hardy CJ, Giaquinto RO, Piel JE, Rohling KW, Marinelli L, Blezek DJ, Fiveland EW, Darrow RD, Foo TK. 128-channel body MRI with a flexible high-density receiver-coil array. J Magn Reson Imaging 2008;28(5):1219-1225.
21. Schmitt M, Potthast A, Sosnovik DE, Polimeni JR, Wiggins GC, Triantafyllou C, Wald LL. A 128-channel receive-only cardiac coil for highly accelerated cardiac MRI at 3 Tesla. Magn Reson Med 2008;59(6):1431-1439.
22. Vaidya MV, Sodickson DK, Lattanzi R. Approaching Ultimate Intrinsic SNR in a Uniform Spherical Sample with Finite Arrays of Loop Coils. Concepts Magn Reson Part B Magn Reson Eng 2014;44(3):53-65.
23. Wiesinger F, Boesiger P, Pruessmann KP. Electrodynamics and ultimate SNR in parallel MR imaging. Magn Reson Med 2004;52(2):376-390.
24. Barth M, Breuer F, Koopmans PJ, Norris DG, Poser BA. Simultaneous multislice (SMS) imaging techniques. Magn Reson Med 2016;75(1):63-81.
25. Feinberg DA, Setsompop K. Ultra-fast MRI of the human brain with simultaneous multi-slice imaging. J Magn Reson 2013;229:90-100.
26. Setsompop K, Feinberg DA, Polimeni JR. Rapid brain MRI acquisition techniques at ultra-high fields. NMR Biomed 2016;29(9):1198-1221.
27. Pruessmann KP, Weiger M, Scheidegger MB, Boesiger P. SENSE: sensitivity encoding for fast MRI. Magn Reson Med 1999;42(5):952-962.
28. Griswold MA, Jakob PM, Heidemann RM, Nittka M, Jellus V, Wang J, Kiefer B, Haase A. Generalized autocalibrating partially parallel acquisitions (GRAPPA). Magn Reson Med 2002;47(6):1202-1210.
29. Breuer FA, Blaimer M, Heidemann RM, Mueller MF, Griswold MA, Jakob PM. Controlled aliasing in parallel imaging results in higher acceleration (CAIPIRINHA) for multi-slice imaging. Magn Reson Med 2005;53(3):684-691.
30. Breuer FA, Blaimer M, Mueller MF, Seiberlich N, Heidemann RM, Griswold MA, Jakob PM. Controlled aliasing in volumetric parallel imaging (2D CAIPIRINHA). Magn Reson Med 2006;55(3):549-556.
31. Collins CM, Yang QX, Wang JH, Zhang X, Liu H, Michaeli S, Zhu XH, Adriany G, Vaughan JT, Anderson P, Merkle H, Ugurbil K, Smith MB, Chen W. Different excitation and reception distributions with a single-loop transmit-receive surface coil near a head-sized spherical phantom at 300 MHz. Magn Reson Med 2002;47(5):1026-1028.
32. Wang J, Yang QX, Zhang X, Collins CM, Smith MB, Zhu XH, Adriany G, Ugurbil K, Chen W. Polarization of the RF field in a human head at high field: a study with a quadrature surface coil at 7.0 T. Magn Reson Med 2002;48(2):362-369.
33. Kumar A, Edelstein WA, Bottomley PA. Noise figure limits for circular loop MR coils. Magn Reson Med 2009;61(5):1201-1209.
34. Gosselink WJM, Anzellotti A, Mens G, Boutelje M, Voermans B, Hoogduin H, Luijten PR, Possanzini C, Klomp DWJ. Converting digital MRI receivers built for 1.5T into 7T receivers using Surface Acoustic Wave filters. Proceedings of the 23rd Annual Meeting of the ISMRM,

Toronto, Canada; 2015; Toronto, Ontario, Canada. p 1823.
35. de Zwart JA, Ledden PJ, Kellman P, van Gelderen P, Duyn JH. Design of a SENSE-optimized high-sensitivity MRI receive coil for brain imaging. Magn Reson Med 2002;47(6):1218-1227.
36. Weiger M, Pruessmann KP, Leussler C, Roschmann P, Boesiger P. Specific coil design for SENSE: a six-element cardiac array. Magn Reson Med 2001;45(3):495-504.
37. Batson MA, Petridou N, Klomp DW, Frens MA, Neggers SF. Single session imaging of cerebellum at 7 Tesla: obtaining structure and function of multiple motor subsystems in individual subjects. PLoS One 2015;10(8):e0134933.
38. Fracasso A, Luijten PR, Dumoulin SO, Petridou N. Laminar imaging of positive and negative BOLD in human visual cortex at 7T. Neuroimage 2018;164:100-111.
39. Ledden PJ, Mareyam A, Wang S, van Gelderen P, Duyn J. 32 Channel Receive-Only SENSE Array for Brain Imaging at 7T. Proceedings of the 15th Annual Meeting of the ISMRM, Berlin, Germany 2007 p 242 2007.
40. Ohliger MA, Sodickson DK. An introduction to coil array design for parallel MRI. NMR Biomed 2006;19(3):300-315.
41. Cox RW. AFNI: software for analysis and visualization of functional magnetic resonance neuroimages. Comput Biomed Res 1996;29(3):162-173.
42. Corea JR, Flynn AM, Lechene B, Scott G, Reed GD, Shin PJ, Lustig M, Arias AC. Screen-printed flexible MRI receive coils. Nat Commun 2016;7:10839.
43. Brown RW, Cheng Y-CN, Haacke EM, Thompson MR, Venkatesan R. Chapter 27: MRI Coils and Magnets. Book of Magnetic Resonance Imaging: Physical Principles and Sequence Design, Second Edition John Wiley & Sons Ltd; 2014. p 823-857.
44. Bernstein MA, King KF, Zhou XJ. Chapter 13: Common Image Reconstruction Techniques. Handbook of MRI Pulse Sequences. Burlington: Academic Press; 2004. p 530.
45. Triantafyllou C, Polimeni JR, Wald LL. Physiological noise and signal-to-noise ratio in fMRI with multi-channel array coils. Neuroimage 2011;55(2):597-606.
46. Buehrer M, Pruessmann KP, Boesiger P, Kozerke S. Array compression for MRI with large coil arrays. Magn Reson Med 2007;57(6):1131-1139.

# Chapter 4

## Ultrasonic gradients in magnetic resonance imaging

Debra S. Rivera,
Arjan D. Hendriks,
Tijl A. van der Velden,
Jeroen C. Siero,
Dennis W.J. Klomp

**Patent details:** Application No./Patent No.: 17020058.8 – 1568 European Patent Office. Method and apparatus for ultrasonic gradients in magnetic resonance imaging. Date of filing: 17-02-2017.

## Abstract

**Patent summary:** The herein described invention relates to a gradient system and method that allows for a spatial encoding gradient driven at high (> 10 kHz) or ultrasonic (≥ 20 kHz) frequencies in order to achieve fast slew-rate high-strength spatial encoding gradients without generating vibration in the auditory range and without inducing peripheral nerve stimulation.

Rise time is proportional to inductance, therefore gradient coils that minimize inductance per generated magnetic-flux density, allow for faster switching rates. Such a system can be implemented, for example as an insert gradient coil (in 1, 2, or 3 axis) to augment the in-bore gradient system in close proximity to the head or imaging target. Such a system may exclude counter-windings, creating a minimum inductance for a given magnetic flux density. The use of spatial encoding gradients at increased drive frequency reduces the moment of inertia and thus magneto-mechanical vibrations, and therefore allows for more light-weight construction of coils and elimination of counter-winding for self-shielding coils.

An embodiment of the presented invention is the use of high-frequency gradients in combination with 3 phase encoding directions and receive coil spatial sensitivity profiles, to enable parallel imaging with acceleration in 3 dimensions.

Application No./Patent No.: 17020058.8 - 1568
Date of filing: 17-02-2017

**Method and apparatus for ultrasonic gradients in magnetic resonance imaging**

The present invention relates to magnetic resonance imaging, more specifically the spatial encoding gradients of the magnetic resonance system.

Magnetic resonance imaging (MRI) is performed on an MRI scanner. An MRI scanner typically consists of a large static magnetic field $B_0$, a set of radio frequency coils or antennas for generating an alternating magnetic field $B_1$ and collecting the MR signal, and a set of gradient coils to allow spatial encoding on the $B_0$ field which is required for tomographic imaging.

Spatial encoding of the MR signals is achieved by fast switching of three orthogonal magnetic field gradients (X, Y, Z) located in the scanner bore that surrounds the body, often combined with encoding caused by coil sensitivity profiles. Current state of the art, involves driving spatial-encoding gradients in the kHz range (0-10 kHz) as specified in US 5610521A. Given that the gradients are driven in the auditory range (<<20 kHz), considerable efforts have gone towards methods for reducing the noise caused by the Lorenz forces induced in and by the switching gradients. One such method, disclosed in DE 102004042100 A1, incorporates vibration dampening material in order to reduce the noise. Additional methods incorporate counter-wound turns, concentric to and in series with the gradient coil windings, tightly coupled to the same rigid mass, creating a self-shielding structure in which the magneto-motive forces are anti-phase and therefore cancel, for either primary gradients as in DE 102004042100 A1 or for an insert gradient, such as US 5235279 A.



To boost the MRI spatiotemporal resolution, the gradient system needs to be driven faster and stronger, in other words with higher gradient slew-rates (T per m per s) and higher gradient strengths (mT per m). The other means of spatial encoding by coil sensitivity profiles is limited by enhanced g-factors (noise amplification due to spatially correlating sensitivity profiles). At present, the gradient performance is mainly limited by uncomfortable peripheral nerve stimulations (PNS) induced by too fast switching of a strong magnetic field gradient. Switching of the gradients induces electrical fields and currents in conducting tissue, such as muscles and nerves, and may result in nerve depolarization and ultimately nerve stimulation. A viable strategy for faster and stronger gradient coil performances while preventing nerve stimulation is I) to reduce the extent of the gradient field and thus the associated electric field and II) to reduce the switch times below the PNS threshold (IEC guidelines).

For improved spatiotemporal resolution of MRI it is necessary to increase spatial encoding gradient strength and switching speed, which are currently limited primarily by the need to

minimize peripheral nerve stimulation. Spatial gradient systems generated vibration in the auditory range, requiring rigid housing for dampening the vibration and minimizing the risk of hearing damage. The herein described invention relates to a gradient system and method that allows for a spatial encoding gradient that can be driven at ultrasonic frequencies (≥ 20 kHz) as in claim 1, or high frequencies (> 10 kHz) as in claim 2, to provide high resolution MRI, and thereby overcome the aforementioned limitations of conventional gradient systems. Inductance is proportional to the ramp time, therefore gradient coils that minimize inductance per generated magnetic field have shorter rise times and thus allow for faster switching rates. The present invention provides the following advantages over the state-of-the-art: vibrations occurring from fast-switching gradients are outside of the range of human hearing as in claim 1, voltage requirements of the gradient signal generators are diminished due to less copper windings as in claim 3, the moment of inertia caused by the short duration of the Lorentz forces on the gradient system are reduced thereby allowing for a less robust and lighter weight housing as in claim 6, peripheral nerve stimulation is no longer a limiting factor (occurs at > 100 µs) as in claim 7, and such a system, capable of fast-switching strong gradients, results in a greatly increased MRI temporal resolution, particularly when combined with high density receiver coil arrays (as in claim 8) and existing state-of-the art scanning techniques (as in claim 9) and high power gradient amplifiers.

Herein after, further details of the present invention will be given in the context of specific embodiments, though are not limited by the scope of the presented embodiments.

An embodiment of the invention is an insert gradient coil (in 1, 2, or 3 axis) to augment the in-bore gradient system, in close proximity to the head or imaging target as in claim 4, and may exclude counter-windings, and thus create a minimum inductance for a given magnetic flux density. A further embodiment of the invention described in claim 1, wherein the windings of the high frequency (> 10 kHz) gradient coil are made of hollow tubings to allow fluid-based cooling as in claim 5.

In order to also maximize spatial resolution in the presence of the fast-switching gradients, an additional direction of spatial encoding can be added with high density RF coil receiver arrays. Phase encoding is done on a larger time-scale than readout (aka frequency) encoding, and therefore more amenable to acceleration. So far, receiver arrays have been used to accelerate in either 1 or 2 --and in the rare-case 3-- phase encoding directions, but for MRI never in the readout direction. Moving from 1 dimension to 2 dimensions already boosted acceleration at preserved g-factor. When increasing to 3 dimensions, acceleration can be increased even further without sacrificing g-factor. The reason for accelerating in 3 directions is that the number of useful samples that can be obtained during one lobe of the ultra-fast EPI readout is limited, and may be less than required for high spatial resolution. Here we propose to

use phase encoding in 3 dimensions in addition to the readout in one dimension to further enhance spatial resolution.

For clarity we provide an example embodiment of the presented invention of an ultrasonic (20 kHz) z-direction gradient head insert, such as shown in Figure 15, used in combination with the x-, y-, and z-gradients of the MRI scanner for brain imaging.

For a 3D MRI with a spatial resolution of 2 mm x 2 mm x 1 mm (x, y, z) with a field of view of 15 cm x 15 cm x 20 cm using a z-gradient of 160 mT/m and slewrate of 13000 T/m/s, a suitable bandwidth is 15 cm x 166 mT/m x 42.5 MHz/T = 1 MHz. A 20 kHz z-gradient provides 25 microsecond lobes, thus 25 data points per lobe (1 MHz x 25 µs). Current state of the art gradient amplifiers can provide 2 kV and 1 kA, hence can drive a copper-wound head gradient coil 1 as seen in Figure 14. For a typical $T_2$* contrast a 60 ms acquisition window can be used; this provides 240 z-lobes with a 20 kHz z-gradient. Adding a constant z-gradient during the readout period facilitates additional phase encoding in this z-dimension. Accelerating 4 fold in z-direction using an array of coils that provide different sensitivity profiles along z then requires only 2 phase encode steps in the z direction to end up in 2 x 4 x 25 = 200 data points in z-direction. Adding a blipped or constant phase encoding in the y-direction could facilitate 15 lines and using coil sensitivity profile differences in the y-direction may extend 5-fold into a y-direction resolution of 2 mm. Finally, using a slow low power EPI train in x-direction can generate 15 or even 8 lines if half k-space scanning is used that can translate in a spatial resolution of 2 mm in x-direction as well. A simplified representation of a pulse sequence of this example is shown in Figure 16 and the corresponding acquired k-space (excluding coil sensitivity acceleration) in Figure 17.

Additional embodiments of the present invention incorporate high-frequency or ultrasonic switching gradients in more than one direction, such that readout trajectories through k-space are not limited to those presented herein.

**Claims**

1. A method of operating a magnetic resonance imaging (MRI) system having a gradient coil, characterized by driving the MRI field gradients above the human auditory range ( = or > 20 kHz).

2. The use of frequencies above 10 kHz for driving MRI spatial encoding gradients.

3. A magnetic field gradient coil system comprising of coils that provide at least one axis of spatial encoding in which one or more of the coils are designed with minimal inductance such that the coil(s) can be driven at high frequency (> 10 kHz) and due to the minimal inductance require limited voltage.

4. A gradient system as in claim 3 in which one or more axis of spatial encoding is implemented all or in part as a gradient insert coil.

5. A magnetic field gradient coil system comprising of coils that provide at least one axis of spatial encoding in which one or more of the coils are driven at high frequency (> 10 kHz) and are made of hollow conductors to facilitate efficient cooling.

6. A magnetic field gradient coil system comprising of coils that provide at least one axis of spatial encoding characterized in that the intended use of the coils is for high frequency switching gradients (= or > 10 kHz) and therefore can be made lightweight due to the reduced moment of inertia associated with shortened duration of Lorenz forces as the drive frequency is increased.

7. A method of operating spatial encoding gradients for MRI characterized by the use of high frequency switching gradients in order to prevent peripheral nerve stimulation.

8. The use of an array of RF receivers to extend the spatial encoding of high frequency (>10 kHz) switching of gradient fields MRI readout of EPI or any trajectory through k-space of any dimensions.

9. A method as in claim 8 in which g-factors get minimized and parallel imaging encoding schemes (e.g. CAIPIRINHA) become more effective from 3D acceleration.

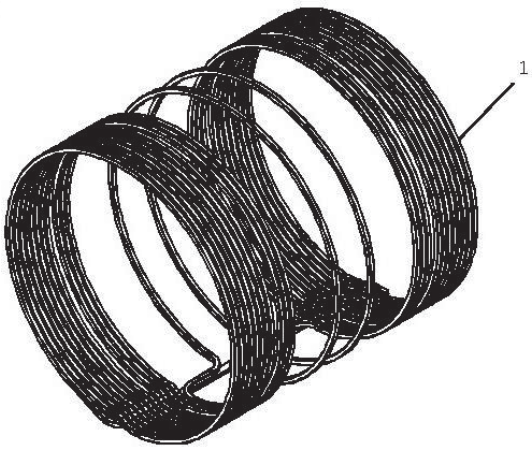


Figure 14a

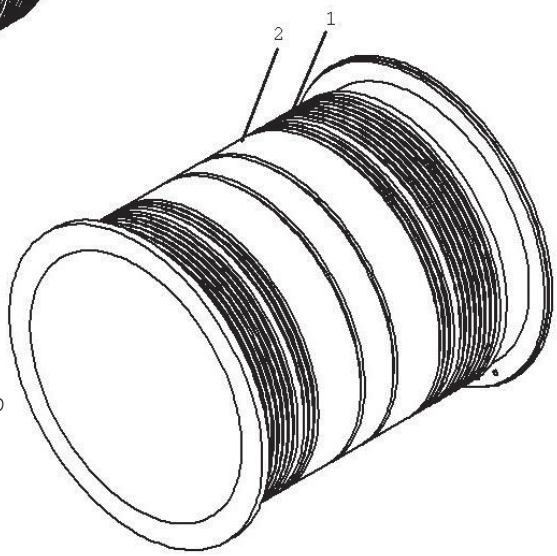


Figure 14b

**Figure 14: Copper windings (1) as an embodiment of the presented invention. The embodiment provides one-axis of spatial encoding above 10 kHz, in which coil inductance is minimized by the lack of a return section or self-shielding counter-wound section. The copper windings (1) are shown in Figure 14a. In Figure 14b the copper windings are mounted on a former (2) a structure that supports the gradient windings. It is lightweight in accordance with claim 6.**

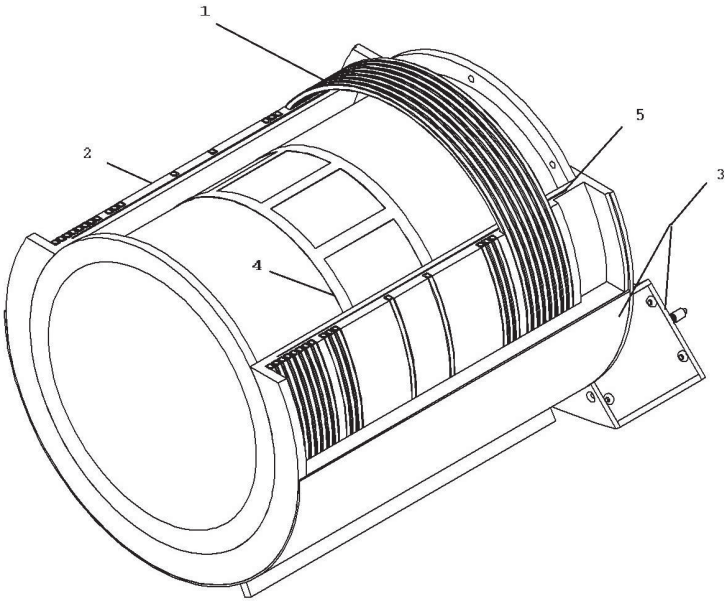


**Figure 15: An embodiment of the invention as described in claim 4. A single axis of spatial encoding is implemented as an insert high-frequency gradient, with the high-frequency gradient winding (1) mounted on a lightweight structure (2) that is contained within a housing (3) which can be mounted on an MRI scanner bed. The housing (3) also contains an RF coil (4) and an RF shield (5) embedded in the gradient coil structure (2).**

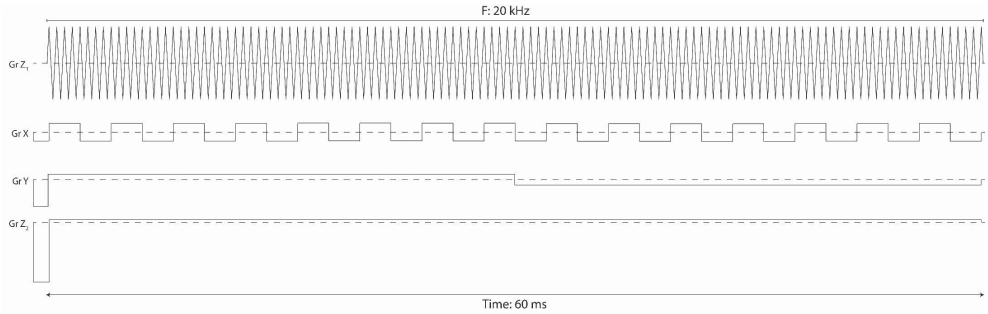


**Figure 16: A simplified representation of the gradient waveforms of an accelerated 3D single shot EPI trajectory. Gradient $Z_1$ is performed at an ultrasonic frequency. Gradient X and Y are performed at frequencies in the acoustic range, but with a low amplitude. Gradient $Z_2$ ensures an additional phase encoding in the readout direction.**



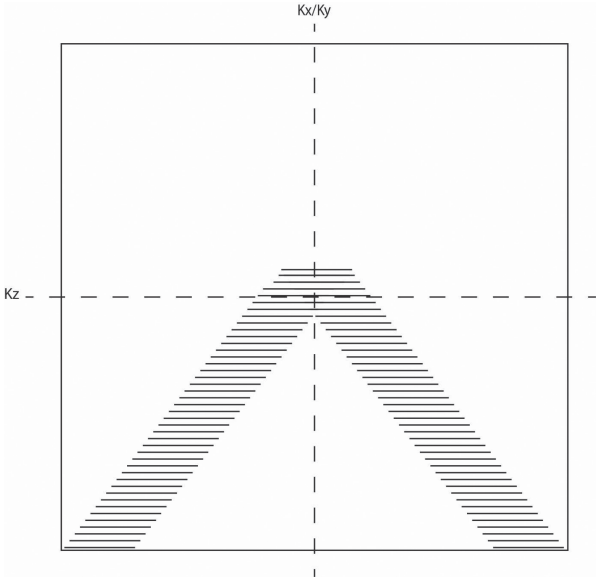


**Figure 17: A 2D simplification of the k-space trajectory of the sequence shown in Figure 16. Each line represents the acquisition during a single lobe of the magnetic gradient field switching at a frequency of 20 kHz.**

# Chapter 5

## Maximizing sensitivity for fast GABA edited spectroscopy in the visual cortex at 7T

Arjan D. Hendriks,
Alessio Fracasso,
Catalina S. Arteaga de Castro,
Mark W.J.M. Gosselink,
Peter R. Luijten,
Natalia Petridou,
Dennis W.J. Klomp

**Based on publication:** Hendriks A.D., Fracasso A., Arteaga de Castro C.S., et al. Maximizing sensitivity for fast GABA edited spectroscopy in the visual cortex at 7T. NMR in Biomedicine. 2018;31:e3890. DOI: 10.1002/nbm.3890

## Abstract

**Introduction:** The combination of functional MRI (fMRI) and MRS is a promising approach to relate BOLD imaging to neuronal metabolism, especially at high field strength. However, typical scan times for GABA edited spectroscopy are of the order of 6-30 min, which is long compared with functional changes observed with fMRI. The aim of this study is to reduce scan time and increase GABA sensitivity for edited spectroscopy in the human visual cortex, by enlarging the volume of activated tissue in the primary visual cortex.

**Methods:** A dedicated setup at 7T for combined fMRI and GABA MRS is developed. This setup consists of a half volume multi-transmit coil with a large screen for visual cortex activation, two high density receive arrays and an optimized single-voxel MEGA-sLASER sequence with macromolecular suppression for signal acquisition. The coil setup performance as well as the GABA measurement speed, SNR, and stability were evaluated.

**Results:** A 2.2-fold gain of the average SNR for GABA detection was obtained, as compared with a conventional 7T setup. This was achieved by increasing the viewing angle of the participant with respect to the visual stimulus, thereby activating almost the entire primary visual cortex, allowing larger spectroscopy measurement volumes and resulting in an improved GABA SNR. Fewer than 16 signal averages, lasting 1 min 23 s in total, were needed for the GABA fit method to become stable, as demonstrated in three participants. The stability of the measurement setup was sufficient to detect GABA with an accuracy of 5%, as determined with a GABA phantom. In vivo, larger variations in GABA concentration are found: 14-25%.

**Conclusion:** Overall, the results bring functional GABA detections at a temporal resolution closer to the physiological time scale of BOLD cortex activation.

**Keywords:** fast edited spectroscopy, fMRS, half volume coil, MEGA-sLASER, visual cortex, γ-aminobutyric acid (GABA)

## Introduction

Blood-oxygenation-level-dependent (BOLD) functional MRI (fMRI) is the most widely used technique to measure brain function non-invasively in humans. BOLD measurements capture neuronal activity indirectly, via changes in blood flow, volume, and oxygenation [1,2]. These changes arise from local changes in neuronal activity and metabolism. The relationship between BOLD signals and excitatory neuro-metabolic processes has been studied extensively; however, the relationship between BOLD signals and inhibitory neuro-metabolic processes is less well understood [3-5]. One of the key inhibitory metabolites is γ-aminobutyric acid (GABA), which is the main inhibitory neurotransmitter of the brain and is believed to have a direct impact on BOLD contrast through regulation of neuronal firing rates [6-8]. In the human brain in vivo, the relationship between GABA and BOLD signals has been investigated in studies that combined fMRI and MRS [7,9-15].

Edited GABA spectroscopy is a commonly used technique to measure GABA levels [16]. With edited spectroscopy it is possible to separate the GABA signal from the signal of other metabolites. Faster non-edited, short echo time MRS techniques have been used for functional measurements of other metabolites as well, but often lack reliable quantification of GABA, because of contamination from overlapping resonances [17].

In order to further relate BOLD signal to GABA, it is desirable to measure GABA changes within the time scale of BOLD changes, meaning short scan times. Short scan times enable the measurement of rapid changes in GABA levels that are induced by specific cognitive tasks carried out by the participant inside the scanner [9,12,18]. Typical scan times for GABA edited spectroscopy reported in literature are of the order of 6-30 min [16], which is impermissibly long when compared with functional changes observed with fMRI. To further reduce scan time of GABA edited spectroscopy, the measurement method needs to be highly sensitive to GABA, allowing reduction of scan time per measurement.

At high magnetic field strengths, such as 7T or higher, the combination of BOLD fMRI and GABA MRS is particularly promising, because both BOLD contrast and MRS sensitivity are enhanced. This gain in sensitivity at high field can be traded for shorter measurement times. Nevertheless, even at high field, the sensitivity for functional GABA edited spectroscopy might not be enough. A seemingly simple solution to increase spectroscopic sensitivity is to increase the voxel size. However, when interested in specific regions of the brain, or regions that only contain tissue stimulated by a task, the voxel size must be limited by the corresponding physical brain shapes or by the maximal regional extent of stimulated tissue.

The aim of this study is to reduce scan time and increase GABA sensitivity for edited spectroscopy in the visual cortex. To realize this aim, a dedicated coil setup for a high field strength (7T) MRI

scanner was developed with a large projection screen. We focus on the visual cortex, because it is well characterized and it can be stimulated in a well-controlled manner. The developed setup consists of a multi-transmit head coil and high density receive arrays. The setup is developed for combined fMRI and GABA MRS at 7T in the visual cortex. The setup facilitates a clear visual view to a large screen, enabling a wide radial visual stimulus with a large visual angle. We expect that a stimulus with a large visual angle can activate a large cortical volume, which enables a large voxel size for spectroscopy, resulting in an enhanced GABA signal-to-noise ratio (SNR). GABA measurements are performed with a MEGA-sLASER sequence with macromolecular nulling. The sequence is modified to include frequency offset corrected inversion (FOCI) editing pulses, enhancing GABA detection and spatial localization [19]. This setup enabled us to measure individual GABA concentrations over a short period of time. The effectiveness of the approach to achieve short scan time is evaluated in two steps. First, the coil setup performance with visual stimulus is assessed, by mapping the extent of activation in primary visual cortex (V1) and by determining the corresponding increase in spectroscopy voxel size. Second, the achievable SNR, speed and stability of the GABA measurements are assessed by performing multiple repetitive GABA measurements in the same region.

## Design

### Coil setup and MRS sequence design, rationale

Three important aspects were taken into account for the design of the setup. First, the size of the projected visual stimulus, and corresponding visual angle of view of the subject, directly influences the size of visual cortex tissue volume that can be activated [20]. An increased visual angle of view of the participant, for example due to an increased screen size, leads to activation of a greater part of the visual cortex. When measuring GABA in this greater part of the visual cortex, the acquisition volume (size of the single voxel) can be increased, which in turn delivers a stronger GABA signal with an enhanced SNR. The gain in GABA SNR can be used to reduce the GABA spectroscopy acquisition time. As an additional advantage, by increasing the amount of stimulated tissue, the interference of signals arising from non-stimulated tissue can also be minimized. At high field, the elongated scanner bore together with closed transmit coil configurations decreases the maximum projection size for visual stimulation. Often, multiple mirrors and prisms have to be used, at the cost of reducing the participant's visual angle. Half volume multi-transmit coils that are specialized for the visual cortex do not have this drawback, and have recently been shown as a promising research tool for functional imaging [21]. The concept of an open half volume coil design [22-27] is used in this study to construct a setup that enables visual stimulation with a large visual angle.

Second, $B_1$ field uniformity over the acquisition volume is needed to reach the desired flip angle, which is especially important for GABA spectroscopy, in which editing pulses assume a

uniform $B_1$ field. Using multiple RF transmit coil elements in parallel can significantly improve $B_1$ field uniformity of high field MRI [28]. Therefore, the half volume coil was built with multiple channels for RF transmission to optimize $B_1$ uniformity.
Third, an optimized MEGA-sLASER sequence was implemented for enhanced GABA detection [29]. The sequence includes macromolecular nulling to minimize the contamination of the GABA signal by macromolecules. To optimize sequence performance, we employed frequency offset corrected inversion pulses (FOCI) as a means to increase the bandwidth of adiabatic pulses [19], reducing chemical shift displacement artifacts, thus improving the spatial localization of GABA signals.

## Coil setup specifications

A dedicated coil setup was constructed for a 7T MR system (Philips, Best, The Netherlands). The setup (Figure 18) consists of a shielded open half-cylinder multi-transmit head coil with 8 transmit elements. The 8 transmit elements are oval-shaped, with a size of 16x10 cm, facilitating $B_1^+$ shimming in three dimensions. Each element is matched to 50 Ω at 298 MHz when loaded with the participant's head. The transmit elements are arranged on the half cylinder with their direction to the back of the head (Figure 18b). Four elements are aligned along the direction of the $B_0$ field and two pairs of two elements orthogonal to the field (Figure 18c). To maximize inductive decoupling of the elements with their nearest neighbors, all elements are positioned with a partial overlap to their adjacent elements. The overlap was determined by minimizing the $S_{12}$ coupling in pairs of two, beginning with the center two elements followed by the paired orthogonal elements. This was done separately for each pair, without the other elements present. Subsequently, the overlap of the two orthogonal pairs to the center pair of elements was optimized by minimizing the $S_{12}$ coupling between the pairs. Finally, the outer two elements were positioned with an overlap to the orthogonal pairs of elements such that $S_{12}$ between the outer and the neighboring pair of elements was minimized. The elements are made of printed circuit board material and incorporate PIN diodes for detuning during receive. The RF coils are all actively detuned. The transmit elements are detuned during the receive phase and the receiver coils during the transmit phase. The elements are embedded in plexiglass. The surrounding U-shaped casing is custom made out of 6 mm thick polyoxymethylene, while aluminum foil was used as RF shielding to prevent coupling to the cables and conductors in the patient bed. The transmit elements are connected to two 4 kW and six 1 kW amplifiers via ceramic cable traps tuned to 298 MHz and transmit-receive switches. The amplifiers can be controlled in amplitude and phase for RF shimming over the visual cortex with a target $B_1^+$ of 20 µT.
A projection screen, with bars of adjustable length embedded in the coil casing, is mounted at the back of the coil. The screen size is 35 cm high by 56 cm wide, just small enough to fit in the scanner bore. A 17x20 $cm^2$ mirror is mounted on top of the coil casing on sliding bars that can be used to adjust the mirror location with respect to the participant's eyes (Figure 18a,b).

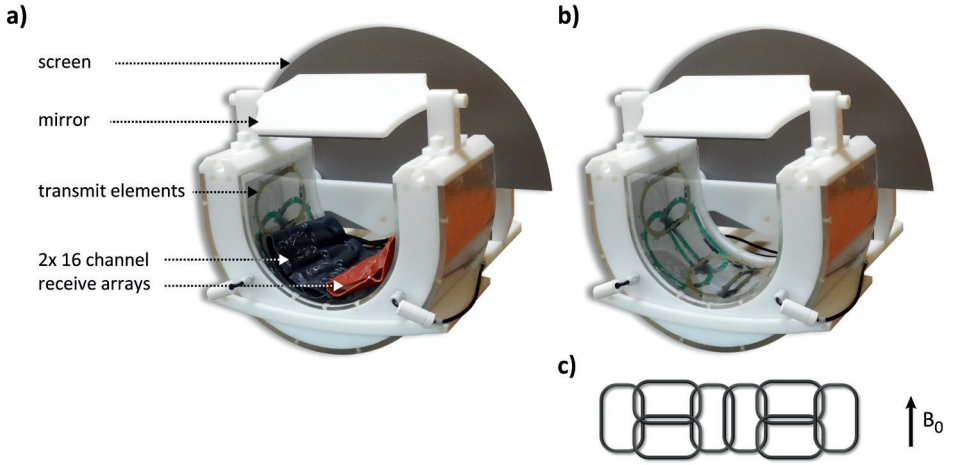


**Figure 18: Overview of the half volume coil setup. The transmit coil is open (u-shaped), allowing a visual stimulation with less mirrors and a large visual angle. Displayed is (a) a photograph of the coil setup in which the main components are labeled, including the 16 channel receive arrays, (b) a photograph of the coil setup without the receive arrays in place, showing the actual transmit elements, and (c) the transmit element arrangement in a schematic flat view, to illustrate the relative position of the 8 transmit elements to each other in more detail.**

Using back-projection of visual stimuli, the size of the projection achieved is 17x24 $cm^2$. The mirror can be positioned approximately 10 cm from the participant's eyes and angulated at 45°, resulting in a visual angle of more than 60°.
The receive part of the setup consists of two high-density 16-channel surface arrays (MR Coils B.V., Zaltbommel, The Netherlands). The high density receive arrays with small coil elements fit tightly on the participant's head, and are used to produce high resolution, high SNR, fMRI and MRI scans, with a receive depth extending several centimeters from the coil elements [30,31].

### Reference setup specifications

The performance of the custom-made coil setup was examined relative to the standard head coil setup of our 7T system. The standard setup consists of a dual-channel volume transmit coil in combination with a 32-channel receive head coil [32] (Nova Medical, MA, USA). The projection screen for the standard setup at our site is located at the front of the transmit coil and visible through prism glasses and a mirror at approximately 30 cm from the participant's eyes (Figure 19a). Using back-projection of visual stimuli the projection size achieved is 9 x 15 $cm^2$ yielding a visual angle of approximately 11°.

## Methods

The half volume coil setup was evaluated in two steps. First, the coil setup performance was evaluated by performing GABA measurements in four participants and fMRI in one participant,

focusing on the spatial extent of visual cortex activation and corresponding maximal achievable size of the GABA voxel. These results were evaluated relative to the standard head coil setup of our 7T system. Second, the SNR, speed, and stability of the GABA measurements were assessed by carrying out multiple repetitive measurements with the half volume coil setup in three participants at rest and in a phantom. All participants gave informed consent, and the work was approved by the Medical Ethics Committee of the University Medical Center Utrecht.

*Preparation and shimming*

Before acquiring the fMRI and GABA scans, a number of preparation steps were performed. A $T_1$-weighted scan was acquired for both setups as anatomical reference (3D gradient echo, TE/TR = 2.1/4.5 ms, flip angle of 5°, 2x2x2 mm voxel size, 250x250x198 $mm^3$ FOV, 99 sagittal slices, and a duration of 1 minute). For the half volume setup, an extra preparation phase was performed to shim the $B_1$ field on primary visual cortex (V1) based on 8 low flip angle gradient echo image series obtained by driving a different transmit element each time (multi-slice gradient echo series, with a TE/TR of 0.85/15 ms, flip angle: 10°, 3.9x3.9x10 $mm^3$ voxel size, 190x221x70 $mm^3$ FOV, 7 slices, and a duration of 7 seconds). The resulting $B_1^+$ level was assessed with a $B_1$ map (AFI [33], 3D gradient echo, TE/TR= 2.2/25 ms, flip angle: 50°, 3x3x3 $mm^3$ voxel size, 176x220x27 $mm^3$ FOV, 9 slices, and a duration of 1:47 minutes). The $B_1$ shimming procedure was performed for each participant individually and lasted around 10 minutes in total. $B_1$ shimming was not performed with the standard head coil. As final preparation step for both coil setups, a $B_0$ map of the posterior part of the brain was acquired, which was used for third order $B_0$ phase map shimming ($B_0$ map, 3D gradient echo, TE/TR = 1.96/4.7 ms, flip angle: 10°, 2x2x2 $mm^3$ voxel size, 190x190x70 $mm^3$ FOV, 35 coronal slices, and a duration of 1 minute). The linewidth of the water peak after $B_0$-shimming measured in the respective voxel, was on average 14±1 Hz (mean±sd) for the half volume coil setup and 15±2 Hz for the standard setup.

## Coil setup performance

The coil setup performance was evaluated in terms of spatial extent of visual cortex activation assessed with fMRI and corresponding maximal achievable voxel size and SNR for GABA MRS measurements. The performance of the custom-made coil setup was examined relative to the standard head coil setup of our 7T system. For the coil setup comparison, 4 participants were scanned with both setups. Three participants were scanned with 3 GABA edited MRS scans of 5:30 min each (no fMRI). One participant was scanned with both fMRI and 2 GABA edited MRS scans of 5:30 min.

*fMRI acquisition*

Visual stimuli consisted of a contrast-reversing checkerboard at 6 Hz, presented at full visual field to assess the spatial extent of activation in V1. The participant was instructed to fixate the

eyes on a central cross. The projection size was maximized according to the setup used. Full visual stimuli were presented in a block design with the contrast-reversing checkerboard 7 sec on/ 18 sec off. The duration of each run was 3.5 min. fMRI data were acquired using single-shot echo-planar imaging (EPI), with TE/TR= 27/1800 ms, flip angle: 60°, 1.5x1.5x1.5 $mm^3$ voxel size, 160x170x53 $mm^3$ FOV, and 35 slices orthogonal to the calcarine sulcus (Figure 19d).

*fMRI analysis*

fMRI data were analyzed using AFNI [34]. Data were corrected for motion and drift, and active voxels were identified with correlation of the stimulus waveform convolved with the canonical hemodynamic response. Activation maps were obtained by thresholding the resulting correlation coefficient maps at $p<10^{-5}$ uncorrected. The comparison between the activation maps of the two coils was performed by visual inspection of the spatial extent of activity in V1. To quantify the difference, an ROI analysis was performed as follows: The mean EPI image was computed for each fMRI time series, i.e. for each coil. A transformation matrix was obtained by co-registering the mean EPI images of the half-volume coil to the mean EPI image of the head coil using AFNI (3dWarpdrive function, rigid body transformation). This transformation matrix was applied to the correlation coefficient maps obtained for the half-volume coil data (3dAllineate function), bringing the activation maps of both coils in the same space. An ROI was selected on the mean EPI image of the head coil, encompassing that part of visual cortex which corresponds to the large MRS-voxel. Inside the ROI, the number of significantly active voxels were counted and compared between setups.

*MRS acquisition*

A single voxel was positioned to approximately encompass the active regions in V1 in both hemispheres. GABA edited spectroscopy was performed using a MEGA-sLASER sequence. For each participant, consecutive MRS scans were performed during one scanning session with the half volume coil setup, the session was repeated on a different day using the standard head coil setup. Three participants were scanned with 3 GABA edited MRS scans for both receive setups. The used MRS acquisition parameters for these 3 participants were: TE/TR= 74/5000 ms, spectral bandwidth: 4000 Hz, 32 odd-even pairs, 64 signal averages (NSA) and a total acquisition time of 5:30 min. The voxel size for the standard setup was 25x25x20 $mm^3$, and for the custom half-volume coil setup 40x30x30 $mm^3$. Besides these 3 participants, one additional participant was scanned with both fMRI and 2 MRS scans, where the generic voxel size and location of the MRS scan was adapted to match directly to the activation area observed with fMRI. The same MRS acquisition parameters were used as described above, except for a voxel size for the half volume coil setup of 40x40x20 $mm^2$, approximately spanning the fMRI activation maps (Figure 19, panels c,e,f,g). The MEGA-sLASER sequence combined two dual-banded editing pulses applied alternatively in odd/even acquisitions, to suppress the macromolecules and water signals simultaneously, while refocusing the 3.0 ppm GABA signal

[29]. FOCI pulses were implemented to increase the bandwidth of the adiabatic pulses [19]. Note that for an MEGA-sLASER sequence the acquisition of 1 editing pair, consists of 1 odd and 1 even spectrum, acquired over a period of 2 TR-intervals, which is counted as 2 signal averages (NSA). In addition to the water suppression of the two dual-banded editing pulses, VAPOR was applied with a window of 250 Hz. To also measure the water signal, each scan was preceded by an unsuppressed water pre-scan. No visual stimulation was applied for the MRS measurements.

*MRS data processing*

The spectra were processed using Matlab (MATLAB 8.3, MathWorks, MA, USA). The processing steps performed were: phasing and apodization (10 Hz), residual water removal by HLSVD fitting [35], retrospective frequency and phase alignment of the acquired NSA based on the choline and creatine signal [36,37], and lastly, adding the odd/even spectra resulting in an edited GABA spectrum [29]. Afterwards, the edited spectra were fitted to estimate the relative concentration of GABA and creatine (as a reference). The fit procedure was implemented in the same Matlab routine as the data processing steps. Fitting of the metabolite peaks was performed with an iterative Lorentzian fitting function, regulating peak amplitude, linewidth, frequency and offset ($0^{th}$ order baseline). For GABA, a double Lorentzian curve was fitted at 3.0 ppm with 14 Hz peak splitting. The creatine signal was fitted in the metabolite spectrum (odd and even subtracted). This was done as a reference, and as validation of the editing procedure. Both the area under the metabolite peak and the Cramer-Rao lower bound (CRLB) were estimated in the fitting procedure. Reported SNR values were calculated in time domain (FID), by dividing the signal amplitude of the fitted metabolite (GABA or creatine) in time domain by the standard deviation of the noise at the end (last 15%) of the acquired FID signal. This is done to obtain a metric for SNR which is independent of line shape [38]. SNR was calculated for both coil setups, as spectral resolution of the GABA resonance was similar for both setups, the SNR gain was quantified as the ratio of the two SNR values.

## SNR, speed, and stability of the GABA measurements

The SNR and stability of GABA measurements using the custom coil setup was assessed in 3 healthy volunteers and a phantom. The minimum achievable scan time with the coil setup was assessed by the number of averages required to reach a stable fit of the GABA peak, given by the number of averages required for the Cramer-Rao lower bound (CRLB) of the fit algorithm to reach a plateau. The stability of the GABA measurements was assessed by bootstrapping sets of spectra and computing the variance of the fitted GABA peak. The detection limits of the measurement and accuracy of the fit procedure were evaluated on a phantom.

*Acquired spectra*

MRS measurements were performed in 3 participants with a MEGA-sLASER sequence of 5:30 min and a voxel size of 40x30x30 $mm^3$. The parameters of the MEGA-sLASER sequence were the same as described above in the methods of the coil setup performance (A). The measurement was repeated 3 times per participant. Additionally, phantom measurements were performed. The phantom consisted of a 4 cm diameter ping-pong ball containing the metabolites GABA and creatine. A phantom with a small diameter was chosen, to avoid artifacts originating from standing waves. Standing waves can appear because the RF wavelength in a phantom at a field strength of 7 tesla is smaller than in vivo due to their dielectric differences. Because of the small diameter of the ball, the voxel size that could be fitted inside the volume of the phantom was 6 times smaller than that employed for the in-vivo measurements. To compensate for this difference in voxel size, a 6 fold higher concentration was chosen for the metabolites in the phantom (GABA: 6.6mM, creatine: 48mM) than assumed in vivo, matching the SNR between the phantom and in-vivo measurements. The MEGA-sLASER sequence parameters were the same as the in-vivo measurements, except for a voxel size of 17x20x17 $mm^3$. The measurement was repeated 6 times. Processing and fitting of the spectra was the same as described above in the methods of the coil setup performance (A). Though, in the phantom no choline was present, therefore, in the processing steps, alignment was based on the creatine signal only.

*SNR and speed*

To assess the minimum achievable scan time for a stable fit of the GABA peak, the number of averages (NSA) was incrementally increased and fitted. The area under the metabolite peak and the Cramer-Rao lower bound (CRLB) were estimated in the fitting procedure. The number of spectra that were averaged increased incrementally in steps of 2, starting from 2 to 64 (the entire scan), and the CRLB and SNR were computed at each step. The CRLB was calculated according to Cavassila et al. [39] The minimum achievable scan time (speed) was assessed by the number of spectra required for the CRLB of the fit algorithm to reach a plateau. For the data in this study, the plateau was defined as a rate of GABA CRLB decay of less than 10% for all participants.

*Stability*

To assess the GABA variation over a short period of time, a bootstrapping procedure [40] was employed. Bootstrapping was the preferred method, since the GABA peak was difficult to distinguish from noise for the spectrum obtained from one pair of edited data acquisition (2 NSA). With the bootstrapping procedure, an estimate could be obtained for the error and variance of GABA over a short period of time. In the bootstrap procedure, 500 random pairwise combinations of 16 NSA (8 pairs) were selected out of a total of 64 NSA (32 pairs). Consecutive odd/even acquisitions were kept together (per pair) during the randomization. Each selected combination was added and fitted, resulting in 500 fits of the GABA and creatine peaks. The

procedure was repeated to also bootstrap 32 NSA out of 64 NSA. The mean and standard deviation of the metabolite peak areas were calculated over the 500 fits (all bootstraps) to get an estimate for the error and variance of the metabolite peaks over a short period of time. Since the concentrations of the metabolites in the phantom do not change over time, the stability of the measurement method could be determined by applying the same procedure on the phantom measurements.

## Results

### Coil setup performance

Figure 19a and b show the standard 32-channel head coil setup and half volume coil setup respectively. The shaded (Figure 19a) and illuminated (Figure 19b) parts of the projection screen give an estimate of the difference in visual field of view between the two setups. The visual field of view achieved with the standard 32 channel head coil (Figure 19a) gives rise to activation in a part of the primary visual cortex, as measured with fMRI (Figure 19c). The large visual field of view achieved with the half volume coil setup (Figure 19b) enabled a larger activation encompassing about the entire extent of V1 (Figure 19e). The spatial extent of activation was larger than that obtained with the standard head coil, most notable in the upper part of V1 (upper bank of the calcarine sulcus) due to the elongated screen height (Figure 19 c,e). The increased spatial extent of activity allowed for a 2.5 fold larger MRS voxel size comprising of tissue that would be uniformly stimulated (Figure 19 f,g). The benefits of the increased voxel size obtained with the new setup can be seen in the MRS spectra by a substantial increase in SNR.

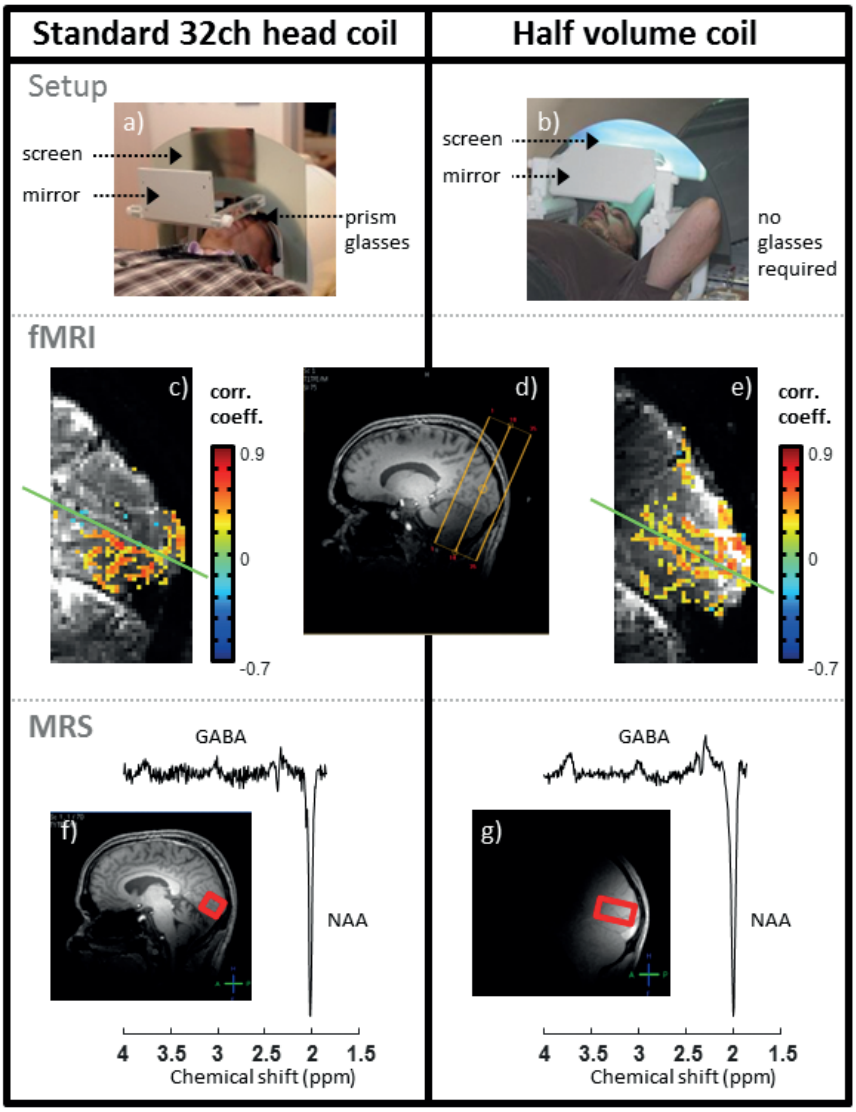


**Figure 19: Coil setup comparison of one participant. As reference, (a) the standard 32 channel head coil was used to compare with (b) the half volume coil. Both setups have a mounted screen for visual stimulation. The maximum visual field of view achieved with the setups (a,b) directly influences the extent of visual cortex activation as measured with fMRI (c,e). The fMRI activation map (correlation coefficient, $p<10^{-5}$ uncorrected) is overlaid on a sagittal view of the mean image of the EPI time series. The positioning of the fMRI slices is indicated on a $T_1$-weighted anatomical scan (d). Note that there is an increase in the extent of activation in the fMRI maps for the half volume coil setup (c,e), especially in superior-inferior direction. The added green lines mark the calcarine, specifically separating the upper and lower banks. The increase in activated tissue allows for a larger spectroscopy voxel of 40x40x20 $mm^3$ (g) as compared to the voxel of the reference setup of 25x25x20 $mm^3$ (f). The larger voxel size yields an SNR improvement of the GABA measurement, as can be seen in the two spectra (f,g). Both spectra consist of 16 NSA and are acquired in 1:23 minutes.**

Quantification of the increase in spatial extent of tissue activation and the increase in GABA SNR can be found in Table 4 and Table 5, respectively. The spatial extent of tissue activation was quantified as the number of active voxels in an ROI of equal size as the large MRS voxel. As can be seen in Table 4, the spatial extent of tissue activation for the half volume coil setup increased by approximately 19%, as compared to the standard 32 channel head coil. The GABA SNR was measured in 4 participants and the values can be found in Table 5. For the half volume coil setup, there is an increase in GABA SNR in all participants. The increase in GABA SNR varies per participant and is not directly equal to the increase in voxel size. Overall, the average increase in GABA SNR of the half volume coil over all participants is a factor of 2.2, as compared to the standard 32 channel head coil.

**Table 4: fMRI comparison between the two setups. The number of active voxels was counted in an ROI of equal position and size as the large MRS voxel**

| Reference setup (n) | Half volume coil (n) | Increase (%) |
|---|---|---|
| 2470 | 2947 | 19% |

**Table 5: GABA SNR comparison between the two setups.**

| Participant no. | MRS scans per setup (n) | GABA SNR (mean±sd) | | SNR increase, factor | Voxel size increase, factor |
|---|---|---|---|---|---|
| | | Reference setup | Half volume coil | | |
| 1 | 3 | 2.0±0.2 | 3.2±0.6 | 1.6 | 2.88 |
| 2 | 3 | 1.5±0.5 | 4.5±0.9 | 3.0 | 2.88 |
| 3 | 3 | 1.1±0.2 | 2.6±0.5 | 2.4 | 2.88 |
| 4 | 2 | 2.3±0.5 | 5.1±0.4 | 2.2 | 2.56 |
| All | 11 | 1.7±0.6 | 3.7±1.1 | 2.2 | 2.8 |

The resulting $B_1^+$ map obtained after shimming over the visual cortex is shown in Figure 20. Note that a $B_1^+$ of around 16 µT could be obtained in the visual cortex, despite the absence of transmit elements on the upper part of the head.

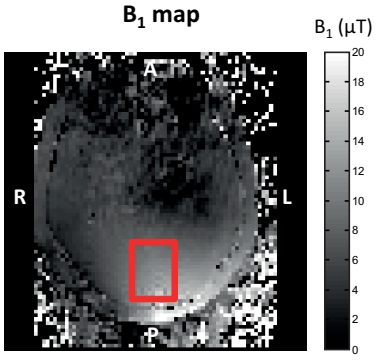


**Figure 20: A $B_1$ map acquired with the half volume coil. Beforehand, the $B_1$ field is shimmed for optimal performance in the back of the head, with a $B_1$ value of around 16 µT. The size and position of the GABA voxel is also indicated (red square).**

## SNR, speed, and stability of the GABA measurements

*Acquired spectra*

As an initial step, the quality of the acquired spectra was evaluated by visual inspection. Figure 21 shows an example of the acquired spectra after processing (phasing, apodization, alignment, addition of odd/even acquisitions) for the three participants, indicated in blue, green, and red respectively. Figure 21a-c, shows the edited spectra for one scan, per participant. For each scan 64 signal averages (NSA) are acquired. Note, that the GABA peak is clearly visible in the spectra of all three participants. To get an impression of the temporal fluctuation within these 64 NSA, the data of each participant was split into 4 sets of 16 NSA, which are shown in Figure 21e-g. These spectra appear noisier since they were computed from only 16 NSA. Still, the GABA peak can be distinguished in the spectrum, though, small differences in GABA peak area are hard to evaluate visually from these plots.

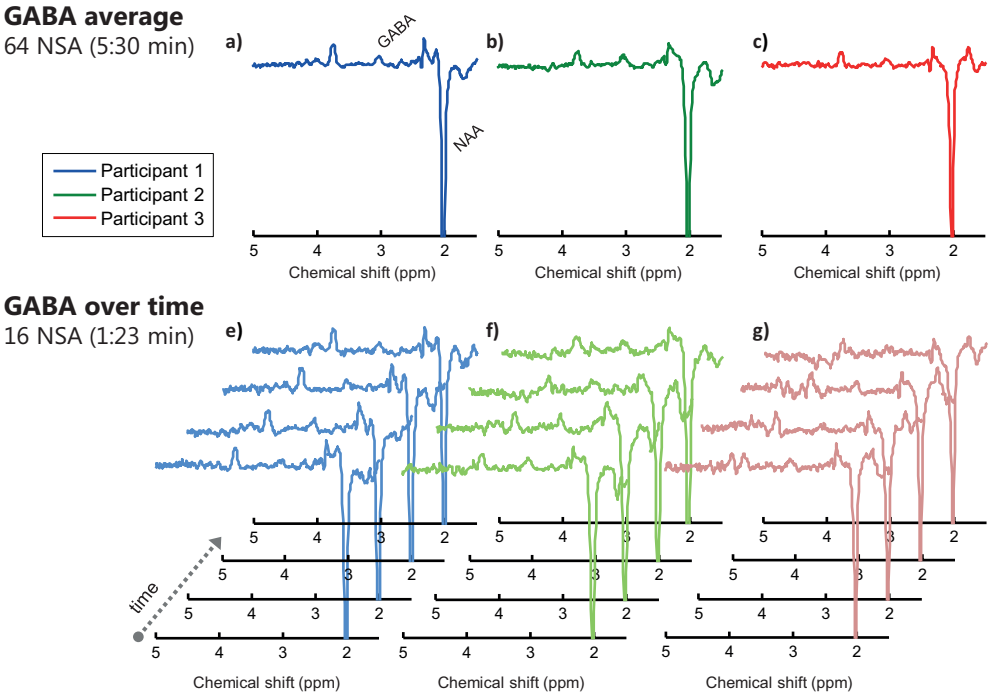


**Figure 21: Illustration of the acquired GABA edited spectra after processing. For all 3 participants (blue, green, red), one scan consisting of 64 NSA is shown (a-c, bright colors). At 3.0 ppm the GABA peak is clearly visible. Furthermore, each spectrum is split into 4 sets of 16 NSA (e-f, light colors), to also inspect the temporal behavior of the GABA peak within one scan. Even though these spectra consist of only 16 NSA and are thus noisier, the GABA peak can still be distinguished.**

*SNR and speed*

The analysis of the fitted spectral data of the phantom and the three different participants, is shown in Figure 22. GABA results are shown in Figure 22 a-c. Creatine results are shown as reference in Figure 22 d-f. An example of a spectral fit of GABA and creatine is shown in panels a and d respectively. The SNR and the fitting error (CRLB) were determined with different averaging, as shown in the graphs in Figure 22 b,c for GABA and e,f for creatine.

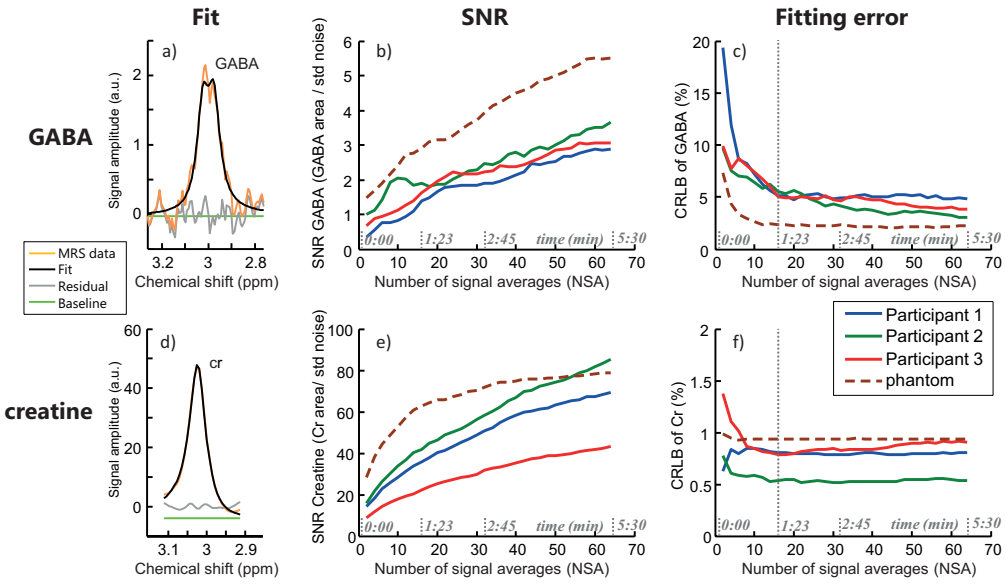


**Figure 22: Spectral fitting, SNR and goodness of fit. On the left, an example of the spectral fit is displayed for both metabolites GABA (a) and creatine (d). The two graphs in the center (b,e) show the SNR with different averaging. In all cases, the SNR increases with the number of averages. The two graphs on the right-hand side (c,f) display the fitting error, as described by the Cramér-Rao lower bound (CRLB). Note that less than 16 NSA (indicated by a vertical dotted line) are needed for the GABA fit to become stable, as estimated by the required number of averages for the CRLB to reach a plateau. After 16 NSA, the rate of GABA CRLB decay is less than 10% for all participants. The acquisition of 16 NSA converts to a scan time of less than 1:23 min.**

The SNR improves with increasing number of averages, as expected for both GABA (Figure 22b) and creatine (Figure 22e), and for both in-vivo and phantom measurements (solid and dotted lines respectively). The goodness of fit results for the in-vivo measurements (Figure 22 c,f) showed that approximately 16 averages are needed to reach a stable fit for GABA, and about 8 averages for creatine, as estimated by the required number of averages for the CRLB to reach a plateau. After 16 NSA, the rate of GABA CRLB decay is less than 10% for all participants. For the phantom measurements, less averages (<10) are needed for the CRLB to reach a plateau for both GABA and creatine. The required number of averages (NSA) must be multiple of 2, since one average (1 NSA) either contains an odd or an even editing spectrum.

The corresponding scan time for 16 averages is 1:23 min, the full 64 averaged editing sets take 5:30 minutes to acquire.

The GABA concentration over time, for 3 repeated MRS scans in three participants at rest, is shown in Figure 23. The GABA concentration is displayed in reference to creatine, both, when averaging consecutive sets of 16 NSA (Figure 23a), and as a moving average (Figure 23b) with a window of 16 NSA and a step size of 2 NSA. Each data point consists of 16 NSA, corresponding to a short scan time of 1:23 minutes. Note that, in both graphs, the individual GABA concentration in reference to creatine fluctuates over time for repeated GABA measurements at rest. The observed variability of the GABA over creatine ratios can predominantly be attributed to the variability of the GABA concentrations, since the coefficient of variation of creatine is on average only 1.4% within scans, and 3.8% between scans (of 64 NSA). To further assess the size and origin of the GABA fluctuations a bootstrap analysis is performed, determining the stability of the GABA measurements.

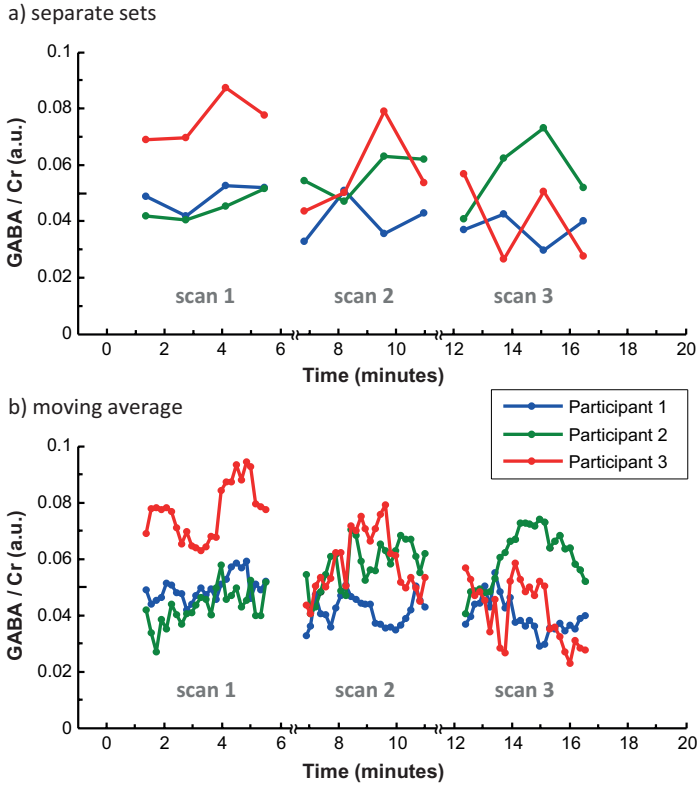


**Figure 23: GABA concentration over time referenced to creatine, as measured by 3 repeated GABA edited spectroscopy scans in 3 participants at rest. The GABA concentration is displayed (a) when averaging consecutive sets of 16 NSA, and (b) as a moving average with a window of 16 NSA and a step size of 2 NSA. Each data point consists of 16 NSA, corresponding to a short scan time for GABA edited spectroscopy of 1:23 min. The individual GABA concentration at rest fluctuates over time.**

*Stability*

The GABA stability results of the repeated spectroscopy measurements are shown in Figure 24. Both, 6 repeated scans in a phantom (Figure 24 a,c,e,g) and 3 repeated scans in 3 participants (Figure 24 b,d,f,h) are displayed. A bootstrap analysis is performed, both for averaging 16 NSA (Figure 24 a-d) and 32 NSA (Figure 24 e-h) out of a total of 64 NSA. For each data point, the relative metabolite concentration is plotted, as defined by the area under either the GABA (Figure 24, top row) or creatine peak (Figure 24, bottom row). The graphs show the results for the repeated scans separately (6 for the phantom, 3 for each participant). The error bars indicate the mean and standard deviation of the relative GABA or creatine concentrations computed from the 500 fits of the bootstrap procedure. The percentage displayed next to the error bars represents the ratio of standard deviation and the mean. For the phantom, this ratio of the standard deviation and the mean of the measured GABA concentrations is less than 5% for 16 NSA and less than 3% for 32 NSA (Figure 24 a,c). For creatine, this is less than 0.5% in both cases (Figure 24 e,g), which is similar to the total system stability. In-vivo, the ratio of the standard deviation and the mean of the measured GABA concentrations is between 14-25%

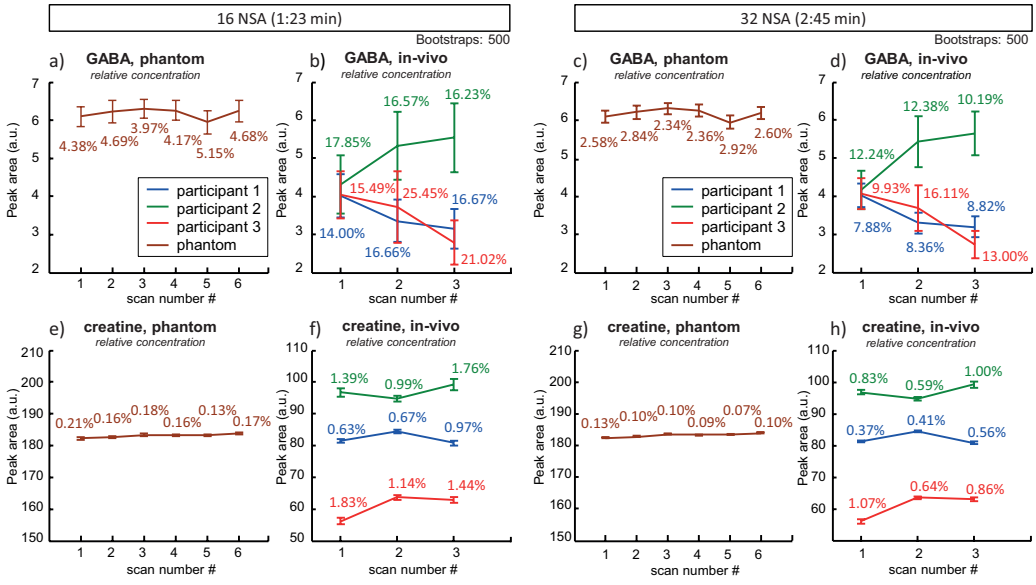


**Figure 24: Repeated MRS measurements of GABA (a-d) and creatine (e-f) for the phantom (a,c,e,g) and in-vivo (b,d,f,h). The graphs show the results for the repeated scans separately (6 for the phantom, 3 for each participant). To estimate the variation of the concentrations per scan, 500 bootstrap fits were performed. Results are shown for spectra consisting of 16 signal averages (a,b,e,f) and 32 signal averages (c,d,g,h). The mean, standard deviation (error bar) and their ratio (percentage) across the 500 estimated GABA and creatine concentrations is shown in the graphs. Despite the same intrinsic SNR of GABA, the in-vivo levels show, per scan, higher fluctuations (16 NSA: 14-25%, 32 NSA: 8-16%) than the phantom results (16 NSA: 5%, 32 NSA: 3%).**

for 16 NSA and between 8-16% for 32 NSA (Figure 24 b,d). For creatine this is between 0.5-2% for both 16 and 32 NSA (Figure 24 f,h). The variation of GABA is larger than the variation of creatine.

Since the measured metabolite values (Figure 24) are relative concentrations, the ratio of GABA to other metabolites (Table 6 and Table 7) was also calculated to facilitate comparison with other studies. The GABA ratio is calculated with respect to the reference metabolite, creatine (Table 6), and water (Table 7). The GABA ratios for the 3 scans per participant are shown in both tables. Also, descriptive information is reported per participant, such as: the mean, standard deviation (SD), coefficient of variation (CV, %) and the absolute difference in terms of percentage (Abs Diff, % defined as the difference between first and last scan, divided by the mean signal of the participant). The last row shows statistics for the average over all participants, reported as the mean coefficient of variation and mean absolute difference.
Note that the mean coefficient of variation over all participants for the GABA measurements when referenced to creatine is 18% (range: 14% – 25%) and when referenced to water it is 16% (range: 13% – 20%). The mean absolute variation of GABA referenced to creatine is 33% (range: 23% - 50%) and referenced to water it is 30% (range: 24% - 38%).

**Table 6: Repeated measurements of GABA concentrations referenced to creatine, using a MEGA-sLASER sequence. The rows indicate the different participants. Columns 2 to 4 show the measured GABA ratios. The remaining columns show the calculated statistics, characterizing the variation in the GABA measurements.**

| Participant | GABA/cr (x$10^{-2}$ IU) | | | Mean | SD | CV (%) | Abs Diff (%) |
|---|---|---|---|---|---|---|---|
| | Scan 1 | 2 | 3 | | | | |
| 1 | 4.94 | 3.90 | 3.95 | 4.27 | 0.6 | 13.7% | 23.2% |
| 2 | 4.30 | 5.74 | 5.68 | 5.24 | 0.8 | 15.6% | 26.4% |
| 3 | 7.28 | 5.80 | 4.34 | 5.80 | 1.5 | 25.3% | 50.6% |
| Mean | | | | | | 18.2% | 33.4% |

*IU, institutional units; SD, standard deviation; CV, coefficient of variation; Abs Diff, difference between first and last scan, divided by the mean.*

**Table 7: Repeated measurements of GABA concentrations referenced to water, using a MEGA-sLASER sequence**

| Participant | GABA/$H_2O$ (x$10^{-5}$ IU) | | | Mean | SD | CV (%) | Abs Diff (%) |
|---|---|---|---|---|---|---|---|
| | Scan 1 | 2 | 3 | | | | |
| 1 | 4.23 | 3.45 | 3.33 | 3.67 | 0.5 | 13.3% | 24.2% |
| 2 | 4.49 | 5.73 | 5.95 | 5.39 | 0.8 | 14.7% | 27.3% |
| 3 | 4.37 | 4.04 | 2.93 | 3.78 | 0.8 | 19.9% | 38.0% |
| Mean | | | | | | 16.0% | 29.9% |

*IU, institutional units; SD, standard deviation; CV, coefficient of variation; Abs Diff, difference between first and last scan, divided by the mean.*

## Discussion

The aim of this study was to reduce scan time and increase GABA sensitivity for edited spectroscopy in the visual cortex. The developed half volume coil setup increased the spatial extent of fMRI activation, enabling an increase voxel size, yielding a gain in GABA SNR by a factor of 2.2 as compared to a conventional head coil setup at 7T. The gain in SNR can be exchanged for shorter acquisition times. Using this setup and the MEGA-sLASER sequence with FOCI pulses, we were able to obtain a reliable fit of the GABA peak in-vivo in 1:23 minutes. The stability of the GABA measurements, with the approach employed here, was sufficient to detect GABA with an accuracy of 3% in 2:45 min and 5% in 1:23 min, as determined with the GABA phantom. The GABA measurements show larger fluctuations in-vivo, than in the phantom, suggesting the influence of physiological variability. In-vivo, the concentration changes of GABA measurements were on the order of 18% per participant, which suggests that physiological variability might be substantially higher than the stability of the setup and approach presented.

Our approach involved multiple avenues to enhance GABA MRS sensitivity. A half volume multi-transmit coil was constructed and combined with a large screen for visual stimulation, enabling a projection size, with a visual angle, of more than 60 degrees. As no close fitting volume transmit coil was used, $B_1$ shimming was performed with the constructed transmit array of the half volume coil. This resulted in a uniform field over the spectroscopy voxel, but also assured sufficient $B_1^+$ to use the short adiabatic RF pulses, required for the optimized GABA acquisition. GABA MRS signal was acquired with a MEGA-sLASER sequence with macromolecular nulling and FOCI editing pulses to enhance the sensitivity and spatial localization of GABA signals. High density receive surface arrays were used for signal reception which yield a high SNR in the visual cortex, for a distance of several centimeters from the coil elements. The effectiveness of the constructed setup at 7T is discussed in more detail below.



### Coil setup performance

The achieved extent of tissue activation in the visual cortex with the half volume coil setup, as measured with fMRI, was larger than with the standard head coil setup, most evident for V1 (Figure 19 c,e). It is expected that this is caused predominantly due to the increased visual angle (larger presentation screen) of the half volume coil setup. The increased activated tissue volume encompassed about the entire extent of V1. The increase in active voxels within the voxel ROI was relatively modest, on the order of 19%, likely because other visual areas were also included in the ROI (such as V2 or V3). The difference in spatial extent of activation between setups was translated to 2.8-fold larger spectroscopy volumes containing stimulated tissue. The GABA spectroscopy comparison between setups showed a gain in SNR by a factor of 2.2 on average for the half volume coil setup. The increase in GABA SNR comes directly from the increased voxel size, which is possible due to a larger activated cortical volume when

using the half volume coil setup. The achieved gain in SNR can be used either to perform measurements with higher GABA sensitivity or to enable shorter measurement times. Though, the gain in GABA SNR of 2.2 did not scale linearly with the gain in voxel size of 2.8. This can be expected since the sensitivity profile of the surface receive coils decays towards the center of the brain, and the voxel size was expanded towards the center of the brain. The use of a dedicated coil setup for the back of the brain enhances the SNR close to the coils, but at the same time results in lowered SNR towards the center of the brain.

## SNR, speed, and stability of the GABA measurements

The SNR of the GABA measurements increased with the number of signal averages (NSA) as expected. The goodness of fit of the GABA peak also improved with the number of signal averages, as expressed by the CRLB, and became stable in less than 16 NSA, which can be acquired in less than 1:23 minutes. When comparing the 1:23 minutes acquisition time to the 6-30 minutes typical scan times reported for GABA edited spectroscopy in literature [16], an approximate 4 to 20 fold improvement is achieved. However, when compared to the typical fMRI acquisition times of 1 to 4 seconds, there is still an order of magnitude difference.

The stability and repetition accuracy of the 16 NSA and 32 NSA GABA measurement was 5% and 3% respectively, as determined with a GABA phantom. This 3-5% variability in GABA measurements for the phantom data suggests that GABA changes of at least 3% can be detected within 2:45 minutes and 5% in 1:23 minutes, excluding physiological confounds. Then again, in vivo, the variability of the GABA peaks was substantially higher, both within and between repetitive GABA scans in all participants. The intra scan variability in GABA levels (variability within all averages of one scan) ranged from 8-16% (32 NSA) and 14-25% (16 NSA) in a period of 5:30 minutes. The inter scan variability (variation between consecutive scans) is larger (CV:18%, Abs Diff 30%) than the variation within one the scan (8-16% for 32 NSA, and 14-25% for 16 NSA). The variability of the GABA signals is substantially larger than those caused by intrinsic system noise and measurement instabilities, as assessed by the phantom measurements. The origin of this variability is unclear, however, given the much lower variability observed for the phantom measurements it could be of physiological origin.

Noise and motion of the participant can affect the GABA level variation as well. However, a spectrum of poor quality due to motion of the participant would be averaged out in the bootstrapping procedure, which selects 500 sets of 16 or 32 NSA from a total of 64 NSA. Extreme artifacts of a single spectrum (1 NSA) per scan (5:30 min) would therefore not have a big impact on the results obtained for the in-vivo measurements. The larger voxel size might increase variability of GABA as well. Anatomically, a larger voxel includes more neurons. A larger pool of active and in-active neurons at different locations could possibly explain the increased physiological variations. In this study, the participants were asked to look at black presentation screen, but were free to close their eyes as well. This could be an additional factor of variation. The variability of GABA is larger than the variability of creatine, which can

be expected since the absolute concentration of creatine is in general almost 8 times larger than the concentration of GABA. Therefore, small absolute changes of creatine would be less visible in the large creatine pool. In case of GABA, small absolute changes would result in a big relative change of the total GABA concentration, since the total GABA concentration is low. When considering a physiological origin of the observed in-vivo variability in GABA levels, the results may imply that GABA changes of at least 8-16% may be needed in order to be detected in a functional MRS experiment. The high GABA variability impairs the possibility of detecting evoked GABA fluctuations, questioning the motivation to aim for GABA measurements with a high SNR and a short scan time. However, measurements that are performed with event related paradigms may still benefit, and may be able to identify evoked GABA fluctuations from background variability. Another reason for the of the observed in-vivo variability in GABA levels could be that the presumed resting state of the visual cortex during our measurements may not hold for GABA physiology. Consequently, new paradigms may be required to set the brain in resting GABA states in order to assess functionally induced alterations in GABA levels. Our result suggests that physiological alterations in GABA levels can occur within the duration of more common MRS acquisitions that average spectra over 6-30 minutes. However, further work is needed to confirm assumptions about the source of variability of GABA in-vivo.

## Methodological considerations

A number of methodological aspects have to be taken into account with respect to the coil setup design. Small surface coils tend to yield the highest SNR within their sensitive area, but their receive sensitivity is not very uniform and decreases with distance from the coils [41]. The high density surface coils used in the present setup allow for high sensitivity and SNR up to at least a 4-5 cm distance from the coil elements [30,31]. In the coil setup design, a choice was made to increase the visual angle by increasing the screen size. However, this approach can be argued. It may be possible to achieve the same visual angle with head coil mountable goggles near the participant's eyes, minimizing the distance between the screen and the eyes of the participant [42,43]. Still, the electronics on the goggles should not interfere with the magnetic field, and the compatibility with a 7T scanner may be an issue. Another confound of large voxel sizes is the stronger demands on $B_1$ and $B_0$ shimming. To resolve this issue we adopted multi-transmit technology in the half volume coil design. Though, the limited availability of multi-transmit technology at 7T systems might be a drawback. In this study, $B_1$ shimming is performed for each participant individually, which extended the scanning protocol with approximately 10 minutes. Though, when aiming for a short scan protocol, it is also possible to fix the transmit channels to one general setting. The spectroscopy scans are acquired with a peak $B_1$ peak amplitude in accordance with the value found in the $B_1$-map. If the value is lower than expected, the RF pulse durations in the sequence can become longer. With the current hardware there is still room for $B_1$ field improvement, as the transmit channels are not yet maximally optimized in amplitude and phase settings. The refocusing RF pulses used in the

sequence are adiabatic RF pulses and are therefore less sensitive to $B_1$ variations. However, the RF pulses used for MRS editing are conventional pulses, which can still be a source of variation. Despite the possible $B_1$-field non-uniformity because of the large MRS voxel, we do expect it to be stable over time. So in that sense, it does not explain the variations we measure over time. As opposed to $B_1$ shimming, the $B_0$ shimming in the visual cortex is hardly compromised, particularly considering the broadened spectral lines of GABA due to inherent J-coupling. Finally, the voxel size is mainly enlarged towards the center of the brain, where the distance to the RF coils is greater. Consequently, the SNR may not linearly scale with the enlargement of the voxel.

### Technical comparison with other studies

Several studies have demonstrated changes in GABA levels between patient populations, however, less is known about short-term temporal (minute) GABA level fluctuations in individuals [16]. Repeatability studies that measure GABA over time [44-47] report lower fluctuations in GABA per participant with a CV of 4-12% (mean coefficient of variation, for GABA plus macromolecules (MM) referenced to either water or creatine at 3T). However, these studies use a MEGA-PRESS sequence, without macromolecular suppression. Macromolecular contamination can have a significant impact on the GABA results [48,49]. Two studies performed at 7T, which do incorporate macromolecular suppression show a higher GABA CV of 9.5% [50] and 13.6% [51], with a total acquisition time of 12:48 and 8:00 minutes respectively. In addition, a recent study performed at 3T which includes macromolecular suppression and motion navigation, reports a CV of 13.3 – 17.6% [52] with an acquisition time of 10:40 minutes. These values come closer to the CV of GABA variation found in our study of 16%-18%, acquired at 7T in 5:30 minutes. In our study, we used macromolecular nulled GABA editing techniques that are obtained at a relatively short total acquisition time. When neglecting consequences of signal overlap, functional GABA MRS acquisitions may be obtained at even higher temporal resolutions using non-edited, short echo time MRS acquisition [53]. Similar as obtained for functional lactate MRS, these may reveal even faster GABA fluctuations in the visual cortex [54,55]. Despite the short echo time, care must be taken in assuming constant levels of overlapping resonances and fitting accuracies [49,56]. Short echo time MRS is more heavily dependent on data quality and fitting constraints for the quantification of GABA [17].

Studies that combine fMRI and GABA MRS are interesting from a fundamental point of view, because they may provide insight into the connection between neuronal metabolism and BOLD hemodynamics. Furthermore, they are also interesting from a clinical point of view, because imbalances in excitatory and inhibitory processes are believed to be implicated in several neuropathological conditions such as stroke, schizophrenia, autoimmune inflammation, Parkinson's disease and epilepsy [7]. For the schizophrenia studies that focus on frontal cortex, the proposed setup with the advantages of a large screen, would not be beneficial. Though,

the application of the setup is widespread, as it can be extended to other brain regions, such as the temporal lobe where perception of objects and faces is based, which can be impaired in schizophrenia. Or it can be extended to other patient groups, for example neurofibromatosis type 1 patients in which a GABA deficit is present in the visual cortex [57]. In both cases our setup can enhance GABA sensitivity or reduce measurement time to approach measurements at a physiological time scale, gaining insight into the diseased brain system.

## Conclusion

The half volume setup enables an increase in the area of visual stimulation, allowing activation of almost the entire primary visual cortex (V1). Also, more than an average 2.2-fold SNR gain in GABA detection of stimulated tissue can be achieved, as compared to a conventional head coil setup. The SNR, speed and stability of the sensitivity optimized method employed at 7T is sufficient to detect GABA with an accuracy of 5%, within a fast scan time of less than 2 minutes, as determined in a phantom. This brings functional GABA detection at temporal resolutions that match closer to activation paradigms. However, the repetitive in-vivo measurements per individual show a large GABA variation of 14-25% at rest, suggesting a physiological origin. Overall, the results indicate new possibilities and considerations for GABA spectroscopy measurements in the field of human brain physiology.

## References


1. Kim SG, Ogawa S. Biophysical and physiological origins of blood oxygenation level-dependent fMRI signals. J Cereb Blood Flow Metab 2012;32(7):1188-1206.
2. Ogawa S, Lee TM, Kay AR, Tank DW. Brain magnetic resonance imaging with contrast dependent on blood oxygenation. Proc Natl Acad Sci U S A 1990;87(24):9868-9872.
3. Lauritzen M, Mathiesen C, Schaefer K, Thomsen KJ. Neuronal inhibition and excitation, and the dichotomic control of brain hemodynamic and oxygen responses. Neuroimage 2012;62(2):1040-1050.
4. Logothetis NK. What we can do and what we cannot do with fMRI. Nature 2008;453(7197):869-878.
5. Attwell D, Buchan AM, Charpak S, Lauritzen M, Macvicar BA, Newman EA. Glial and neuronal control of brain blood flow. Nature 2010;468(7321):232-243.
6. Buzsaki G, Kaila K, Raichle M. Inhibition and brain work. Neuron 2007;56(5):771-783.
7. Donahue MJ, Near J, Blicher JU, Jezzard P. Baseline GABA concentration and fMRI response. Neuroimage 2010;53(2):392-398.
8. Logothetis NK, Pauls J, Augath M, Trinath T, Oeltermann A. Neurophysiological investigation of the basis of the fMRI signal. Nature 2001;412(6843):150-157.
9. Muthukumaraswamy SD, Edden RA, Jones DK, Swettenham JB, Singh KD. Resting GABA concentration predicts peak gamma frequency and fMRI amplitude in response to visual stimulation in humans. Proc Natl Acad Sci U S A 2009;106(20):8356-8361.
10. Mangia S, Tkac I, Gruetter R, Van De Moortele PF, Giove F, Maraviglia B, Ugurbil K. Sensitivity of single-voxel 1H-MRS in investigating the metabolism of the activated human visual cortex at 7 T. Magn Reson Imaging 2006;24(4):343-348.

11. Northoff G, Walter M, Schulte RF, Beck J, Dydak U, Henning A, Boeker H, Grimm S, Boesiger P. GABA concentrations in the human anterior cingulate cortex predict negative BOLD responses in fMRI. Nat Neurosci 2007;10(12):1515-1517.
12. Kuhn S, Schubert F, Mekle R, Wenger E, Ittermann B, Lindenberger U, Gallinat J. Neurotransmitter changes during interference task in anterior cingulate cortex: evidence from fMRI-guided functional MRS at 3 T. Brain Struct Funct 2016;221(5):2541-2551.
13. Lipp I, Evans CJ, Lewis C, Murphy K, Wise RG, Caseras X. The relationship between fearfulness, GABA+, and fear-related BOLD responses in the insula. PLoS One 2015;10(3):e0120101.
14. Michou E, Williams S, Vidyasagar R, Downey D, Mistry S, Edden RA, Hamdy S. fMRI and MRS measures of neuroplasticity in the pharyngeal motor cortex. Neuroimage 2015;117:1-10.
15. Bednarik P, Tkac I, Giove F, DiNuzzo M, Deelchand DK, Emir UE, Eberly LE, Mangia S. Neurochemical and BOLD responses during neuronal activation measured in the human visual cortex at 7 Tesla. J Cereb Blood Flow Metab 2015;35(4):601-610.
16. Puts NA, Edden RA. In vivo magnetic resonance spectroscopy of GABA: a methodological review. Prog Nucl Magn Reson Spectrosc 2012;60:29-41.
17. Mullins PG, McGonigle DJ, O'Gorman RL, Puts NA, Vidyasagar R, Evans CJ, Edden RA. Current practice in the use of MEGA-PRESS spectroscopy for the detection of GABA. Neuroimage 2014;86:43-52.
18. Cleve M, Gussew A, Reichenbach JR. In vivo detection of acute pain-induced changes of GABA+ and Glx in the human brain by using functional 1H MEGA-PRESS MR spectroscopy. Neuroimage 2015;105:67-75.
19. Arteaga de Castro CS, Boer VO, Andreychenko A, Wijnen JP, van der Heide UA, Luijten PR, Klomp DW. Improved efficiency on editing MRS of lactate and gamma-aminobutyric acid by inclusion of frequency offset corrected inversion pulses at high fields. NMR Biomed 2013;26(10):1213-1219.
20. Adams DL, Horton JC. Ocular dominance columns: enigmas and challenges. Neuroscientist 2009;15(1):62-77.
21. Sengupta S, Roebroeck A, Kemper VG, Poser BA, Zimmermann J, Goebel R, Adriany G. A Specialized Multi-Transmit Head Coil for High Resolution fMRI of the Human Visual Cortex at 7T. PLoS One 2016;11(12):e0165418.
22. Adriany G, Gruetter R. A half-volume coil for efficient proton decoupling in humans at 4 tesla. J Magn Reson 1997;125(1):178-184.
23. Adriany G, Pfeuffer J, Yacoub E, Van De Moortele P, Shmuel A, Andersen P, Hu X, Vaughan JT, Ugurbil K. A Half-Volume Transmit / Receive Coil Combination for 7 Tesla Applications. The 9th Annual Meeting of the ISMRM 2001, Glasgow, Scotland, p1097 2001.
24. Avdievich NI, Peshkovsky AS, Kennan RP, Hetherington HP. SENSE imaging with a quadrature half-volume transverse electromagnetic (TEM) coil at 4T. J Magn Reson Imaging 2006;24(4):934-938.
25. Ballon D, Graham MC, Miodownik S, Koutcher JA. A 64 MHz half-birdcage resonator for clinical imaging. Journal of Magnetic Resonance (1969) 1990;90(1):131-140.
26. Fujita H, Braum WO, Shvartsman SM, Brown RW, Reisker TJ, Molyneaux DA, Morich MA. An optimized open quadrature distributed RF surface coil. The 6th Annual Meeting of the ISMRM, Sydney, Australia p645 1998.
27. Peshkovsky AS, Kennan RP, Fabry ME, Avdievich NI. Open half-volume quadrature transverse electromagnetic coil for high-field magnetic resonance imaging. Magn Reson Med 2005;53(4):937-943.
28. Katscher U, Bornert P. Parallel RF transmission in MRI. NMR Biomed 2006;19(3):393-400.
29. Andreychenko A, Boer VO, Arteaga de Castro CS, Luijten PR, Klomp DW. Efficient spectral editing at 7 T: GABA detection with MEGA-sLASER. Magn Reson Med 2012;68(4):1018-1025.
30. Petridou N, Italiaander M, van de Bank BL, Siero JC, Luijten PR, Klomp DW. Pushing the limits of high-resolution functional MRI using a simple high-density multi-element coil design. NMR Biomed 2013;26(1):65-73.

31. Batson MA, Petridou N, Klomp DW, Frens MA, Neggers SF. Single session imaging of cerebellum at 7 Tesla: obtaining structure and function of multiple motor subsystems in individual subjects. PLoS One 2015;10(8):e0134933.
32. Ledden PJ, Mareyam A, Wang S, van Gelderen P, Duyn J. 32 Channel Receive-Only SENSE Array for Brain Imaging at 7T. Proceedings of the 15th Annual Meeting of the ISMRM, Berlin, Germany 2007 p 242 2007.
33. Yarnykh VL. Actual flip-angle imaging in the pulsed steady state: a method for rapid three-dimensional mapping of the transmitted radiofrequency field. Magn Reson Med 2007;57(1):192-200.
34. Cox RW. AFNI: software for analysis and visualization of functional magnetic resonance neuroimages. Comput Biomed Res 1996;29(3):162-173.
35. Cabanes E, Confort-Gouny S, Le Fur Y, Simond G, Cozzone PJ. Optimization of residual water signal removal by HLSVD on simulated short echo time proton MR spectra of the human brain. J Magn Reson 2001;150(2):116-125.
36. Edden RA, Puts NA, Harris AD, Barker PB, Evans CJ. Gannet: A batch-processing tool for the quantitative analysis of gamma-aminobutyric acid-edited MR spectroscopy spectra. J Magn Reson Imaging 2014;40(6):1445-1452.
37. Waddell KW, Avison MJ, Joers JM, Gore JC. A practical guide to robust detection of GABA in human brain by J-difference spectroscopy at 3 T using a standard volume coil. Magn Reson Imaging 2007;25(7):1032-1038.
38. Kreis R. Issues of spectral quality in clinical 1H-magnetic resonance spectroscopy and a gallery of artifacts. NMR Biomed 2004;17(6):361-381.
39. Cavassila S, Deval S, Huegen C, van Ormondt D, Graveron-Demilly D. Cramer-Rao bounds: an evaluation tool for quantitation. NMR Biomed 2001;14(4):278-283.
40. Davison AC, Hinkley DV. Bootstrap Methods and their Application. Cambridge: Cambridge University Press; 1997.
41. Asher KA, Bangerter NK, Watkins RD, Gold GE. Radiofrequency coils for musculoskeletal magnetic resonance imaging. Top Magn Reson Imaging 2010;21(5):315-323.
42. Choubey B, Jurcoane A, Muckli L, Sireteanu R. Methods for dichoptic stimulus presentation in functional magnetic resonance imaging - a review. Open Neuroimag J 2009;3:17-25.
43. James TW, Gauthier I. Repetition-induced changes in BOLD response reflect accumulation of neural activity. Human Brain Mapping 2006;27(1):37-46.
44. Bogner W, Gruber S, Doelken M, Stadlbauer A, Ganslandt O, Boettcher U, Trattnig S, Doerfler A, Stefan H, Hammen T. In vivo quantification of intracerebral GABA by single-voxel (1) H-MRS-How reproducible are the results? Eur J Radiol 2010;73(3):526-531.
45. Near J, Ho YC, Sandberg K, Kumaragamage C, Blicher JU. Long-term reproducibility of GABA magnetic resonance spectroscopy. Neuroimage 2014;99:191-196.
46. O'Gorman RL, Michels L, Edden RA, Murdoch JB, Martin E. In vivo detection of GABA and glutamate with MEGA-PRESS: reproducibility and gender effects. J Magn Reson Imaging 2011;33(5):1262-1267.
47. Evans CJ, McGonigle DJ, Edden RA. Diurnal stability of gamma-aminobutyric acid concentration in visual and sensorimotor cortex. J Magn Reson Imaging 2010;31(1):204-209.
48. Harris AD, Puts NA, Barker PB, Edden RA. Spectral-editing measurements of GABA in the human brain with and without macromolecule suppression. Magn Reson Med 2015;74(6):1523-1529.
49. Terpstra M, Ugurbil K, Gruetter R. Direct in vivo measurement of human cerebral GABA concentration using MEGA-editing at 7 Tesla. Magn Reson Med 2002;47(5):1009-1012.
50. Prinsen H, de Graaf RA, Mason GF, Pelletier D, Juchem C. Reproducibility measurement of glutathione, GABA, and glutamate: Towards in vivo neurochemical profiling of multiple sclerosis with MR spectroscopy at 7T. J Magn Reson Imaging 2017;45(1):187-198.
51. Wijtenburg SA, Rowland LM, Edden RA, Barker PB. Reproducibility of brain spectroscopy at 7T using conventional localization and spectral editing techniques. J Magn Reson Imaging 2013;38(2):460-467.

52. Saleh MG, Near J, Alhamud A, Robertson F, van der Kouwe AJ, Meintjes EM. Reproducibility of macromolecule suppressed GABA measurement using motion and shim navigated MEGA-SPECIAL with LCModel, jMRUI and GANNET. MAGMA 2016;29(6):863-874.
53. Near J, Andersson J, Maron E, Mekle R, Gruetter R, Cowen P, Jezzard P. Unedited in vivo detection and quantification of gamma-aminobutyric acid in the occipital cortex using short-TE MRS at 3 T. NMR Biomed 2013;26(11):1353-1362.
54. Mekle R, Kuhn S, Pfeiffer H, Aydin S, Schubert F, Ittermann B. Detection of metabolite changes in response to a varying visual stimulation paradigm using short-TE (1) H MRS at 7 T. NMR Biomed 2017;30(2).
55. Mangia S, Garreffa G, Bianciardi M, Giove F, Di Salle F, Maraviglia B. The aerobic brain: lactate decrease at the onset of neural activity. Neuroscience 2003;118(1):7-10.
56. Near J, Simpson R, Cowen P, Jezzard P. Efficient gamma-aminobutyric acid editing at 3T without macromolecule contamination: MEGA-SPECIAL. NMR Biomed 2011;24(10):1277-1285.
57. Violante IR, Ribeiro MJ, Edden RA, Guimaraes P, Bernardino I, Rebola J, Cunha G, Silva E, Castelo-Branco M. GABA deficit in the visual cortex of patients with neurofibromatosis type 1: genotype-phenotype correlations and functional impact. Brain 2013;136(Pt 3):918-925.

# Chapter 6

## SNR optimized $^{31}$P functional MRS to detect mitochondrial and extracellular pH change during visual stimulation

Arjan D. Hendriks,
Wybe J.M. van der Kemp,
Peter R. Luijten,
Natalia Petridou,
Dennis W.J. Klomp

*Submitted*

## Abstract

**Summary:** Energy metabolism of the human visual cortex was investigated by performing $^{31}$P functional MRS.

**Introduction:** The human brain is known to be the main glucose demanding organ of the human body and neuronal activity can increase this energy demand. In this study we investigate whether alterations in pH during activation of the brain can be observed with MRS, focusing on the mitochondrial inorganic phosphate (Pi) pool as potential marker of energy demand.

**Methods:** Six participants were scanned with 16 consecutive $^{31}$P MRSI scans at rest and during visual stimulation. Since the signals from the mitochondrial compartments of Pi are low, multiple approaches to achieve high SNR $^{31}$P measurements were combined. This included: a close fitting $^{31}$P RF coil, a 7T-field strength, Ernst angle acquisitions and a stimulus with a large visual angle allowing large spectroscopy volumes containing activated tissue.

**Results:** The targeted resonance downfield of the main Pi peak could be distinguished, indicating the high SNR of the $^{31}$P spectra. The peak downfield of the main Pi peak is believed to be connected to mitochondrial performance. In addition, a BOLD effect in the PCr signal was observed as a signal increase of 2-3% during visual stimulation as compared to rest. When averaging the data over multiple volunteers, a small subtle shift of about 0.1 ppm of the downfield Pi peak towards the main Pi peak could be observed in the first 4 minutes (2 scans), but no longer in the 4 to 8 minute scan window. Indications of a subtle shift in resonance frequency of the mitochondrial Pi peak during visual stimulation were found, but this effect remains small and should be further validated.

**Conclusion:** Overall, the down-field peak of Pi could be observed, revealing opportunities and considerations to measure specific acidity (pH) effects in the human visual cortex.

**Keywords:** $^{31}$P MRS, phosphor spectroscopy, fMRS, visual cortex, mitochondrial inorganic phosphate Pi, pH

## Introduction

The human brain consumes a considerable amount of energy, and is known to be the main glucose demanding organ of the human body [1]. Neuronal activity can increase this energy demand, and can cause local pH changes via several mechanisms [2,3]. So, studying energy metabolism in the human brain should provide a direct assessment of neuronal integrity and functioning.

$^{31}$P MR spectroscopy is often used to study energy metabolism in-vivo and non-invasively [4,5], for it can detect the energy products adenosine triphosphate (ATP), phosphocreatine (PCr), and inorganic phosphate (Pi). Moreover, using saturation transfer techniques, exchange rates between ATP and Pi can be determined [6], and acidity can be derived using the pH sensitive resonance position of the Pi signal. During muscle exercise, substantial alterations in PCr and Pi levels can be observed, as well as a clear shift of the frequency of the Pi signal that coincides with pH alteration. Even distinctions between Pi pools in mitochondrial, intracellular and extracellular compartments are visible due to their characteristic pH and thereby peak position in the $^{31}$P MR spectrum [7].

For several decades until now, no alterations of $^{31}$P MRS signal levels have been observed in the brain during activation, nor were alterations in pH observed, in contrast to the large activation-induced alterations of $^{31}$P MR signals in muscle. Under baseline hypoxia, neither the PCr/ATP and Pi/(Pi+ PCr) ratios nor intracellular pH levels in the brain were affected [8], despite the fact that blood oxygen saturation ranged from 0.95 to 0.83 reducing the blood's capacity to deliver $O_2$ to the brain as required for energy metabolism. Only chemical exchange rates during visual stimulation have been observed [6] and recently confirmed [9]. Obviously, the energy metabolism of the brain is strongly regulated and intracellular pH levels are controlled, for example through buffer processes such as the $CO_2/HCO_3^-$ system. Because of these regulatory mechanisms, the magnitude of the neuronal activity induced pH changes is very small, so with MRS it could possibly only be detected as a small shift in peak frequency or minimal change in peak amplitude of Pi. A subtle shift in the intracellular Pi peak or amplitude alteration would be challenging to observe, as the $^{31}$P MRS peaks will get narrower line widths and higher amplitudes during stimulation caused by BOLD effects. Moreover, signals of 2,3-DPG (2,3-diphosphoglycerate) from blood may contaminate the spectrum as demonstrated in cardiac MRS, as these have resonances close to the Pi peak [10,11].

In our study, we propose an alternative means to observe alterations in pH during activation of the brain. Rather than focusing on the total observed Pi pool, which is predominantly intra cellular, our study aims to observe pH alterations in the mitochondria. Distinction between mitochondrial Pi and intracellular Pi is possible due to their different acidic environments: pH of 7.8 in mitochondria (at rest) [12] versus 7.05 of the intracellular pool [13]. When the

chemical shift of PCr is normalized at 0 ppm, Pi at a pH of 7.8 would correspond to a chemical shift of 5.5 ppm, and Pi at a pH of 7.05 would correspond to 4.9 ppm. The spectral resolution is more than sufficient at a field strength of 7T to distinguish these two signals that have a chemical shift difference of 0.6 ppm (i.e. similar difference for phosphocholine (6.2 ppm) and phosphoethanolamine (6.8 ppm) that have demonstrated clear distinction at 7T) [14].

However, the pool size of Pi in mitochondria is substantially less than intracellular Pi, therefore the signal to noise ratio (SNR) has to be increased. With the use of SNR optimized RF coils for calf muscle $^{31}$P MRS at 7T, it has been demonstrated that the mitochondrial Pi pool reflects about 13% of the total observed intracellular Pi pool [7]. In fact, when taking a closer look at the first $^{31}$P spectra obtained from the human brain at 7T [15], a small peak down-field from the main Pi peak can be observed, albeit not labeled by the authors as such. Consequently, when optimizing SNR of $^{31}$P MRS in the human brain, the mitochondrial Pi pool may be detected.

The SNR of the mitochondrial Pi signal can be improved at 7T in several steps. First, the volume of activated tissue can be enlarged. A large volume of activated tissue would enable the use of a large spectroscopy voxel size, resulting in an additional increase in SNR similar as recently observed for enlarged voxel measurements of γ-aminobutyric acid (GABA) using a setup with a large visual angle [16]. Secondly, the RF coil can be optimized for higher SNR. Using a tight-fit volume resonator, a uniform excitation can be obtained while assuring highest SNR in the center of the brain [17]. Moreover, when compared to surface coil transceivers, the uniform reception will reduce potential contamination from $^{31}$P signals from the large vessels close to the skull. Finally, it was demonstrated that the $T_1$ relaxation time of mitochondrial Pi is about four-fold shorter than intracellular Pi [7], therefore short TR sequences can be used that maximize the SNR per unit of time.

In this study, the above mentioned SNR optimization steps were implemented to investigate the behavior of the downfield Pi peak in the human brain of six healthy volunteers during visual stimulation.

## Methods

Six participants (5 male, 1 female, 24-43 year old) were scanned in a 7T Achieva system (Philips, Best, the Netherlands). The first participant was scanned twice: first to test the setup and scan protocols, and second to acquire data with an identical scan protocol as for the rest of the participants. All participants provided written informed consent, and the study was approved by the medical ethics committee of the University Medical Center Utrecht.

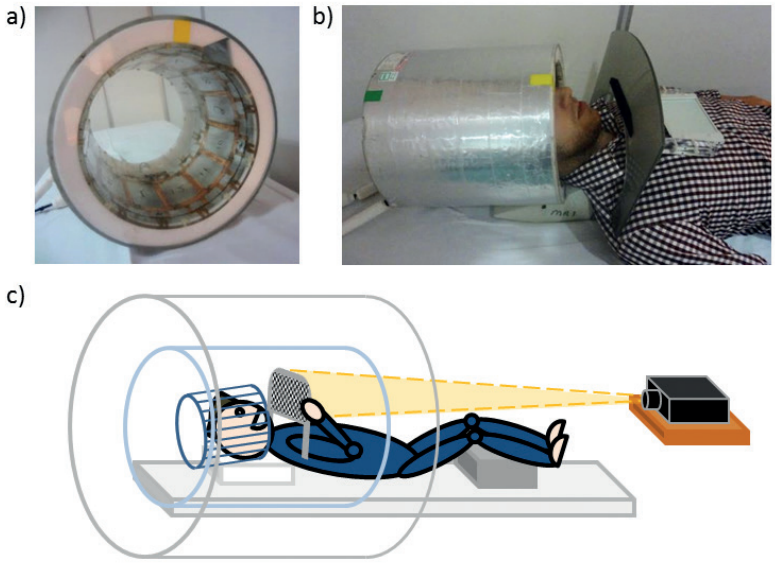


**Figure 25: The coil setup, which is equipped with a screen for visual stimulation. Displayed are (a) a photograph of the $^{1}$H-$^{31}$P transmit-receive coil, (b) a photograph of the coil when the screen is mounted and (c) a schematic overview of setup during signal acquisition. Note that no mirrors and/or prism glasses are required for this setup, which enhances the visual angle of view with respect to the projected stimulus.**

A dedicated custom coil setup was used with a large screen for projection of a stimulus with a large visual angle (Figure 25). The visual angle was around 40 degrees in height and more than 70 degrees in width. The transmit/receive coil used was a tight fit (inner diameter = 23 cm), shielded quadrature birdcage coil, double tuned to both the $^{1}$H and $^{31}$P frequency. Ceramic floating cable traps tuned for $^{31}$P and $^{1}$H were used in series for both cables that run from the $^{1}$H and $^{31}$P coil, via an RF splitter, to the narrow band transmit receive switches, quadrature hybrids and preamplifiers of the MRI system.

$B_0$ shimming of the visual cortex was performed by acquiring a 3D $B_0$ map, and subsequently updating the currents in the shim coils with the calculated values from the first and second order harmonics that fit to the $B_0$ maps. The $B_0$ maps were obtained with TE = 1.54 ms, delta TE = 1 ms, TR = 4 ms, FOV = 240x180x157 mm$^3$, spatial resolution = 3.75x3.75x3.75 mm$^3$, and a total scan time of 16.2 sec. After $B_0$ shim updating, the water frequency was determined from the visual cortex using the standard semi-LASER sequence implemented by the vendor [18]. The frequency was used to fix the carrier frequency of the $^{31}$P MR system during the remainder of the scan session.

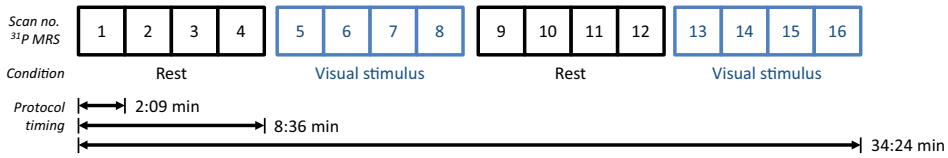


**Figure 26: Overview of the scan protocol for the $^{31}$P MRS scans. Sixteen $^{31}$P MRS scans of 2:09 minutes are acquired in 6 participants. Visual stimuli were projected in blocks of 4 scans (4 rest, 4 stimulus, 4 rest, 4 stimulus). In total, the $^{31}$P MRS scans had a duration of 34:24 minutes.**

A pulse-acquire $^{31}$P MR sequence was used and configured with a short TR of 100 ms to obtain highest SNR per unit of time, while providing an acquisition window of 80 ms (512 datapoints at 6400 Hz) and a spectral resolution of 0.1 ppm. An Ernst-angle of 20 degrees was used, based on the estimated shortened $T_1$ value of mitochondrial Pi of 1.4 sec, as obtained from literature [7]. The excitation pulse duration was set to 109 µs, and the pulse was amplified using the 4kW RF amplifier of the MR system. $B_0$ gradient phase encoding steps of 400 µs were included to the sequence to provide 3D MR Spectroscopic Imaging (MRSI) in order to spatially distinguish the $^{31}$P MR spectrum of the stimulated visual cortex from the remainder of the brain (280x280x280 mm$^3$ FOV, matrix size 8x8x8, 35x35x35 mm$^3$ voxelsize). Hamming weighted averaging was applied with 6 averages of the center of k-space resulting in a scan-shot of 2:09 minutes. For each participant a total of 16 consecutive $^{31}$P MRSI scans were acquired.

Visual stimuli were projected in blocks of 4 scans (4 rest, 4 stimulus, 4 rest, 4 stimulus), as is shown in Figure 26. The visual stimulus consisted of a contrast reversing pattern at 8 Hz, which was comprised of curved-lines oriented in different directions, targeted to stimulate a big pool of neurons with varying orientation preference [19]. The stimulus was presented for 8:36 min (4 scans) and was repeated after a rest period. The first subject was scanned twice to test the scan protocols. In the first session of the first subject a standard contrast reversing checkerboard at 8 Hz was used as visual stimulus. In the second session an identical visual stimulus was used as for the rest of the participants.

After scanning, in post processing steps, the data was Hamming filtered in spatial domain and 1 voxel located in the visual cortex was selected from each 3D MRSI scan. The resulting spectra were phased using a fixed first order phase setting corresponding to the delay of 503 µs between the center of excitation and the center of the first acquired data point. Manual zero order phasing was performed and fixed to the same setting for all spectra obtained from the same participant. Next, datasets were zerofilled to 4096 data points, apodized to 10Hz, aligned to PCr and averaged in three ways:
First, four sets of 4 spectra were averaged for each individual participant (i.e. 4 rest, 4 stimulus, 4 rest and 4 stimulus). From these averaged spectra, the BOLD effect to PCr is assessed by plotting the PCr peak over time. Second, the 16 individual consecutive scans were averaged

over the 6 participants to assess temporal behavior of the mitochondrial Pi pool and pH. Matching blocks of either rest or stimulation were averaged to visualize the first 2 minutes, second 2 minutes and end of the stimulation block, to investigate possible dynamic changes of metabolites during the experiment. Third, all spectra were averaged per stimulation block over all participants. The relative amplitude of the mitochondrial Pi peak as compared to the main intracellular Pi peak was assessed using Lorentzian line fitting (jMRUI version 3.0) with fixed prior knowledge on peak position and line width.

## Results

All included participants fitted in the RF coil and reported full visual view of the screen. In one participant the large visual field of view for visual stimulation is shown (Figure 25). The duration of the preparation steps such as planning and $B_0$-shimming took less than 10 minutes, starting from the moment the participant was inside the MRI until the start of the first dynamic $^{31}$P MRSI scan. In one of the 6 participants, the automatic frequency determination was off during the preparation steps, thereby causing an off resonance of 1 kHz as compared to the spectra acquired from the other participants. As this offset is well within the bandwidth of the 109 µs RF excitation pulse (9.2 kHz), the dataset was still included in all analyses.

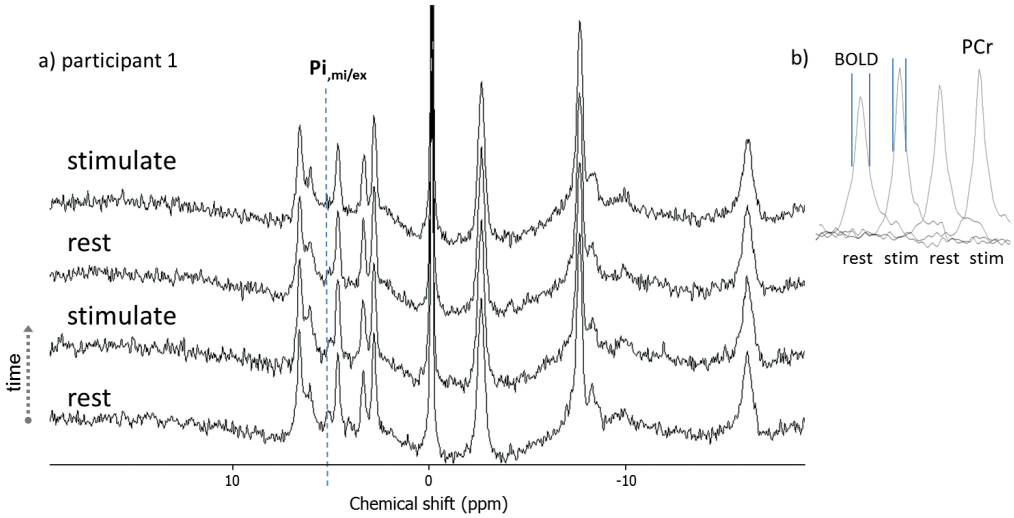


**Figure 27: $^{31}$P MR spectra from the first scan session of the first participant. These spectra are obtained during rest and during visual stimulation with a checkerboard reversing contrast at 8Hz. Each spectrum is an average of 4 consecutive scans of 2 minutes. A clear peak downfield from the intracellular Pi peak is indicated by the striped line (a). Upon closer inspection of the $Pi_{,mi/ex}$ peak, a small shift in frequency can be observed, particularly when comparing the first rest spectrum (bottom) with the first stimulus spectrum (second from the bottom). In addition, when comparing the rest spectra with the stimulus spectra, a line narrowing of the PCr peak can be observed reflected as ≈15% increase in PCr amplitude during stimulus (b).**

In the first scan session of the first participant, the scan protocol was tested revealing a clear resonance downfield of the main Pi peak (Figure 27a) indicating that the $^{31}$P spectra have a high SNR. Lorentzian fits of the two Pi peaks indicated that the signal integral of the downfield peak was 0.20 times the signal integral of the main Pi peak. Upon closer inspection, the frequency of the intracellular Pi peak at 4.85 ppm corresponding to a pH of 7.01 did not shift, while the mitochondrial Pi peak shifted at max 0.1 ppm up field during visual stimulation, corresponding to a shift in pH from 7.55 to 7.41. In addition, a clear BOLD effect in the PCr signal was observed, reflected as a signal increase of approximately 15% when comparing the spectra obtained during rest with the ones obtained during visual stimulation with the contrast-reversing checkerboard (Figure 27b).

As the temporal resolution of the MRSI scans was 2 minutes, while rest and stimulation periods were 8 minutes, dynamic alterations of $^{31}$P metabolites within the stimulation period can be investigated. In order to maximize SNR, data was averaged not only from all participants, but also from both rest and both stimulation events. Again, a subtle shift of about 0.1 ppm of the

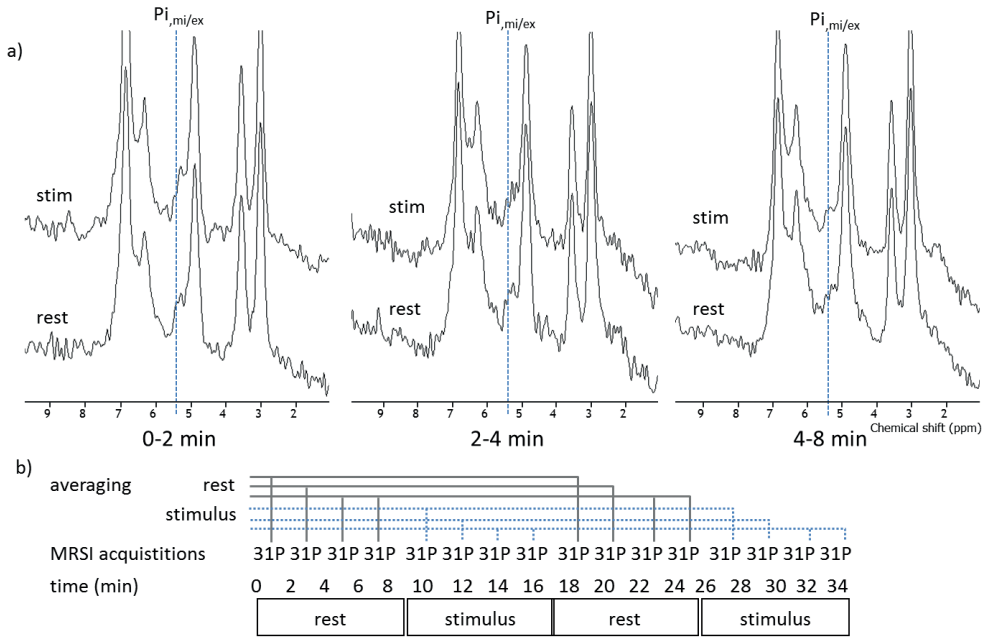


**Figure 28: Dynamic $^{31}$P MR spectra from visual cortex (a) averaged (b) over all six participants. The spectra are obtained during rest and visual stimulation at a temporal resolution of 2 minutes. In the spectra obtained in the first two minutes, as well as the spectra obtained in the second 2 minutes, a shift or line splitting of the $Pi_{,mi/ex}$ peak can be observed during visual stimulation when compared to the corresponding rest spectra. The shift is not observed in the averaged spectra of the final 4 minutes of activation when compared to rest.**

downfield Pi peak towards the main Pi peak can be observed in the first 2 minutes as well as in the second 2 minutes scan, but no longer in the 4 to 8 minute scan window (Figure 28).
In the $^{31}$P spectra of the individual participants, the downfield Pi peak is visible in 5 out of 6 participants (Figure 29). The SNR of these spectra is not sufficient to detect a 0.1 ppm shift of the Pi peak over time. In one participant the carrier frequency was off, thereby missing the β-ATP peak, yet the SNR of the remaining peaks remained similar when compared to the SNR of the $^{31}$P MR spectra from the other participants.

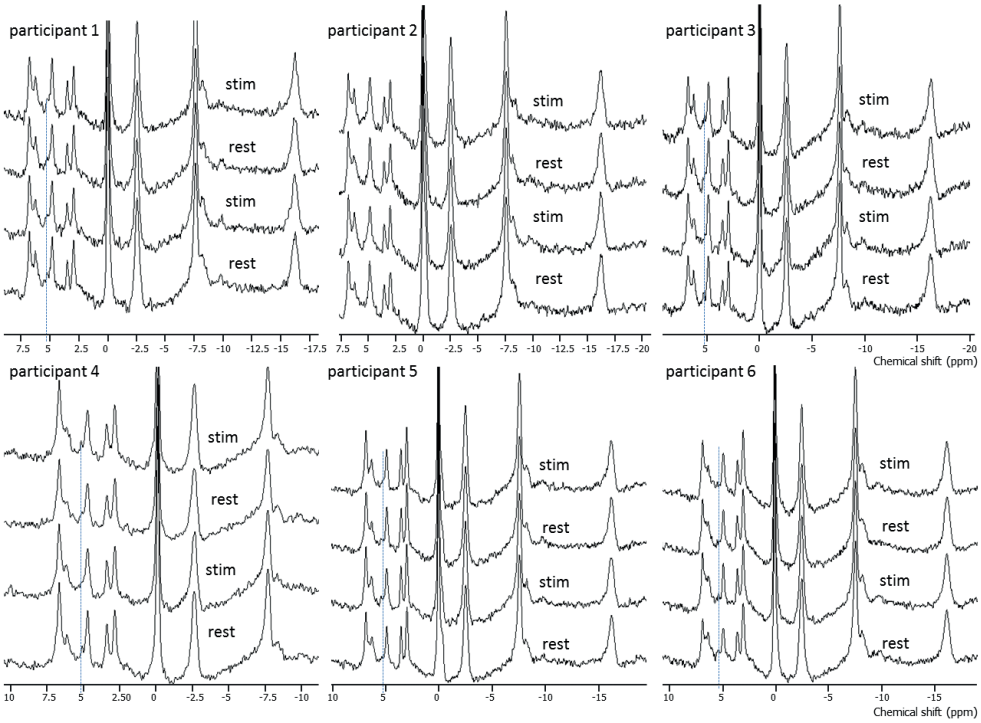


**Figure 29: $^{31}$P MR spectra of all participants individually. The spectra are acquired dynamically from the visual cortex of the brain during rest (lower), stimulus (second), rest (third) and stimulus (upper). The $Pi_{,mi/ex}$ peak downfield from the $Pi_{,i}$ peak is clearly visible in participant 1, 3, 4, 5, and 6, highlighted by the striped line. Note that for participant 4 the spectra are not fully displayed (no β-ATP peak), due to a 1 kHz offset during acquisition.**

In the $^{31}$P MRS datasets of the individual participants, the BOLD effect on the PCr peak was not clearly observed, however, when averaging over all participants, the signal intensity increased 2-3% during stimulation as compared to rest (Figure 30, inset). The alignment of the spectra between participants facilitated averaging spectra over participants, while maintaining the detection of the downfield peak of Pi (Figure 30). When comparing the averaged spectra of

Figure 30 with Figure 27, clearly the SNR is improved. Likewise, line broadening, a subtle shift or even peak splitting of the downfield Pi peak over time can be observed of less than 0.1 ppm.

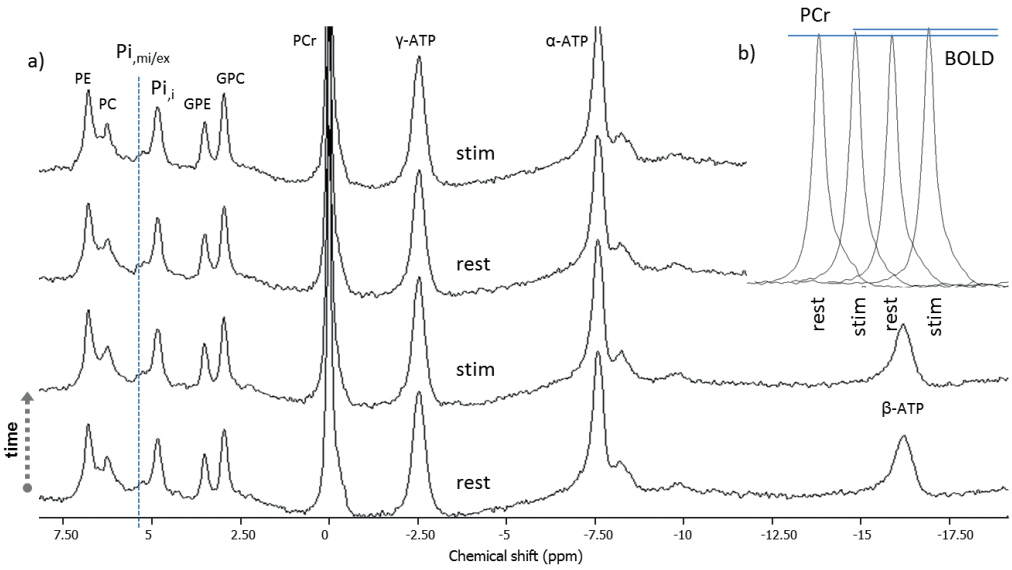


**Figure 30: $^{31}$P MR spectra averaged over all six participants during blocks of rest, visual stimulation, rest and stimulation of each 8 minutes long. The high SNR shows the mitochondrial/extracellular $Pi_{,mi/ex}$ peak downfield from the intracellular $Pi_{,i}$ peak as indicated by the striped line (a). Line broadening, a small shift in frequency or even peak splitting of the $Pi_{,mi/ex}$ peak can be observed when comparing the spectra over time. However, this effect is less prominent as compared to the effect in the spectra of individual participants (Figure 27) or the temporally averaged spectra (Figure 28). In addition, when comparing the rest spectra with the stimulus spectra, a BOLD effect reflected as a 2-3% increase in PCr during visual stimulation can be observed (b).**

## Discussion and conclusion

The energy metabolism of the visual cortex was investigated with $^{31}$P MRS during visual stimulation with a large visual angle. Consequently, the spatial resolution could be reduced, or the voxel size increased to the enlarged stimulated area, in return for higher SNR and temporal resolution of the dynamic $^{31}$P MRSI exams. Combined with Ernst-angle acquisitions, and a close fitting RF coil, a clear resonance downfield from the intracellular Pi peak can be observed within a temporal resolution of 2 minutes. Moreover, during visual stimulation, a subtle shift of at most 0.1 ppm of this peak can be observed, corresponding to a pH shift of −0.13 units when assigning the peak as Pi from either the mitochondria or the extracellular space.

In this study we incorporated a relatively large voxel volume to obtain the SNR required to detect the down-field Pi peak. In addition, averaging over participants was another means to increase SNR, by using peak alignment of the large signal of PCr. This enabled studying

subtle effects in peak position and line width at relatively high temporal resolution. Temporal resolution may be important, considering the possible saturation or habituation effects with the prolonged stimulation employed here. In fact, the shift in the downfield peak of Pi seems better visible in the first two minutes of activation than in the final 4 minutes of activation. In line with this finding, when averaging over the full block of 8 minutes for all participants, the difference between the rest and stimulus condition is less prominent. Still for the spectra of some individual participants and for the average over all participants a small shift in frequency, line broadening or even peak splitting of the $Pi_{,mi/ex}$ is observed. These effects remain subtle and should therefore be further validated.

While it has been shown that receiver arrays could enhance SNR, large volumes deeper in the brain may benefit more from the use of a volume transceiver due to inherent RF phase destructions within the voxel. Some gain in SNR may be found when obtaining a proper assessment of the $T_1$ of the downfield Pi spins in the brain to further optimize the Ernst angle. Most improvements in SNR can be achieved when going to higher magnetic fields, such as 9.4T or in the near future to even higher field strengths.

Studies that use other approaches to measure pH changes in the brain, such as amide proton chemical exchange saturation transfer (APT-CEST), show that it is challenging to measure pH and that the expected pH differences could be smaller than 0.03 pH units [20]. However, the APT-CEST contrast is believed to predominantly originate from intracellular amides. In the current study it was aimed to specifically measure the pH in mitochondrial or extracellular compartments, so pH changes due to activation could be different there.

Although we have assigned the downfield Pi peak as mitochondrial Pi, it is expected to be composed of several other compounds as well. For instance, 2,3-DPG is highly abundant in blood and expresses itself at 7T as two peaks in close proximity to the resonance of Pi and phosphocholine (PC). The absence of this peak in calf muscle was relatively simple to address, as PC levels are much lower in muscle therefore easier to identify the double 2,3-DPG peaks if they were above the noise floor. We have used phase encoding gradients and Hamming filtering to localize the voxel from the visual cortex, which due to point spread function and partial volume effects may still incorporate some signals from blood vasculature. Further reduction of the chance to include signals from highly abundant vasculature close to the skull may be realized when using outer volume suppression by means of a crusher coil [21]. Another possibility could be that the signal comes from extracellular Pi at a much higher pH level than the intracellular Pi, or similar pH level as the mitochondrial Pi. Diffusion weighted spectroscopy may be applied to reduce the content from extracellular Pi. It should be noted that these diffusion techniques require stronger gradients considering the lower gyromagnetic ratio of $^{31}$P over $^{1}$H, and that SNR will go down.

We have shown that even with very high SNR and strong visual stimulation, energy metabolite levels remain highly intact. Yet, over 2 minutes of activation a subtle pH shift from 7.55 to 7.41 can be observed when assigning the downfield peak of Pi as mitochondrial or extracellular Pi. This drop in pH matches observations of lactate increase, as reported with $^{1}$H MRS before [3]. However, considering the substantial BOLD effect reflecting local alterations in oxygenation and high levels of glucose consumption of the brain, stronger effects in $^{31}$P signals would be expected in close proximity to the neurons. The large voxel in our study will lead to partial volume effects of grey and white matter, which in total may have the buffering capacity to maintain the energy metabolite levels and environment constant. Longer and stronger activation strategies can be applied to study this buffer capacity. Or, when higher fields become available, reduced voxel sizes may be used to maximize neuron density, which in that case can be helped by receiver arrays to provide the required SNR.

In conclusion, energy metabolism of the human visual cortex was investigated by performing $^{31}$P functional MRS. We focused on the mitochondrial inorganic phosphate pool as potential marker of energy demand. The targeted resonance downfield of the main Pi peak could be distinguished, indicating the high SNR of the $^{31}$P spectra. Additionally, a BOLD effect in the PCr signal was observed. A small subtle shift of about 0.1 ppm of the downfield Pi peak towards the main Pi peak could be observed, especially in the first 4 minutes. When averaging over larger time periods the results were less prominent, indicating a time dependency. The effects are subtle and should be further validated. Overall, this study revealed potential opportunities to measure activation evoked changes in specific acidity (pH), but also emphasizes the need for higher SNR measurements to be able to study these processes in more detail.

## References


1. Mergenthaler P, Lindauer U, Dienel GA, Meisel A. Sugar for the brain: the role of glucose in physiological and pathological brain function. Trends Neurosci 2013;36(10):587-597.
2. Chesler M. Regulation and modulation of pH in the brain. Physiol Rev 2003;83(4):1183-1221.
3. Magnotta VA, Heo HY, Dlouhy BJ, Dahdaleh NS, Follmer RL, Thedens DR, Welsh MJ, Wemmie JA. Detecting activity-evoked pH changes in human brain. Proc Natl Acad Sci U S A 2012;109(21):8270-8273.
4. Prompers JJ, Jeneson JA, Drost MR, Oomens CC, Strijkers GJ, Nicolay K. Dynamic MRS and MRI of skeletal muscle function and biomechanics. NMR Biomed 2006;19(7):927-953.
5. Valkovic L, Chmelik M, Krssak M. In-vivo $^{31}$P-MRS of skeletal muscle and liver: A way for non-invasive assessment of their metabolism. Anal Biochem 2017;529:193-215.
6. Chen W, Zhu XH, Adriany G, Ugurbil K. Increase of creatine kinase activity in the visual cortex of human brain during visual stimulation: a $^{31}$P magnetization transfer study. Magn Reson Med 1997;38(4):551-557.
7. Kan HE, Klomp DW, Wong CS, Boer VO, Webb AG, Luijten PR, Jeneson JA. In vivo $^{31}$P MRS detection of an alkaline inorganic phosphate pool with short T1 in human resting skeletal muscle. NMR Biomed 2010;23(8):995-1000.
8. Vidyasagar R, Kauppinen RA. $^{31}$P magnetic resonance spectroscopy study of the human visual cortex during stimulation in mild hypoxic hypoxia. Exp Brain Res 2008;187(2):229-235.

9. Chen C, Stephenson MC, Peters A, Morris PG, Francis ST, Gowland PA. $^{31}$P magnetization transfer magnetic resonance spectroscopy: Assessing the activation induced change in cerebral ATP metabolic rates at 3 T. Magn Reson Med 2018;79(1):22-30.
10. Rodgers CT, Clarke WT, Snyder C, Vaughan JT, Neubauer S, Robson MD. Human cardiac $^{31}$P magnetic resonance spectroscopy at 7 Tesla. Magn Reson Med 2014;72(2):304-315.
11. van der Kemp WJM, Klomp DWJ, Wijnen JP. $^{31}$P T2 s of phosphomonoesters, phosphodiesters, and inorganic phosphate in the human brain at 7T. Magn Reson Med 2018;80(1):29-35.
12. Porcelli AM, Ghelli A, Zanna C, Pinton P, Rizzuto R, Rugolo M. pH difference across the outer mitochondrial membrane measured with a green fluorescent protein mutant. Biochem Biophys Res Commun 2005;326(4):799-804.
13. Vorstrup S, Jensen KE, Thomsen C, Henriksen O, Lassen NA, Paulson OB. Neuronal pH regulation: constant normal intracellular pH is maintained in brain during low extracellular pH induced by acetazolamide--$^{31}$P NMR study. J Cereb Blood Flow Metab 1989;9(3):417-421.
14. van der Kemp WJ, Stehouwer BL, Runge JH, Wijnen JP, Nederveen AJ, Luijten PR, Klomp DW. Glycerophosphocholine and Glycerophosphoethanolamine Are Not the Main Sources of the In Vivo $^{31}$P MRS Phosphodiester Signals from Healthy Fibroglandular Breast Tissue at 7 T. Front Oncol 2016;6:29.
15. Lei H, Zhu XH, Zhang XL, Ugurbil K, Chen W. In vivo $^{31}$P magnetic resonance spectroscopy of human brain at 7 T: an initial experience. Magn Reson Med 2003;49(2):199-205.
16. Hendriks AD, Fracasso A, Arteaga de Castro CS, Gosselink M, Luijten PR, Petridou N, Klomp DWJ. Maximizing sensitivity for fast GABA edited spectroscopy in the visual cortex at 7 T. NMR Biomed 2018;31(4):e3890.
17. Klomp DW, van der Graaf M, Willemsen MA, van der Meulen YM, Kentgens AP, Heerschap A. Transmit/receive headcoil for optimal 1H MR spectroscopy of the brain in paediatric patients at 3T. MAGMA 2004;17(1):1-4.
18. Scheenen TW, Heerschap A, Klomp DW. Towards 1H-MRSI of the human brain at 7T with slice-selective adiabatic refocusing pulses. MAGMA 2008;21(1-2):95-101.
19. Kay KN, Winawer J, Rokem A, Mezer A, Wandell BA. A two-stage cascade model of BOLD responses in human visual cortex. PLoS Comput Biol 2013;9(5):e1003079.
20. Khlebnikov V, Siero JCW, Bhogal AA, Luijten PR, Klomp DWJ, Hoogduin H. Establishing upper limits on neuronal activity-evoked pH changes with APT-CEST MRI at 7 T. Magn Reson Med 2018;80(1):126-136.
21. Boer VO, van de Lindt T, Luijten PR, Klomp DW. Lipid suppression for brain MRI and MRSI by means of a dedicated crusher coil. Magn Reson Med 2015;73(6):2062-2068.

# Chapter 7

## General discussion

## General discussion

In this thesis the overall aim was to maximize the SNR, temporal resolution and spatial resolution of BOLD fMRI and MRS techniques to be able to gain further insight into the hemodynamics and metabolism of the human brain. This aim was pursued in five different approaches (chapters), which can roughly be divided in two parts.

The first part of this thesis shows that it was possible to reduce scan time of high resolution EPI scans intended for BOLD fMRI measurements. A shot selective 2D CAIPIRINHA implementation was developed, which enhanced the image quality and reduced the scan time of sub-millimeter 3D EPI scans of the visual cortex. It also enabled the acquisition of sub-millimeter 3D EPI scans with a sub-second temporal resolution (**Chapter 2**). Succeeding simulations showed that the use of a 256 channel receive coil array could potentially reduce scan time further. The estimated maximum acceleration factor, as compared to a 32 channel coil, went from 9 to 24 using SENSE and from 12 to 28 using CAIPIRINHA (**Chapter 3**). In addition, a novel idea was presented to push the spatial and temporal resolution of EPI scans by the use of ultrasonic switching gradients, as described in a patent (**Chapter 4**).

The second part of this thesis shows that it was possible to improve functional brain measurements that target (neuronal) metabolism using MRS. Neurotransmitter levels of GABA could be measured with GABA edited spectroscopy scans, which had a duration of less than 1:23 minutes. This was achieved using a specially built half volume coil setup with a wide screen for visual stimulation (**Chapter 5**). The same principle of using a visual stimulation with a large visual angle was then applied to measure energy metabolism of the brain with dynamic $^{31}$P MRS. This could potentially further extend the toolbox of MR techniques to study brain functions (**Chapter 6**).

### Main applications

The proposed approaches described in previous chapters lead to an increased temporal and spatial resolution for BOLD fMRI, and an increased SNR and shorter dynamic scan time for metabolic MRS. This brings new opportunities for the field of neuroscience.

The improved spatial resolution allows BOLD fMRI studies to map the human cortex with high detail. This includes high resolution mapping of sensory and motor systems in for example retinotopy, tonotopy and somatotopy at a columnar or laminar level. It opens up possibilities to probe layer-specific hemodynamics and neurovascular coupling mechanisms in the cortex [1]. The overall target is to push the resolution to the fine spatial scale of cortical micro-circuits that perform the brain's fundamental processing tasks. These circuits consist of small groups of neurons forming detailed cortical structures on the order of micrometers to a few millimeters thick. Being able to measure at such scales, enables us to gain fundamental knowledge on how the brain works.

Improved temporal resolution (or short dynamic scan time) allows us to further explore specific time dependent characteristics of the BOLD response. Temporal characteristics of the

hemodynamic BOLD response can help to target neuronal processes and neuronal vascular coupling relationships across cortical layers, for example by differences in the start (onset times) of the BOLD response across cortical depth. Recent studies from animal research show that the BOLD onset arrives earliest in layer 4 of the somatosensory cortex, matching neural inputs [2]. Similarly, further improved temporal resolution of BOLD fMRI scans in humans, might eventually allow us to further determine the temporal order of neuronal events and the neuronal communication pathways in the human brain [3,4].

To give an initial example of improved temporal and spatial resolution for fMRI, a recent application of the shot selective 2D CAIPIRINHA approach of this thesis can be found in the preliminary results shown in Figure 31, where both temporal and spatial resolution are pushed, while maintaining sufficient SNR. High density receive arrays and the shot selective 2D CAIPIRINHA sequence were combined to perform enhanced BOLD fMRI imaging of the visual cortex during visual stimulation. Major improvements in SNR were achieved, as compared to a SENSE scan with the same resolution and scan time. This resulted in better detectable BOLD fMRI signals relating to neuronal activation. Even better imaging performance can potentially be achieved, when combining this method with the other approaches described in this thesis.

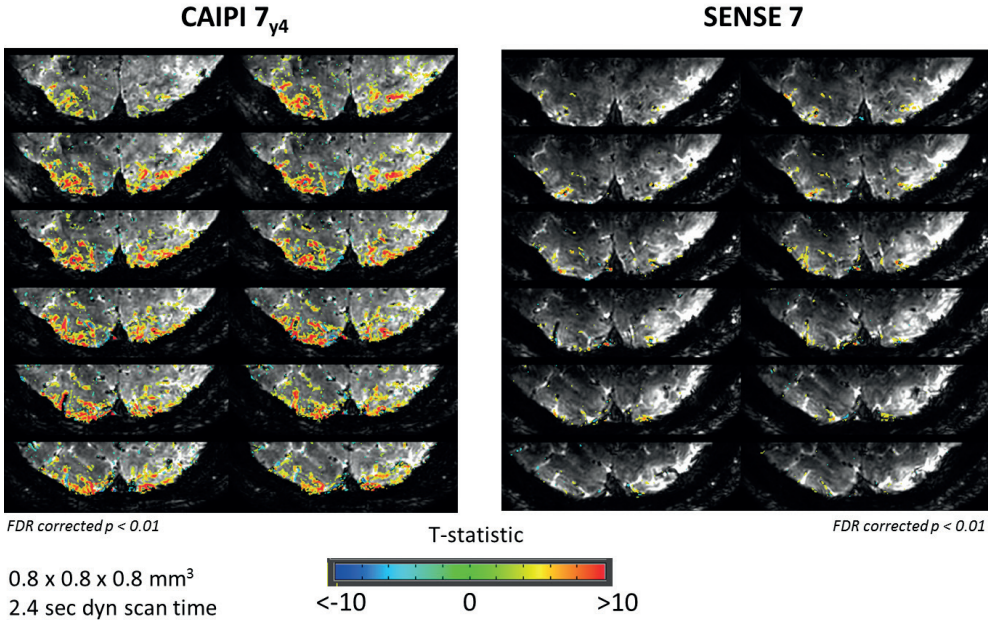


**Figure 31: A BOLD fMRI application of the shot selective 2D CAIPIRINHA approach using high density receive arrays. Multiple slices of the visual cortex are displayed for acquisitions at 0.8 mm isotropic resolution using both CAIPIRINHA and SENSE. A checkerboard that reversed contrast at 8 Hz was used as visual stimulus. Note that the detected amount of activated voxels in the brain is much larger for the CAIPIRINHA dataset than the SENSE dataset, due to an increase in SNR. Both datasets were 3D EPI scans with 0.8 mm isotropic voxelsize, TR/TE of 57/28, a 2.4 second dynamic scan time and a total scan time of 4 minutes. fMRI data was FDR corrected (p<0.01), the displayed background image is the mean of the EPI series.**

The reduced dynamic scan time for MR spectroscopy brings us a step further towards functional measurements of (neuronal) metabolism in individuals. The knowledge from these measurements would be complementary to the existing vascular oriented MRI methods, such as BOLD fMRI. The fast scan time for GABA edited MRS of 1:23 minutes in this work, makes it possible to start initial exploratory studies to measure individual GABA levels over time, during visual stimulation and rest. Later, when potentially higher temporal MRS resolutions are achieved, this method can be used to study brain function from a metabolic perspective, in addition to the existing vascular based BOLD fMRI methods. At the moment there is still an order of magnitude difference in temporal resolution between these methods with a scan time of minutes for edited MRS and seconds for BOLD fMRI.
The increase in SNR for $^{31}$P allows for improved measurements of energy metabolism in the human brain. It was possible to distinguish signals from different compartments of inorganic phosphate at a cellular level. Direct applications to study different brain functions through pH measurements with $^{31}$P MRS are not feasible at the moment, though promising applications might lie ahead when this method further advances in the future.

## Considerations and open points

The approaches outlined in this thesis made it possible to increase spatial and temporal resolution of MRI and MRS methods. This is a step in the right direction, though not the end of the line, especially considering the wide range of new developments in the MRI field.
One could argue the choice in this thesis to measure brain function by using two techniques that appear to be very different, being BOLD fMRI and MR spectroscopy. Indeed, the techniques are different when looking from a pure methodological perspective. However, in this thesis, these seemingly different MR techniques have a very similar purpose. Both techniques try to capture functional changes in the brain over time. Where BOLD fMRI tries to measure neuronal activity by measuring changes in hemodynamics, MR spectroscopy measures similar functional behavior of the brain, but by quantifying the concentrations of underlying (neuronal) metabolites.
The transition to sub-millimeter resolution imaging also brings high demands on the measurement setup. It is unrealistic to expect a human volunteer to lay still in the MR scanner for half an hour with sub-millimeter precision. Therefore accurate motion correction techniques, either during acquisition or post processing, are essential and will become more prominent in future applications.
With this work and the ongoing drive to advance MRI technology, it becomes increasingly possible to achieve sub-millimeter voxel sizes with sub-second sampling rates, high SNR, and a large volume coverage of brain. However, as the spatial and temporal resolution of BOLD fMRI increases, the unavoidable question arises: How far can this be pushed? Is our ability to map dynamic and detailed cortical structures with fMRI limited by the instrumental resolution or by the “biological” resolution? In other words, are we limited by the spatial and temporal

sampling we can achieve with advanced MRI systems, or by the spatial and temporal specificity of the hemodynamic signals utilized in fMRI? At a certain point the biological detail of the hemodynamic signals and the brain's ability to locally regulate changes in blood flow might become coarser than the upcoming achievable high resolution with MRI scanners. This would question the aim to further pursue fast and high resolution MR imaging. However, recent studies using optical imaging methods have demonstrated that blood flow regulation occurring in response to neuronal activity is far more precise than previously believed, suggesting that responses may be localized within individual cortical columns or layers [5-7]. Nevertheless, currently the ultimate achievable resolution by fMRI is still unknown [8,9]. While a range of cellular mechanisms, including astrocytes, pericytes, and interneurons, have been proposed to play a role in functional neurovascular coupling, the key spatiotemporal features of BOLD response remain unexplained [10].

## Alternative applications of the developed techniques

In this thesis the improved techniques are mainly applied to the field of functional brain imaging and spectroscopy. However, the benefits of the improved methods have a broader field of application and can be used for other purposes as well. For example, instead of brain function, the developed shot selective 2D CAIPIRINHA implementation for 3D EPI scans (as described in **Chapter 2**) can be used for fast and high resolution scanning of clinical brain anatomy as well. A whole brain $T_2$* weighted 3D EPI scan with a high resolution of less than 1 mm is typically not performed in clinical routine, since the protocol takes too much time. With the exception of scan duration, such scans would be very useful and of clinical value, for example for patients with amyotrophic lateral sclerosis (ALS) where small hypointensities can be observed in the deep layers of the primary motor cortex [11,12]. Previously, the duration of these 0.5 mm isotropic $T_2$* weighted 3D EPI scans was 10 minutes without acceleration and 6 minutes with traditional SENSE acceleration [13]. As shown in this thesis, the 2D CAIPIRINHA implementation can shorten the duration of these scans significantly, resulting in a scan time of 1.5 minutes, making this scan practical and clinically realistic.

The simulations in **Chapter 3** show that it is possible to accelerate even more by using a 256 channel receive array for the head. This applies to a broader range of scans, but the greatest improvement can be achieved with MRI protocols that focus on the cortex of the brain, since the achievable acceleration factor is the highest for these areas.

The novel idea of an ultrasonic switching gradient system (**Chapter 4**) can not only be used to reduce scan time, but could also be used to create a "silent" MRI scanner. Traditionally gradients are driven in the auditory range, generating the typical loud noise of the MRI scanner. An ultrasonic switching gradient system is driven above auditory range, making gradient vibrations in theory inaudible.

The spectroscopy studies in **Chapter 5 and 6** are optimized for high temporal performance by maximizing SNR per unit of time. The developed multi-transmit half volume coil setup, as well

as the concept of a large screen for a visual activation with a large visual angle, are not solely applicable to MRS, but are also valuable for BOLD fMRI studies that target the visual cortex.

## Other approaches in literature

There are other approaches, as described in literature, to be able to perform MRI scans of the human brain with a high spatial resolution and a high temporal resolution.
An integrated approach can be found in several projects such as the currently running project MR Corticography (MRCoG) of Feinberg et al. [14], where multiple strategies (similar to those described in this thesis) will be combined at 7T to image the brain's cortex on the meso-scale. High density receiver arrays with 128 coil elements will be combined with high performance gradients and recently developed pulse sequences to produce high acceleration factors for EPI images. Those studies expect to achieve a higher spatial resolution (of around 0.4 mm) than the resolution of current 7T scanners [15].
The most commonly used technique for functional imaging is BOLD. However, there are other approaches to map functional activity of the human brain. In this thesis, in addition to BOLD, the neurotransmitter GABA and the pH sensitive metabolite inorganic phosphate are measured as well. In literature, alternative methods are described that measure functional activity based on changes in: cerebral blood volume (VASO) [16,17], cell swelling (diffusion fMRI) [18,19] or glutamate neurotransmitter levels (fMRS) [20,21]. These techniques are promising, but overall they face the same challenges as BOLD fMRI of balancing temporal and spatial resolution.
A more rigorous approach is to increase the strength of the main magnetic field ($B_0$ field) of MRI scanners even further. When going to higher $B_0$ field strengths the SNR increases. In addition, for fMRI applications, the BOLD contrast increases with the $B_0$ field as well [22]. A small number of groups took this approach and constructed whole body human MRI scanners with field strengths up to 10.5T, whereas two 11.7T scanners (whole body and head-only) are currently being installed [23]. This technology is predicted to enable quantification of biochemical components of the functioning brain not detectable heretofore. Despite the clear advantages of going to a higher field strength, there are also a lot of practical challenges with this approach. These include the construction, costs, heating due to shorter RF wavelengths, increased field inhomogeneities, and the necessity of tailored MR sequences.
A project that approaches the issue from a metabolic point of view is the realization of a so called META scanner [24]. In this project fundamental knowledge is expected to be gained, by exploring metabolic pathways. A 7T scanner will be constructed to perform not just proton imaging, in addition the system will be equipped with dedicated hardware to measure several other resonances as well (including fluorine, phosphor, sodium and carbon). This could open several new windows in the MRI field.
A multimodal approach, using multiple MRI sequences with different contrast in combination with other measurement modalities, such as PET and optical microscopy, will have a great chance of unraveling some of the complex mechanisms of the brain. In the field of preclinical

animal research for example, it is possible to scan at even higher field strengths and combine these MRI measurements with invasive optical or electrophysiological recordings. Previous research showed it was possible to relate BOLD responses with intracellular neuronal calcium signals [25,26].

## Conclusion

In this work different approaches were investigated to maximize the SNR, temporal and spatial resolution of BOLD fMRI and MRS techniques to be able to gain further insight into the hemodynamics and metabolism of the human brain.

It was shown that the adaptations in acquisition and reconstruction techniques (**Chapter 2**) and receive coil configuration (**Chapter 3**) can significantly improve BOLD fMRI measurements in terms of acceleration performance for high resolution EPI scans in the human brain cortex. Novel ideas were described to be able to overcome traditional gradient limits and push acceleration even further in the future by the use of ultrasonic switching gradients (**Chapter 4**). Alternative approaches to capture neuronal activity via the brain metabolism were further optimized in terms of their acquisition setup, resulting in improved MRS measurements of the main inhibitory neurotransmitter GABA (**Chapter 5**) and inorganic phosphate (**Chapter 6**).

This work laid down strong technical fundaments, upon which both engineering, neuroscience and clinical studies can further build. With these results the ability to follow human brain processes in-vivo with biologically sufficient high spatial and temporal resolution comes a step closer. However in the big perspective, it is a small initial step in the rapidly developing field of MRI, where staggering new techniques and discoveries lie ahead.

## References


1. Dumoulin SO, Fracasso A, van der Zwaag W, Siero JCW, Petridou N. Ultra-high field MRI: Advancing systems neuroscience towards mesoscopic human brain function. Neuroimage 2018;168:345-357.
2. Yu X, Qian C, Chen DY, Dodd SJ, Koretsky AP. Deciphering laminar-specific neural inputs with line-scanning fMRI. Nat Methods 2014;11(1):55-58.
3. Petridou N, Siero JCW. Laminar fMRI: What can the time domain tell us? Neuroimage 2017.
4. Siero JC, Petridou N, Hoogduin H, Luijten PR, Ramsey NF. Cortical depth-dependent temporal dynamics of the BOLD response in the human brain. J Cereb Blood Flow Metab 2011;31(10):1999-2008.
5. Hamilton NB, Attwell D, Hall CN. Pericyte-mediated regulation of capillary diameter: a component of neurovascular coupling in health and disease. Front Neuroenergetics 2010;2.
6. Longden TA, Dabertrand F, Koide M, Gonzales AL, Tykocki NR, Brayden JE, Hill-Eubanks D, Nelson MT. Capillary K(+)-sensing initiates retrograde hyperpolarization to increase local cerebral blood flow. Nat Neurosci 2017;20(5):717-726.
7. Wang Z, Roe AW. Columnar specificity of microvascular oxygenation and blood flow response in primary visual cortex: evaluation by local field potential and spiking activity. J Cereb Blood Flow Metab 2012;32(1):6-16.
8. Polimeni JR. High Resolution Applications: Cortical Layers. Proceedings of the 26th Annual Meeting of the ISMRM, Paris, France; 2018. p E2786.
9. Polimeni JR, Wald LL. Magnetic Resonance Imaging technology-bridging the gap between noninvasive human imaging and optical microscopy. Curr Opin Neurobiol 2018;50:250-260.
10. Hillman EM. Coupling mechanism and significance of the BOLD signal: a status report. Annu Rev Neurosci 2014;37:161-181.
11. Cosottini M, Donatelli G, Costagli M, Caldarazzo Ienco E, Frosini D, Pesaresi I, Biagi L, Siciliano G, Tosetti M. High-Resolution 7T MR Imaging of the Motor Cortex in Amyotrophic Lateral Sclerosis. AJNR Am J Neuroradiol 2016;37(3):455-461.
12. Donatelli G, Ceravolo R, Frosini D, Tosetti M, Bonuccelli U, Cosottini M. Present and Future of Ultra-High Field MRI in Neurodegenerative Disorders. Curr Neurol Neurosci Rep 2018;18(6):31.
13. Zwanenburg JJ, Versluis MJ, Luijten PR, Petridou N. Fast high resolution whole brain T2* weighted imaging using echo planar imaging at 7T. Neuroimage 2011;56(4):1902-1907.
14. Feinberg DA, Vu AT, Beckett A. Pushing the limits of ultra-high resolution human brain imaging with SMS-EPI demonstrated for columnar level fMRI. Neuroimage 2018;164:155-163.
15. Feinberg DA. MRI Corticography: Developing Next Generation Microscale Human Cortex MRI Scanner; University of California, Berkeley. Grant of: National Institute of Biomedical Imaging and Bioengineering, Bethesda, USA; 2017. NIH grant number: 1U01EB025162-01.
16. Huber L, Handwerker DA, Jangraw DC, Chen G, Hall A, Stuber C, Gonzalez-Castillo J, Ivanov D, Marrett S, Guidi M, Goense J, Poser BA, Bandettini PA. High-Resolution CBV-fMRI Allows Mapping of Laminar Activity and Connectivity of Cortical Input and Output in Human M1. Neuron 2017;96(6):1253-1263 e1257.
17. Lu H, Golay X, Pekar JJ, Van Zijl PC. Functional magnetic resonance imaging based on changes in vascular space occupancy. Magn Reson Med 2003;50(2):263-274.
18. Le Bihan D, Urayama S, Aso T, Hanakawa T, Fukuyama H. Direct and fast detection of neuronal activation in the human brain with diffusion MRI. Proc Natl Acad Sci U S A 2006;103(21):8263-8268.
19. Tsurugizawa T, Ciobanu L, Le Bihan D. Water diffusion in brain cortex closely tracks underlying neuronal activity. Proc Natl Acad Sci U S A 2013;110(28):11636-11641.
20. Cleve M, Gussew A, Reichenbach JR. In vivo detection of acute pain-induced changes of GABA+ and Glx in the human brain by using functional 1H MEGA-PRESS MR spectroscopy. Neuroimage 2015;105:67-75.
21. Mullins PG, Rowland LM, Jung RE, Sibbitt WL, Jr. A novel technique to study the brain's response to pain: proton magnetic resonance spectroscopy. Neuroimage 2005;26(2):642-646.

22. Pohmann R, Speck O, Scheffler K. Signal-to-noise ratio and MR tissue parameters in human brain imaging at 3, 7, and 9.4 tesla using current receive coil arrays. Magn Reson Med 2016;75(2):801-809.
23. Budinger TF, Bird MD. MRI and MRS of the human brain at magnetic fields of 14T to 20T: Technical feasibility, safety, and neuroscience horizons. Neuroimage 2018;168:509-531.
24. Klomp DW. META-scan: A non-invasive metabolic imaging tool to study treatment response; University Medical Center Utrecht. Grant of: Netherlands Organisation for Scientific Research (NWO); 2016. NWO grant number: 175.010.2015.006.
25. He Y, Wang M, Chen X, Pohmann R, Polimeni JR, Scheffler K, Rosen BR, Kleinfeld D, Yu X. Ultra-Slow Single-Vessel BOLD and CBV-Based fMRI Spatiotemporal Dynamics and Their Correlation with Neuronal Intracellular Calcium Signals. Neuron 2018;97(4):925-939 e925.
26. Schulz K, Sydekum E, Krueppel R, Engelbrecht CJ, Schlegel F, Schroter A, Rudin M, Helmchen F. Simultaneous BOLD fMRI and fiber-optic calcium recording in rat neocortex. Nat Methods 2012;9(6):597-602.

# Appendix

## Dankwoord

Dit proefschrift is mede tot stand gekomen dankzij de inzet, energie en ondersteuning van verschillende mensen. Velen hebben bijgedragen, zowel aan het onderzoek als aan de goede sfeer binnen en buiten het UMC. Het was teamwork en ik wil jullie hier allemaal voor bedanken! Het is niet mogelijk om iedereen bij naam te noemen, maar je weet dat ik jou bedoel, dus bij deze: BEDANKT! Hieronder doe ik, tegen beter weten in, toch een poging om de meeste namen even te noemen.

Mijn promotieteam, Peter, Natalia en Dennis. Peter, volgens mij ben ik de laatste PhD student die nog lang bij jou op de Q2-gang gezeten heeft. Als professor 7T Strategic Impulse, geef jij nu inmiddels leiding aan de hele divisie Beeld van het UMC (en meer!), geweldig. Ondanks dat alles, ben je gelukkig nog altijd te porren voor een praatje over gitaren, muziek en effectpedalen. In de latere jaren heb ik het zeer gewaardeerd dat je nog steeds de moeite nam om aanwezig te zijn bij mijn evaluatiegesprekken en daarin een belangrijke motiverende bijdrage hebt geleverd.
Natalia, we did not know each other before I started this PhD project, but I am very grateful you were my co-promotor. Your work and expertise in the fMRI field has made a big impression on me. During my PhD project, you opened closed-doors, improved the quality of my work, and allowed me to explore the research field around the globe. Thank you!
Dennis, jouw enthousiasme en energie heeft mij altijd erg geïnspireerd. Dit is één van de redenen waarom ik, na mijn master project, ook aan een PhD traject ben begonnen. Je hebt me gestimuleerd om het maximum uit mezelf te halen. Denk o.a. aan: de scansessies in de avonduren (daar gaat het privéleven?), de Out-of-the-Box Challenge, en een exotische management cursus. Je bent een voorbeeld voor mij hoe je 10 ballen tegelijk in de lucht kan houden en toch zoveel voor elkaar weet te boksen. Ik heb veel van je geleerd, dank je wel!

Geachte leden van de beoordelingscommissie, prof.dr. J. Hendrikse, prof.dr.ir. J.J.W. Lagendijk, dr.ir. J.P. Wijnen, prof.dr. S. Dumoulin, prof.dr. D.G. Norris, dank voor jullie bereidheid mijn proefschrift kritisch te beoordelen en deel te nemen aan de promotieplechtigheid.

Federico, I still do not know how it happed that our paths crossed. But I am very happy it did. Your help with the Philips Recon 2.0 code was essential. We were able to push the CAIPI project to the next level, because you decided to join the late night MRI sessions (argh! not Friday evening ☺). I am glad we managed to find a way to keep you at the UMC a little longer.

Co-authors, Catalina, Alessio, Mark, Wybe, Tim, Liesbeth, Tijl, Jeroen S. en Debra. Jullie namen staan natuurlijk al gedrukt op de publicaties en hoofdstukken van dit proefschrift. Toch wil ik jullie bedanken voor jullie hulp bij verschillende projecten. Jullie hebben bijgedragen aan dit onderzoek, ook voordat er sprake was van een goed resultaat of een publicatie.

Jannie, Anna G., Wouter S., Pim, Sjoerd, Bjorn, Rob, Anna A., Anouk S., Martijn, Hans, Fredy, Alessandro en Dimitri. Op verschillende momenten tijdens mijn PhD hebben jullie mij stappen vooruit geholpen, via brainstorms, GABA metingen, g-factormaps, CAIPI reconstructies, MRI coils of via suggesties in meetings (spectromeeting, trackingmeeting, groupmeeting). Bedankt hiervoor! Master studenten, Nawied, Carel en Luisa. Naast dat ik jullie afstudeerstages heb mogen begeleiden, hebben jullie tijdens verschillende perioden een belangrijke bijdrage geleverd aan dit proefschrift. Het was een mooie samenwerking!

De guys van kamer Q.02.4.312, Janot, Tim, Oscar en Frank. Wat een bende maken jullie er toch van. Heerlijk! Meerdere buitenstaanders hebben aangegeven dat het te gezellig is op onze kamer. Onzin! Er wordt keihard gewerkt, ons kantoor is het best bezette kantoor van de gang inclusief avonduren en vakantietijden. De critici komen gewoon altijd op het verkeerde moment binnen ☺.
Oscar, jij weet altijd de rust te bewaren en zit vol met goeie verhalen en advies in verband met de nieuwste ontwikkelingen binnen de cryptocurrency. Frank, jouw deskundigheid en onderwijs op het gebied van gif's, internet memes en kantoorhumor zullen mij nog lang bijblijven. Tim, jij hebt mij op meerdere vlakken tijdens mijn PhD geholpen, zowel met inhoudelijke brainstroms over bijvoorbeeld de MRI acquisitie code, als met politiek ten opzichte van bedrijven, supervisors en promotiereglementen. Daarnaast zijn de tafelvoetbal en boardgame activiteiten altijd zeer geslaagd! Janot, al vanaf de vierde verdieping (Q4) zitten wij bij elkaar op kantoor. Dit is per toeval gestart, maar als ik het voor het uitkiezen zou hebben, zou dat weer zo gaan. Ik kan mij geen chillere kamergenoot voorstellen. We hebben samen een hoop beleefd tijdens de afgelopen vier jaar: borrels, hardloop estafettes, stapavonden, PhD stress, UMC feesten, congressen, tennis, festivals, (tafel)voetbal events, brainstorms en natuurlijk kantoorpraat. Jij was erbij! Ik voel mij vereerd dat je als paranimf aan mijn zijde wilt staan tijdens mijn defence.

Het feest-, tafelvoetbal-, bbq¬, stap- en koffieteam. Erwin, Cyril, Alex, Lisa, Arjen, Sander, Niek, Bart, Quincy, Anneloes, Carlo, Matteo, Tijl, en de partysquad: Suzanne, Deji en Isabel. Jullie weten wat echt belangrijk is: gezelligheid. Door jullie zijn de afgelopen vier jaar stukken leuker geworden. Erwin, al vanaf de flexplekken zijn wij als master studenten aan dit ongelofelijke UMC traject begonnen. Wat een achtbaanrit is het geweest. Ik ben blij dat jij er nu ook bij bent om het af te sluiten. Een saluut aan de oude garde: Ronald, Wouter K., Lennart, Anita, Alexandra, Mariska L., Mariska D., Nikki, Hanke, Joep, Irene, Anja, Jolanda, Wieke, Matthew, Vitaly, Stefano, Jill en Vincent. Ik wens jullie het beste. We komen elkaar vast nog tegen!

Een woord van dank aan de vele UMC-gangers. Jullie maken het UMC een leuke werkplek. Edwin, Jacob-Jan, Peter S., Flavio, Tine, Anna K, Sylvia, Marja, Mike, Katharina, Bart F., Carrie, Alberto, Beatrice, Lieke, Bastiaan, Ria, Cezar, Alexander, Jeanine, Jaco, Nico, Rik, Aidin, Ingmar, Erik, Luca, Lisa O., Michel, Bart-Jan, Salam, Tuan, Sophie, Ellis, Soraya, Robin, Anna D. en Tom.

Jeugdvrienden, "U-towners," Thijs, Merel, Eline, Koos, Frederick en Sara. Ik ben er de afgelopen tijd een paar keer niet bij geweest, maar daar gaat na mijn defence gelukkig weer verandering in komen. Op de vele drankjes die we samen nog gaan drinken. Huisgenootjes "Graaf A.," bedankt voor de leuke huisuitjes. Studiegenoten, "Eindhovense gekken," specifiek: Niels, Ashley, Jonas en Annette. Op de vele borrels, stapavonden en Science & Technology Quiz Nights die we gehad hebben en nog gaan meemaken (of winnen). My internationals, mainly met in Zürich, Maaike, Nicole, Jaap, Mara J., Camilla, Sabine, and Jeroen. During my PhD, our trips and reunions gave me so much joy! I am looking forward to all the countries, weekends and crazy adventures that lie ahead of us!

Last but definitely not least, mijn familie. Broer en zus, Sander en Mariska. Bedankt voor jullie steun, hulp en afleiding. Jullie betekenen veel voor mij. Als drie musketiers veroveren wij samen de wereld! Sander zei net, dat hij niet begreep dat ik dit boek verder wilde schrijven, in plaats van mee te gaan tennissen. Daar heeft hij eigenlijk wel een goed punt. Dus ik ga afsluiten, maar niet zonder mijn ouders te bedanken. Ik zou het niet ver geschopt hebben, zonder jullie grenzeloze support en geloof in mijn kunnen, niet alleen als het goed gaat, maar ook als het even tegen zit. Zonder jullie zou dit proefschrift er niet zijn geweest. Bedankt dat ik mijn MRI verhalen bij jullie kan vertellen of gewoon even kan bijkomen. Op de mooie verhalen en avonturen die we samen nog gaan beleven!

# Publication list

## Scientific publication

**A.D. Hendriks**, P.R. Luijten, D.W.J. Klomp, N. Petridou. Potential acceleration performance of a 256-channel whole-brain receive array at 7 T. Magnetic Resonance in Medicine 2018 https://doi.org/10.1002/mrm.27519. *Epub ahead of print*

**A.D. Hendriks**, A. Fracasso, C.S. Arteaga de Castro, M.W.J.M. Gosselink, P.R. Luijten, N. Petridou, D.W.J. Klomp. Maximizing sensitivity for fast GABA edited spectroscopy in the visual cortex at 7 T. NMR in Biomedicine. 2018;31:e3890. https://doi.org/10.1002/nbm.3890

**A.D. Hendriks**, F. D'Agata, T. Schakel, L. Geerts, P.R. Luijten, D.W.J. Klomp, N. Petridou. High density receive arrays in combination with shot selective 2D CAIPIRINHA for 3D EPI scans: accelerated sub-millimeter functional and anatomical MRI at 7T. *Submitted for publication*

**A.D. Hendriks**, W.J.M. van der Kemp, P.R. Luijten, N. Petridou, D.W.J. Klomp. SNR optimized $^{31}$P functional MRS to detect mitochondrial and extracellular pH change during visual stimulation. *Submitted for publication*

B.J. van Nierop, B.F. Coolen, W.J.R. Dijk, **A.D. Hendriks**., L. de Graaf, K. Nicolay, G.J. Strijkers, Quantitative first-pass perfusion MRI of the mouse myocardium. Magnetic Resonance in Medicine. 2013;69: 1735–1744. https://doi.org/10.1002/mrm.24424

## Patent

D.S. Rivera, **A.D. Hendriks**, T.A. van der Velden, J.C. Siero, D.W.J. Klomp. Method and apparatus for ultrasonic gradients in magnetic resonance imaging. European Patent Office. Application No./Patent No.: 17020058.8 – 1568. Date of filing: 17-02-2017. *Patent application*

## Conference proceedings (selection)

**A.D. Hendriks**, W.J.M. van der Kemp, N. Petridou, D.W.J. Klomp. SNR optimized $^{31}$P fMRS to measure energy metabolism in the visual cortex. Proceedings of the Joint Annual Meeting of the ISMRM-ESMRMB 2018, Paris, France. Program number: 3997

**A.D. Hendriks**, F. D'Agata, T. Schakel, L. Geerts, D.W.J. Klomp, N. Petridou. Shot selective 2D CAIPIRINHA for 3D EPI scans: combination with high density receive arrays and application to sub-millimeter functional and structural MRI at 7T. ISMRM Benelux Chapter 10$^{th}$ Annual Meeting 2018, Antwerpen, Belgium. Abstract and presentation number: Oral-22.

N.D. Sijtsema, **A.D. Hendriks**, P.R. Luijten, D.W.J. Klomp, P.J.W. Pouwels, C.S. Arteaga de Castro. 4-Dimensional spin echo for prostate $^{1}$H MRSI at 7T using a multi-transmit system. Proceedings of the 25th Annual Meeting of the ISMRM 2017, Honolulu, Hawaii. Program number: 3020

B. Gruber, **A.D. Hendriks**, C.B.S. Alborahal, B. Brussen, T. Leiner, G.J. Strijkers, D.W.J. Klomp, M. Froeling. The potential of a 256-Channel receive-only array for accelerated Cardiac Imaging

at 3T. Proceedings of the 25th Annual Meeting of the ISMRM 2017, Honolulu, Hawaii. Program number: 4319

**A.D. Hendriks**, C.B.S. Alborahal, M.G.M. Italiaander, D.W.J. Klomp, N.Petridou. The potential of 256 channel high density receive arrays in combination with 2DCAIPIRINHA at 7T. Proceedings of the 24th Annual Meeting of the ISMRM 2016, Singapore. Program number: 3235

**A.D. Hendriks**, N. Petridou, C.S. Arteaga de Castro, M.W.J.M. Gosselink, A. Fracasso D.W.J. Klomp. Pushing the limits of speed and accuracy for 7T GABA MR spectroscopy to reveal GABA level fluctuations in resting brain. Proceedings of the 24th Annual Meeting of the ISMRM 2016, Singapore. Program number: 3340

**A.D. Hendriks**, M.G.M. Italiaander, N. Petridou, D.W.J. Klomp. Potential gain of a 256 channel head coil at 7T: combined measurements and g-factor calculations. Proceedings of the 23th Annual Meeting of the ISMRM 2015, Toronto, Canada. Program number: 3166

**A.D. Hendriks**, C.S. Arteaga de Castro, V.O. Boer, D.W.J. Klomp, N. Petridou. Wide screen visual stimulation: fMRI combined with fast GABA detection. Proceedings of the 23th Annual Meeting of the ISMRM 2015, Toronto, Canada. Program number: 3200

R. Krijthe, V.O. Boer, **A.D. Hendriks**, D.W.J Klomp. Parallel Imaging of the Prostate at 7T Using a B0 Crusher Coil to Suppress Aliasing Artifacts. Proceedings of the 23th Annual Meeting of the ISMRM 2015, Toronto, Canada. Program number: 3162

**A.D. Hendriks**, T.A. van der Velden, M.P. Luttje, V.O. Boer, P.R. Luijten, D.W.J. Klomp. 3D EPSI - Exploring the potential of 3D spectroscopic imaging of the prostate at 7 tesla. Proceedings of the Joint Annual Meeting of the ISMRM-ESMRMB 2014, Milan, Italy. Program number: 1435

## Invited talks and awards

**ISMRM Benelux Chapter Meeting, Out-of-the-box Challenge 2018**
Research proposal selected as top 3 and invited to pitch at the ISMRM Benelux Chapter Meeting.

**Erwin L. Hahn Spectroscopy Workshop 2014, 8th of October.**
Invited research presentation titled: High speed 3D prostate MRSI at 7T: selective RF excitation pulses, EPSI readout and external body coils.

**Eindhoven-Utrecht Science and Technology student award 2013**
Best master thesis proposal of the alliance between Eindhoven University of Technology, Utrecht University and University Medical Center Utrecht.

# Summary and CV

## Summary

Our brain plays an important role in our everyday life. Nearly all of our common activities require our brain. Especially the brain cortex is essential for our thoughts, decisions, personality and imagination. Even though brain research has advanced tremendously over the recent years, there are open questions and mysteries about the brain that remain unsolved to this day. These are both fundamental questions about our consciousness and how our brain works, as well as clinical questions in case of neurological diseases like Alzheimer's and Parkinson's disease.

Magnetic resonance imaging (MRI) has proven itself to be a valuable instrument to study the human brain, allowing structures and anatomy to be visualized in-vivo at high detail. However, in order to gain more knowledge about the mechanics of the brain, static imaging of anatomy is not enough. To take the next step, it is essential to study dynamic in-vivo brain functions, including (neuronally triggered) hemodynamics and metabolism.

This thesis focuses on two MR techniques that measure brain activity via changes in hemodynamics and metabolism, specifically blood-oxygen-level dependent functional MRI (BOLD fMRI) and magnetic resonance spectroscopy (MRS). In general, MRI measurements are a tradeoff between the signal-to-noise ratio (SNR), resolution, (dynamic) scan time and imaging volume. With MRI it is therefore possible to acquire high resolution images, but at the cost of a long acquisition time. This is not desirable when aiming to monitor fast and detailed physiological processes. For example for BOLD fMRI, the combination of both a high temporal resolution (< 1 sec) and a high spatial resolution (< 1 mm) is rarely seen. For edited MRS, the commonly reported (dynamic) scan times to measure the main inhibitory neurotransmitter γ-aminobutyric acid (GABA), range between 6 – 30 minutes. This is long when looking at the time scale of brain functions. Therefore, in this thesis it is intended to lift some of the technical barriers for different MR techniques to get closer to measurements at the speed of physiological brain processes. The aim of this thesis is to maximize the SNR, temporal resolution and spatial resolution of BOLD fMRI and MRS techniques to be able to gain further insight into the hemodynamics and metabolism of the human brain.

To achieve this aim five approaches (**Chapters 2-6**) are pursued to make BOLD fMRI and MRS techniques more suitable for fast and high resolution in-vivo measurements of physiological processes in the human brain. First, the dynamic scan time of BOLD fMRI scans was reduced (**Chapter 2**) by a combination of high density receive arrays, and an advanced under sampling strategy for 3D fMRI scans (2D CAIPIRINHA for 3D EPI scans). Second, simulations were performed (**Chapter 3**) showing the potential of a 256 channel receive array for whole brain imaging to reduce dynamic scan time of fMRI scans by an order of magnitude further. Third, the idea of ultrasonic switching gradients was presented (**Chapter 4**), which might hold even

higher accelerations for the future, as described in a patent. Fourth, the neurotransmitter GABA could be measured dynamically with GABA edited MRS techniques that have a reduced scan time of only 1:23 min (**Chapter 5**) by using a specially built half volume coil setup. Fifth, $^{31}$P MRS was found as potential new technique to explore brain function further (**Chapter 6**).

This work brings the ability to follow human brain processes in-vivo with high spatial and temporal resolution a step closer. Fundaments upon which both engineering, neuroscience and clinical studies can further build. In the big perspective, I hope it will contribute to the rapidly developing field of MRI, where staggering new techniques and discoveries lie ahead.

## Samenvatting

Ons brein bepaalt voor een groot deel wie wij zijn. Het herbergt onze gedachten, keuzes, herinneringen, dromen en persoonlijkheid. Vooral de cortex van het brein speelt een essentiële rol bij deze processen. Ondanks dat er al veel kennis over het brein bestaat en wetenschappelijk onderzoek in de laatste jaren met grote sprongen vooruit is gegaan, zijn er nog een hoop onbeantwoorde vragen. Dit zijn zowel fundamentele vragen die over ons bewustzijn gaan of over hoe ons brein precies werkt, als klinische vragen in verband met ingrijpende hersenziektes zoals Alzheimer of Parkinson.

*Magnetic resonance imaging*, beter bekend als MRI, heeft zich gemanifesteerd als een waardevol instrument om het menselijk brein te bestuderen. MRI maakt het mogelijk om structuren en anatomie van het brein met hoog detail te visualiseren. Echter, om meer te weten te komen over de werking van het brein, zijn statische beelden van brein anatomie niet toereikend. Het is essentieel om te kijken naar het levende dynamische brein in functie, waaronder (neuronaal getriggerde) processen op het gebied van hemodynamica en metabolisme.

In deze thesis ligt de focus op twee MR technieken die brein activiteit meten via veranderingen in hemodynamica en metabolisme, namelijk *blood-oxygen-level dependent functional MRI* (BOLD fMRI) en *magnetic resonance spectroscopy* (MRS). Over het algemeen zijn MRI metingen een compromis tussen de signaal-ruisverhouding (SNR), resolutie, scan tijd per beeld en het scan gebied. Het is daardoor mogelijk om beelden van het brein te maken met een hoge resolutie, maar wel ten koste van een langere scan tijd. Dit is ongewenst, zeker wanneer het de bedoeling is meerdere beelden snel achter elkaar te maken, om snelle en gedetailleerde fysiologische processen te volgen. Voor BOLD fMRI bijvoorbeeld, komt de combinatie van een korte scan tijd (< 1 sec) en een hoge resolutie (< 1 mm) nog nauwelijks voor. Voor MRS, is de gebruikelijk scan tijd om de voornaamste inhiberende neurotransmitter γ-aminoboterzuur (GABA) te meten met GABA edited MRS scans tussen de 6 tot 30 minuten. Dit is lang in vergelijking tot de tijdsduur van verschillende hersenfuncties. Deze thesis is daarom gericht op het doorbreken van de technische barrières van verschillende MR technieken, om metingen te kunnen verrichten die de werkelijke snelheid van fysiologische processen in het brein beter benaderen. Het overkoepelende doel van deze thesis is de SNR, temporele resolutie en ruimtelijke resolutie van BOLD fMRI en MRS technieken te maximaliseren, om beter in staat te zijn kennis van het menselijk brein te vergaren op het gebied van hemodynamica en metabolisme.

Om dit doel te bereiken zijn 5 strategieën (**Hoofdstuk 2-6**) nagestreefd om BOLD fMRI en MRS technieken geschikter te maken om fysiologische processen in het brein te volgen met een hoge resolutie en snelheid. Ten eerste, voor BOLD fMRI scans is de benodigde tijd per beeld verkort (**Hoofdstuk 2**), door een combinatie toe the passen van meerdere kleine dicht

op elkaar geplaatste ontvangst spoelen, en een geavanceerde undersamplingsmethode voor 3D fMRI scans (2D CAIPIRINHA voor 3D EPI scans). Ten tweede, zijn er simulaties uitgevoerd (**Hoofdstuk 3**), die laten zien dat met een 256 kanaals ontvangstsysteem voor het hele brein, de scan tijd van fMRI scans met een orde van grootte verkort kan worden. Ten derde, het idee van ultrasonisch schakelende gradiënten is geïntroduceerd (**Hoofdstuk 4**), dit kan in de toekomst mogelijk voor nog snellere scans zorgen, zoals beschreven in een patent. Ten vierde, veranderingen in de concentratie van de neurotransmitter GABA kunnen sneller over de tijd gemeten worden met GABA edited MRS technieken en een korte scan tijd van 1:23 min, door het gebruik van een speciaal ontwikkelde half volume setup (**Hoofdstuk 5**). Ten vijfde, $^{31}$P MRS is ingezet als potentiele nieuwe techniek om brein functies verder te ontrafelen (**Hoofdstuk 6**).

Dit werk vergroot de mogelijkheden om de processen van het levend menselijk brein met hoge temporele en ruimtelijke resolutie te volgen. Hiermee wordt een fundament gelegd, waar zowel technische studies, neurowetenschappelijke studies als klinische studies verder op kunnen bouwen. In het grotere perspectief, hoop ik dat dit werk zal bijdragen aan het snel groeiende MRI veld, waar de toekomst nieuwe technieken en sensationele ontdekkingen met zich mee zal brengen.

## Curriculum vitae

Arjan Hendriks was born in Utrecht on 6 August 1990. His interest in MRI grew during his study Biomedical Engineering at the Eindhoven University of Technology (TU/e). He followed initial courses on MRI during his Bachelor, and did his final Bachelor project on cardiovascular perfusion MRI. For his Masters, he joined the Biomedical NMR group of Klaas Nicolay at the High Tech Campus in Eindhoven. In extension to the program, he did an internship at the ETH in Zürich, Switzerland in the Cardiovascular Magnetic Resonance Group of Sebastian Kozerke. His master Medical Engineering focused on the translation of engineering principles to the clinical setting, so he combined the work in Eindhoven with several courses and projects at the Maastricht University Medical Center (MUMC). For his final Master thesis he linked up with the University Medical Center in Utrecht (UMC Utrecht), where his Master thesis proposal was awarded as the best of the Utrecht-Eindhoven Strategic Alliance 2013. His master thesis was performed predominantly in the High field group of the UMC Utrecht under supervision of Dennis Klomp. Here, he worked on non-invasive determination of prostate cancer aggressiveness using MR spectroscopy. After finalizing his Masters at the TU/e, he was invited to come back to the UMC Utrecht to start a PhD trajectory on brain MRI in a joined project of Natalia Petridou and Dennis Klomp. The research of this four year PhD project has resulted in this thesis.